OPTIMIZATION OF LASER CLADDED IN625/SS316L FUNCTIONALLY GRADED MATERIAL FOR HEAT EXCHANGER APPLICATIONS

JOSEPH BOPHELO MORAKE

MASTER OF SCIENCE

(Mechanical Engineering)

JOMO KENYATTA UNIVERSITY

OF

AGRICULTURE AND TECHNOLOGY

2024

Optimization of Laser Cladded IN625/SS316L Functionally Graded Material for Heat Exchanger Applications

Joseph Bophelo Morake

A Thesis Submitted in Partial Fulfilment of the Requirements for the Degree of Master of Science in Mechanical Engineering of the Jomo Kenyatta University of Agriculture and Technology

2024

DECLARATION

This thesis is my original work and has not been presented for a degree in any other University

Signature…….……...Date……..

Joseph Bophelo Morake

This thesis has been submitted for examination with our approval as the University supervisors

Signature…….……...Date……..

Dr. Martin Ruthandi Maina, PhD

JKUAT, Kenya

Signature…….……...Date……..

Dr. James Mutuku Mutua, PhD

JKUAT, Kenya

Signature…….……...Date……..

Prof. Eyitayo Olatunde Olakanmi, PhD

BIUST, Botswana

DEDICATION

This thesis is dedicated to my mother Jane Morake, for her support and raising me up despite all odds and believing in me.

“In honor of the loving memory of my father, Meshack Seloko Morake”

ACKNOWLEDGEMENT

First and foremost, I want to express my gratitude to God Almighty for His pro- tection in all my endeavors, His faithfulness in my life, and the grace to complete this work. I want to sincerely thank the Education for Laser-based Manufac- turing consortium funded by the European Union for awarding me a Master's scholarship to further my studies. Additionally, I appreciate the African Laser Centre (ALC) for supporting my experimental work. At the CSIR Laser Enabled Manufacturing group, Pretoria, I want to recognize Prof. Sisa Pityana and Mr. Samuel Skhosane for providing insightful guidance during my experimental work and assisting with operating the laser cladding machine. I would like to extend my sincere gratitude to my supervisors, Dr. Martin R. Maina, Dr. James M. Mutua, and Prof. Eyitayo O. Olakanmi, for their unwavering support through- out my academic career, prompt response, fruitful discussions, encouragement, providing significant insights into my research work, mentorship, and accompa- nying me during research and site visits. May God continue to bless you for your tireless efforts. I am very grateful to the Jomo Kenyatta University of Agriculture and Technology (JKUAT) management for providing me with the opportunity and resources to study at this renowned institution. My deepest appreciation to the custodian of my research errands, Dr. Rehema Ndeda for her valuable support and coordinating my scholarship errands. I appreciate Olkaria Manage- ment, especially Eng. Moses Ikote, for their continued support and opening doors for industrial collaboration. Lastly, it would be very remiss to not mention the Morake family (Jane, Rebecca, Omogolo, Kebame, Kimberly, and Basadibothe), as well as my friends and colleagues (Ivyne C, Faith M, A. Ngenzi, C. Odhiambo, J. Adem, and D. Ngene, K. Shuvai). Their love, encouragement, patience, and support throughout my study have always been my source of strength.

TABLE OF CONTENTS

DECLARATION ..... **ii**

DEDICATION ..... **iii**

ACKNOWLEDGEMENT ..... **iv**

TABLE OF CONTENTS ..... **v**

LIST OF TABLES ..... **ix**

LIST OF FIGURES ..... **x**

LIST OF SYMBOLS ..... **xvi**

LIST OF APPENDICES ..... **xvii**

ACRONYMS AND ABBREVIATIONS ..... **xviii**

ABSTRACT ..... **xx**

CHAPTER ONE **1**

INTRODUCTION **1**

1.1 Chapter Overview 1

1.2 Background 1

1.3 Heat Exchangers at Olkaria Power Plant 7

1.4 Statement of the Problem 9

15 Objectives 10

1.5.1 Specific Objectives 11

1.6 Justification of the Study 11

17 Scope of the Study 12

1.8 Organization of the Thesis 13

CHAPTER TWO 15

LITERATURE REVIEW 15

2.1 Chapter Overview 15

2.2 Shell and Tube Heat Exchanger 15

2.2.1 Working Principle of the Shell and Tube Heat Exchanger 16

2.3 Failure Mechanisms in Shell and Tube Heat Exchangers 18

2.4 Materials for Heat Exchanger Pipes 22

2.4.1 Stainless Steel Substrates and Coatings 22

2.4.2 Copper-alloy Substrates and Coatings 25

2.4.3 Nickel-based Substrates and Coatings 28

2.5 Functionally Graded Coatings for Heat Exchanger Applications 33

2.6 Laser Cladding Functionally Graded Materials for Heat Exchanger Pipe Coatings 39

2.7 Laser Cladding Process Parameters 43

2.7.1 Laser Energy Density 45

2.7.2 Composition and Powder Flow Rate 49

2.7.3 Substrate Preheating 53

2.7.4 Shielding Gas Type and Velocity 57

2.8 Summary of Literature 58

CHAPTER THREE 61

RESEARCH METHODOLOGY 61

3.1 Chapter Overview 61

3.2 Heat Exchanger Failure Analysis Procedure 61

3.2.1 Visual Inspection of the Tube Samples 61

3.2.2 Chemical Analysis of the Water 62

3.2.3 Microstructural Investigation of the Failure Samples 63

3.2.4 Residual Stress Measurements 64

3.3 Fabrication of FGM Samples Using Laser Cladding 64

3.3.1 Materials and Methods 64

3.3.2 Laser Cladding Process 65

3.5 Sample Preparation and Characterization 67

3.6 Analysis of Data 68

CHAPTER FOUR 70

RESULTS and DISCUSSION 70

4.1 Chapter Overview 70

4.2 Failure Analysis of Shell and Tube Heat Exchanger 70

4.2.1 Visual inspection of the Tube Samples 70

4.2.2 Chemical Analysis of Water Samples and Corrosion Residue 75

4.2.3 X-Ray Fluorescence Analysis 76

4.2.4 Optical Microscopy Analysis 79

4.2.5 Scanning Electron Microscopic and EDS Analysis 80

4.2.5 X-Ray Diffraction Analysis..... 82

4.2.6 Mitigation Measures to Combat the Degradation of Heat Exchangers 83

4.3 Effects of Process Parameter on Clad Quality Characteristics 97

4.3.1 Effects of Process Parameters on Aspect Ratio..... 101

4.3.2 Effects of Process Parameter on Porosity..... 103

4.3.3 Effects of Process Parameters on Surface Roughness..... 106

4.4 Confirmation and Optimization..... 108

4.5 Chapter Summary..... 115

CHAPTER FIVE..... 116

CONCLUSIONS AND RECOMMENDATIONS..... 116

5.1 Conclusions..... 116

5.2 Recommendations..... 116

REFERENCES..... 118

APPENDICES 135

LIST OF TABLES

Table 2.1: Summary of Gaps Identified in the Literature..... 60

Table 3.1: Summary of the Sample Information and the Measuring Conditions 63

Table 3.2: Chemical Composition of the SS316L and IN625 Materials (wt-%) 64

Table 3.3: Taguchi L9 Orthogonal Array for Fabricating SS316L/IN625 FGM 67

Table 4.1: Chemical Composition of the Water Circulating in the Heat Exchanger 78

Table 4.2: Chemical Composition of the Exchanger Tubes and Corrosion Residue 82

Table 4.3: GRA Experimental Output Responses for Quality Characteristics..... 86

Table 4.4: Normalized Response Values for Output Variables..... 88

Table 4.5: Deviation Sequences of the Normalized Responses..... 91

Table 4.6: Grey Relational Coefficient, Grey Relational Graded, and their Ranking 92

Table 4.7: Architecture for Different Trials Employed in ANN Predicting 94

Table 4.8: Comparison of the GRG Values Predicted by ANN and Those Calculated by GRA 96

Table 4.9: Response for the S/N Ratios of the FGM Microhardness..... 99

Table 4.10: Response Table for the S/N Ratios of the FGM Microhardness. 102

Table 4.11: Response Table for the S/N Ratios of the FGM Porosity. 104

Table 4.12: Response Table for the S/N Ratios of the FGM Surface Roughness ... 107

Table 4.13: Comparison between Taguchi Optimum Sample and ANN Optimized Sample 110

LIST OF FIGURES

Figure 1.1: Illustration of the Laser Cladding Process in Fabricating Functionally Graded Materials..... 3

Figure 1.2: Schematic Structure and Properties of Functionally Graded Materials.... 4

Figure 1.2a: Solid Solution Strengthening Substitutional Mechanism of Solute in Lattice Structure..... 5

Figure 1.2b: Heat Exchanger Schematic Illustration of the Operating Conditions and Configuration 8

Figure 1.3: Failed Shell and Tube Heat Exchanger (a) General View of the Shell (b) Internal Stacked Copper Tubes 9

Figure 2.1: Structure of a Shell and Tube Heat Exchanger..... 17

Figure 2.2: Flow Configuration of Fluids in Heat Exchangers 18

Figure 2.3: Chlorine-Induced Tube Failure Causing (a) Tube Leakage Observed and (b) Microstructural Crack Propagation at the Interface 20

Figure 2.4: Corrosion attack on the Microstructural Grain Boundary of a Boiler Tube Operating in Hostile Temperature Conditions..... 21

Figure 2.5: Corrosion Attack of FeCrAl Coating Deposited on SA213- T11 Steel Showing the Microstructural Substrate/Coating Interface..... 24

Figure 2.6: Microstructural Refinement in Laser-Cladding Nickel Coatings on a Copper Substrate (a) Martensitic Structure, to Cystic Form- Dendrites (b) Highlighted Square Viewed At a Larger Magnification..... 27

Figure 2.7: Laser Cladding Ni60A on Copper Pipes Original Copper Pipes before Deposition..... 28

Figure 2.8: SEM Morphology of Nickel-Based Coating Showing: (a) Dendrite (b) Interdendritic Phase 31

Figure 2.9: Potential Fields of FGM Application in the Heat Exchanger Industry .. 34

Figure 2.10: Variations in Microstructure with Increasing Content (a) Inconel 718 at 100% (b) Inconel 718 at 80% and 20% Haynes 40% Inconel 718 and 40% Haynes (d) 60% and Inconel 718 80% and Inconel 718 in Haynes (e) 205 100% Haynes (e) Haynes 36

Figure 2.11: Microstructural Variation on Functionally Graded SS316L/In718 37

Figure 2.12: Microstructural Evolution of Laser Metal Deposited SS316L/IN718/Cu Functionally Graded Material (a) SS316L Columnar Dendrites (b) Good Bonding at the Interface (c) IN718 Equiaxed Structure 39

Figure 2.13: Interaction of the laser beam with FGM Powders during Laser Cladding 40

Figure 2.14: The Phenomenon of Marangoni Convection during Melting 43

Figure 2.15: The Ishikawa Fish-Bone Diagram Illustrating the Influence of Laser Cladding Process Parameters on Cladding Quality Characteristics..... 44

Figure 2.16: The Microstructure With Varying LED (a) Pore Defects at 60 J/mm2 (b) Optimum Structure without Defects (c,d) Large Pore Inclusions at 80 to 90 J/mm^2..... 47

Figure 2.17: Comparison of Microstructural Bonding at the Interface for (a, b) Non-Optimized Deposition with Lack Of Fusion (c,d) Well-Optimized Deposition 50

Figure 2.18: Increasing Microhardness Profile Concerning Composition Grading . 51

Figure 2.19: Microhardness Profile Variation with Increasing Elemental Content .. 52

Figure 2.20: Input to Output Structure of the Artificial Neural Network 53

Figure 2.21: Microstructure Characterized By (a) Cracks at the Interface (b) Secondary Phase and Inclusions 55

Figure 2.22: Crack Propagation at the Interface of Functionally Graded Material .. 56

Figure 2.23: TMicrostructure with varying LED (a) Pore Defects at 60 J/mm^2 (b) Optimum Structure without Defects (c,d) Large Pore Inclusions at 80 to 90 J/mm^2..... 58

Figure 3.1: Sample Heat Exchanger Tubes Investigated for Failure (a) Intact Tube, Sample T1 (b) Failed Tube, Sample T2..... 62

Figure 3.2: Sample Positioning for Residual Stress Measurements (a) Failed Tube and (b) Intact Tube..... 64

Figure 3.3: SEM Powder Morphology of (a) Stainless Steel 316L (b) Inconel 625. 65

Figure 3.4: Laser Cladding System (a) Kuka Robot with a 5kW IPG YLS 5000 Fiber Laser System (b) Coaxial Nozzle 66

Figure 3.5: FGM Layer Build-Up (a) As-Built SS316L/IN625 clad (b) Compositional Variation (wt.%)..... 67

Figure 3.6: SEM Powder Morphology of (a) Stainless Steel 316L (b) Inconel 625. 69

Figure 4.1: Failed Exchanger Tubes Examined (a) Intact Sample T1 (b) Fracture T2 71

Figure 4.2: Top View of the Failed Heat Exchanger Tube Bundle..... 72

Figure 4.3: Measurement of Internal Residual Stresses at Tube Surface Compared for Sample T1 and T2 (a) Stress Values (b) Distortion (c) Residual Stress Profile..... 74

Figure 4.4: Corroded Heat Exchanger Cover Showing Brownish-to- Red Corrosion Products with Black Layers 75

Figure 4.5: Elemental Distribution and Composition of Corrosion Residue 77

Figure 4.6: Schematic Illustration of the Corrosion Process of CuNi10Fe 78

Figure 4.7: Micrographs of Heat Exchanger Tubes (a) Failed Tube with Surface Defects (b) Intact Heat Exchanger Tube with Less Surface Distortion (c) Surface Cracks Pits Growing from the Inside 79

Figure 4.8: SEM Morphology of Sulphide-Induced Corrosion Crack 81

Figure 4.9: Feature of the Corrosion Residues and the Spectrum of SEM Elemental Analysis 81

Figure 4.10: SEM Micrographs Showing the Main Crack at the Surface Due to Sulfide Stress Cracking 82

Figure 4.11: XRD Pattern of Corrosion Residues from CuNi10Fe Failed Tube 83

Figure 4.12: Illustration of SS316L/IN625 Functionally Graded Coating on CuNi Tube 85

Figure 4.13: Surface Plot Interaction of Process Parameters on GRG Output for (a) Scanning speed, Laser Power (b) Powder Flow Rate, Laser Power (c) Powder Flow Rate, Scanning Speed 93

Figure 4.14: Topology of the Developed ANN Model 95

Figure 4.15: Regression Plot of the Developed Model 97

Figure 4.16: Comparative Analysis of ANN Simulated GRG with the Experimental GRG 98

Figure 4.17: Main Effect Plot for S/N Ratios of the FGM Microhardness 99

Figure 4.18: SEM Micrographs of FGM Samples with (a) Lowest Microhardness for Sample 7 (b) Highest Microhardness for Sample 6 100

Figure 4.19: Contour Plots of the Microhardness Interaction Effects of (a) Laser Power and Scanning Speed (b) Powder Flow Rate and Scanning Speed (c) Laser Power and Powder Flow Rate..... 101

Figure 4.20: Main Effect Plot for S/N Ratios of the FGM Aspect Ratio..... 102

Figure 4.21: Contour Plots of the Aspect Ratio Interaction Effects of (a) Scanning Speed and Laser Power (b) Powder Flow Rate and Scanning Speed (c) Powder Flow Rate and Laser Power..... 103

Figure 4.22: Main Effect Plot for S/N Ratios of the FGM Porosity Level..... 104

Figure 4.23: Porosity Analysis of FGM Samples As A Function Of Laser Power; (a) 700 W (e) 850 W (i) 1000 W; Scanning Speed (c) 400 mm/min (d) 500 mm/min (h) 600 mm/min, and Powder Flow Rate; (f) 2 g/min (b) 4 g/min (g) 6 g/min..... 105

Figure 4.24: Contour Plots for the Porosity Interaction Effects of (a) Powder Flow Rate and Laser Power (b) Powder Flow Rate and Scanning Speed (c) Scanning Speed and Laser Power..... 106

Figure 4.25: Main Effect Plot for S/N Ratios of the FGM Surface Roughness 107

Figure 4.26: Contour Plots for the Surface Roughness Interaction Effects of (a) Scanning Speed and Laser Power (b) Powder Flow Rate and Scanning Speed (c) Powder Flow Rate and Laser Power..... 108

Figure 4.27: (a) Performance Improvement of GRG Values by Varying (a) Laser Power (b) Scanning Speed (c) Powder Flow Rate..... 110

Figure 4.28: Optical Micrographs Showing Microstructural Transformation of ss316l/in625 fgm Clad (a) Microstructure of the Clad Geometry (b) Copper Substrate/100%SS316L Interface (c) Layer 1 and 2 Interfaces (d) layer 2 and 3 Interfaces (e) layer 3 and 4 Interfaces (f) Layer 4 and 5 Interface 111

Figure 4.29: Vickers Microhardness Profile of Cu Substrate and SS316L/ IN625 FGM along the Clad Build Direction 112

Figure 4.30: SEM Micrograph of the FGM Microstructure at 50-50 wt% of SS316L/IN625 113

Figure 4.31: The SEM-EDS Mapping of the Cu-SS316L Dilution Zone (a) Substrate/Coating Interface, and Diffusion of (b) Cr (c) Fe Si (e) S (f) Ni 113

Figure 4.32: Residual Stress Measurements of SS316L/IN625 FGM (a) Pure Copper Substrate (b) As-Built SS316L/IN625 FGM and (c) Heat- Treated Cladding..... 115

LIST OF SYMBOLS

Σ	Stress [MPa]
ξ	Distinguishing Coefficient
D	Dilution
Ω	Powder Flow Rate [g/min]
G	Grey Relational Grade
GCij	Grey Relational Coefficient
H	Height of Deposit [mm]
P	Power [kW]
Ra	Surface Roughness (μm)
T	Scanning Speed [mm/min]
W	Watts
$\mathbf{W_d}$	Width of Deposit [mm]
$\mathbf{X_{ij}}$	Normalized Value
$\mathbf{Y_{ij}}$	Response Value

LIST OF APPENDICES

Appendix I: ANN Program/Code 135

ACRONYMS AND ABBREVIATIONS

AM	Additive Manufacturing
AR	Aspect Ratio
ANN	Artificial Neural Network
BPNN	Back Propagation Neural Network
D	Depth of Deposit
DoE	Design of Experiments
GRA	Grey Relational Analysis
FGM	Functionally Graded Material
HAZ	Heat Affected Zone
GRG	Grey Relational Grade
HX	Heat Exchanger
IN625	Inconel 625
LC	Laser Cladding
LED	Laser Energy Density
LP	Laser Power
H	Microhardness
P	Porosity
SEM	Scanning Electron Microscope

SR	Surface Roughness
S/N	Signal-to-Noise Ratio
SS316L	Stainless Steel 316L
S/N	Signal-to-Noise Ratio

ABSTRACT

Engineering components operating in severe working environments require resilient materials that can withstand degradation caused by corrosion, erosion- wear, and fatigue. This reduces failure problems in power plants that com- promise the integrity, effectiveness, and lifespan of essential heat exchanger components, such as boiler tubes. The Olkaria V power station in Kenya is one of the facilities that use shell and tube heat exchangers. These heat exchangers were investigated in the present study for failure and it was found that hydrogen embrittlement and sulfide stress cracking caused their prema- ture failure. A recommendation was reached that the frequency of corrosion failure in process industries can be reduced by redesigning tubes to conform to operating conditions and using hybrid materials as surface modifiers. Func- tionally graded materials (FGM) were utilized as advanced hybrid materials that can mitigate degradation by varying material composition. Addition- ally, laser cladding surface modification was employed to join stainless steel 316L and Inconel 625 dissimilar materials on a pure copper substrate to pro- duce quality coatings with enhanced quality characteristics. This attributes include a higher microhardness (MH), and aspect ratio (AR), whereas sur- face roughness (SR), and porosity (P) are minimized. Meanwhile, improper material selection and inappropriate control of the laser cladding process and material parameters affect the quality and performance of fabricated FGM coatings, accelerating failure during service. As such, the present study em- ployed a hybrid optimization of process parameters by combining the Taguchi grey relational analysis (GRA) and artificial neural network (ANN) method to improve output characteristics. Characterization was carried out to observe the microstructure using optical image microscopy and scanning electron mi- croscopy equipped with energy dispersive spectroscopy (SEM-EDS). Phaseidentification was investigated using x-ray diffraction analysis and stress dis- tribution with a residual stress analyzer. Mechanical tests were carried out using a microhardness tester for microhardness and surface roughness profiler for surface roughness. Findings from this study revealed that 600 W laser power, 700 mm/min scan speed, and 1.5 g/min of powder flow rate gave the best optimal process parameters exhibiting desirable material properties with a micro hardness of 257.41 HV, aspect ratio of 3.89 mm, surface roughness of 5.31 μm, and porosity of 0.01 %. When varied between 400 and 600 mm/min, the scan speed was found to be the most significant parameter that influences the qualities of the clad, while laser power was varied between 700 and 1000 W, and powder flow rate between 2 and 6 g/min. The outcome of the Taguchi- grey relational analysis showed that it is a powerful tool for optimizing the quality characteristics of FGMs when combined with the artificial neural net- work method because the experimental results were improved by 16.4 %. The Optical and SEM micrographs showed a microstructural transformation from equiaxed structure to columnar and dendritic structure due to steep temper- ature gradient. The FGM was also characterized by increased laves phases and γ-dendrite in the interdendritic area due to solid solution strengthening of IN625, resulting in higher micro hardness properties. Heat treatment was also carried out using water quenching process to alleviate the tensile residual stresses of +ve 8 Mpa induced during laser cladding, to compressive residual stresses of -ve 136 MP, because tensile residual stresses can aggravate

stress cracking in boiler pipes. This study has successfully developed optimized Fe/Ni FGM on pure copper that has not been adequately explored and can be successfully used for coating boiler tubes.

CHAPTER ONE

INTRODUCTION

1.1 Chapter Overview

This chapter provides an overview of the utilization of functionally graded materials in mitigating heat exchanger material deterioration. The failure analysis case study conducted for the heat exchanger at Olkaria V geothermal power plant is described in detail. Additionally, manufacturing of IN625/SS316L FGM on a pure copper substrate is proposed for mitigating failure. Laser cladding as a suitable manufacturing process for fabricating FGMs is elucidated, as well as the effects of the laser cladding process and material parameters on the quality characteristics. Finally, the enhancement of FGM clads utilizing hybrid optimization techniques combining the Taguchi-grey relational analysis and artificial neural network is explained.

1.2 Background

Surface modification is crucial for engineering components exposed to harsh operating conditions (Uenishi et al., 2007; Weng et al., 2014). This is meant to reduce material degradation and prevent premature failure of engineering components, which can lead to high maintenance costs and reduced output. Alloys were initially used as surface modifiers but are usually insufficient in other desirable material properties, resulting in accelerated failure (Islam, 2019).

Consequently, functionally graded materials (FGMs) have received much attention from materials experts to circumvent the limitations of individual alloy coatings. FGMs are realized from a combination of different materials with properties that vary spatially by composition and/or microstructural profile to perform an intended function at a specific part location (Cpm et al., 2014; Li et al., 2022; Miteva, 2014; Sathish et al., 2021), as shown in Figure 1.1.

Materials scientists in Japan created FGMs in the early 1980s to lessen extreme thermal gradients and high surface temperatures in a space plane project. The operational mechanism of FGM can be compared to the way bones and teeth of the human body

function. The human tooth is ductile on the inside and gradually changes to be wear-resistant on the outside surface to lengthen the tooth's lifespan (Mahamood et al., 2012). Similarly, FGMs can be used to coat boiler pipes specifically to provide corrosion protection on the exterior tube wall and change properties gradually to offer wear resistance on the interior tube wall. This is because heat exchangers carry deteriorating fluids at high pressures and temperatures, which can erode the protective material layer, resulting in failure mechanisms such as erosion-wear and induced corrosion cracking (Faes et al., 2019; Hruska et al., 2022; Imran, 2014).

FGMs are of great interest in many other industries, such as the power generation, chemical, thermal, aviation, military, and biomedical industry, to mitigate the premature failure of components. Several additive manufacturing (AM) techniques have been employed in the fabrication of FGMs. This includes techniques such as powder bed fusion (PBF) and directed energy deposition (DED), also referred to as laser cladding (LC) and laser metal deposition (LMD) (Ghanavati & Naffakh-Moosavy, 2021; Hotz et al., 2021; Jim´enez et al., 2021; Yan et al., 2020). Laser Cladding (LC) is a surface modification technique that melts powders using a laser beam and blends them to form a thin film onto a substrate (base material). Powders of different properties can be mixed through the powder nozzle to form a metallurgical bond with the substrate due to its rapid solidification mechanism (Liu et al., 2021; Zhu et al., 2021).

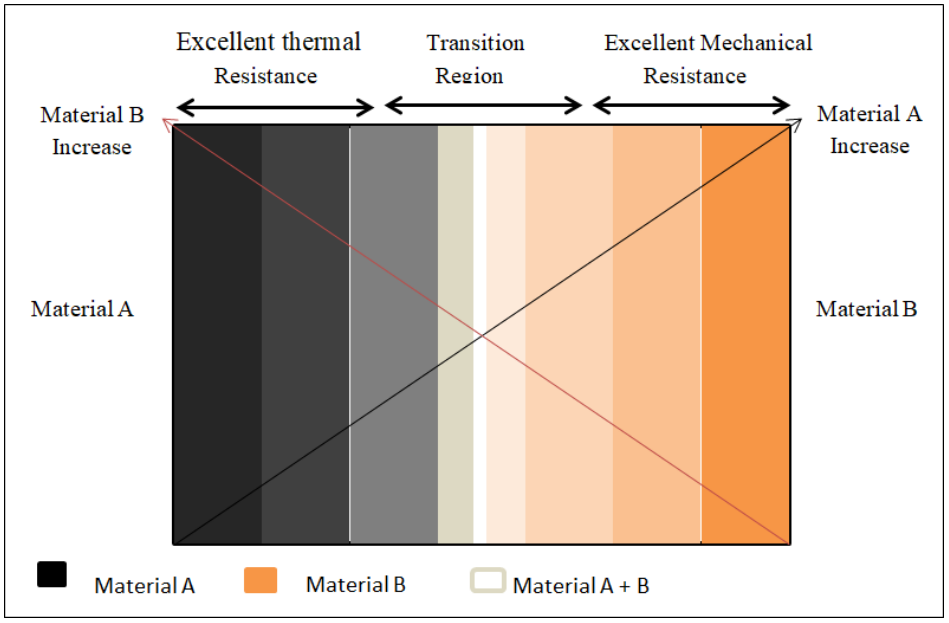

Figure 1.1: Illustration of the Laser Cladding Process in Fabricating Functionally Graded Materials

A carrier nozzle, usually argon gas, is used to drive the powder from the hopper feeding system into a melt pool to avoid oxidation, which is undesirable in the fabricated material, as shown in Figure 1.2. LC was selected in this study because it produces high-quality coatings with good metallurgical bonds and low dilution with the substrate. It is also used to modify the surface by introducing materials with enhanced properties to extend the component lifespan, especially boiler tubes (Siddiqui & Dubey, 2021).

The ever-increasing demand for FGMs for improved system performance, lightweight and hybrid structures, improved material performance, and functionality across industries has seen FGMs being used to overcome other industrial challenges, such as corrosion, pressure, and wear resistance. To achieve this, dissimilar materials were established, a phenomenon that involves the art of joining materials that are difficult to join with different physical properties. Amongst the joining of dissimilar materials, copper and stainless steel have been an area of interest in the fabrication of high-performance boiler pipes (Elijah, 2009; Rodriguez et al., 2019).

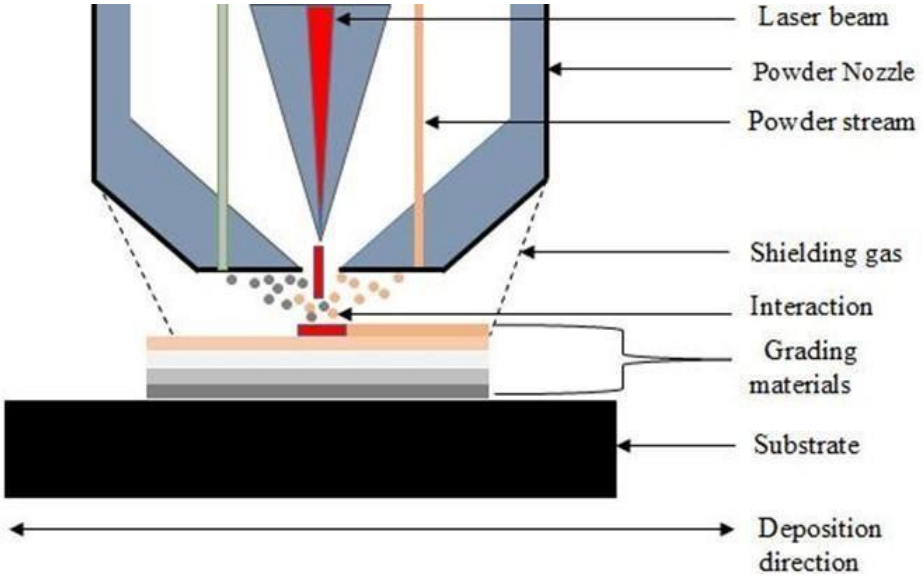

Figure 1.2: Schematic Structure and Properties of Functionally Graded Materials

Despite being adopted due to its high thermal conductivity and high electrical conductivity, copper and its alloys suffer from poor wear resistance and low hardness, which limits their application in heat exchanger piping (Jiang et al., 2021). Therefore, stainless steel, in particular, stainless steel 316L (SS316L) is proposed by researchers for combination with copper due to its excellent strength and excellent corrosion resistance, especially to chloride-containing media. However, joining copper and stainless steel is a challenge because the two are dissimilar materials (Zhang et al., 2021). Joining dissimilar materials can result in processing deformities such as cracks and pore formation which weaken the material quality, making them prone to degrading attacks. Meanwhile, interlayers can be used when depositing dissimilar materials to overcome mismatches in material properties and processing deformities.

For instance, Zhang used Inconel 718 as an interlayer between Cu and SS316L. The authors used directed energy deposition technique to fabricate the FGMs and concluded that IN718 is a good interlayer that forms a good metallurgical bond with the two dissimilar materials. This can be attributed to the fact that IN718 forms a solid solution when it combines with copper, forming a strong metallurgical bond. Solid solution is a strengthening mechanism in which alloying elements diffuse into the crystal structure of another material in liquid state. This leads to the solute, in this case IN718 atom, inducing strains to the crystal structure of copper, leading to dislocation

movement as shown in Fig.1.2a This leads to increased tensile strength and yield change due to tensile strains exerted on the crystal lattice. Complete dissolution leads to formation of a homogeneous microstructure (singe phase gamma bond). However, partial dissolution leads to formation of coarse gamma double prime bond (Pouranvari, 2015). Consequently, enhancing the attributes such as hardness when dislocation movement is hindered by disruption to the crystal lattice (Mouritz et al., 2012)

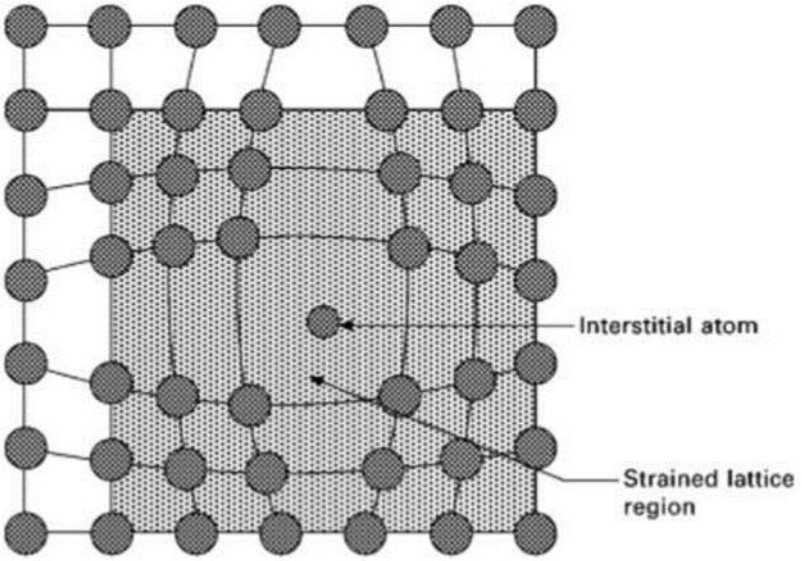

Figure 1.2a: Solid Solution Strengthening Substitutional Mechanism of Solute in Lattice Structure

Source: (Mouritz et al., 2012)

This shows that super alloys are desirable as interlayers between Cu and SS316L. Thus, there is a need to explore the consolidation attributes of other materials that have not been investigated yet such as IN625 (Balu et al., 2015; Reichardt et al., 2021).

Inconel 625 (IN625) is one of the widely utilized superalloys for high-temperature applications due to its high strength and excellent corrosion resistance to thermal and chemical degradation environments (Nguejio et al., 2019; Salavati, 2016).

Thus, combining IN625 with copper can improve its low thermal conductivity properties. For instance, Pan et al. (2020) fabricated a bi-metallic structure of IN625 on Copper 110 substrate using the directed energy deposition technique. They used the

laser flush method to measure the thermal diffusivity of the bi- metallic structure, which showed about 100% improvement of the deposited IN625 when compared to pure IN625. This shows that the material properties of IN625 can be significantly enhanced by combining with Cu alloys. For this reason, IN625 was chosen in this study to fabricate In625/SS316L FGM on the copper substrate because it is compatible with both stainless steel and copper.

In addition, the tensile strength of IN625 is higher than that of SS316L. IN625 can also improve the properties of SS316L, while Cu improves its limitation on thermal conductivity. Using IN625 as an intermediate transition layer can help to avoid brittle intermetallic between SS316L and Cu that can cause cracking, which is not desirable for high-temperature applications. This is because crack deformities during processing can increase the prevalence of stress corrosion cracking. According to Meng et al., 2019, the direct joining of stainless steel to dissimilar materials can result in brittle Fe-Ti intermetallic, which is the leading cause of cracking. They indicated that using an intermetallic layer that acts as a transition material can significantly reduce these reported cracks.

Some of the well-known optimization techniques include the Taguchi method (TM), Response Surface Methodology (RSM), Generic Algorithm (GA), Grey Relational Analysis (GRA), and Artificial Neural Network (ANN) (Kumar et al., 2015; Scala et al., 2013; Kant, 2017; Marrey et al., 2019; Mondal et al., 2012; Nukman et al., 2013; Saqib et al., 2014; Tomaz et al., 2021). This study employed hybrid optimization combining Taguchi-GRA and ANN techniques to improve the quality characteristics of the fabricated FGM. The Taguchi methodology was developed in the 1950s by a Japanese engineer named Genechi Taguchi as a statical tool for quality control. Meanwhile, the Taguchi and GRA methods are limited in optimizing performance characteristics using non-linear relationships (Buldum et al., 2012; Kumar et al., 2015; Pan et al., 2007; Lian et al., 2019).

Despite the abilities of the Taguchi-GRA method, there is still a need to compute large data sets of unknown complex experimental combinations with nonlinear relations. Hence, the ANN method has emerged to overcome this limitation because it employs

computational algorithms to independently assess non-linear statistical models. Because of that, experts have combined the Taguchi-GRA method with ANN as a hybrid optimization technique to yield desirable results. Stojanovic et al. (2016) examined the AlSi7Mg composite parameters using Taguchi and predicted the wear properties using the ANN method. Experiments were carried out using a sliding contact test and L18 orthogonal array parameters. The authors were successful in wear rate prediction using the feed-forward back- propagation ANN method. It was found that the wear rate of the AlSi7Mg composite increases with an increase in the sliding speed and the normal load, showing that Taguchi and ANN can be employed to enhance different performance characteristics.

Kumar and co-investigators conducted a study to optimize neural network parameters using the Taguchi-grey relational and showed that it is an effective methodology for improving performance. Deng et al. (2020) investigated quality improvement using the ANN method and discovered that it is also a proper computational technique for developing relations between quality characteristics and process parameters. Similarly, Nukman et al. (2013) also employed feed- forward back-propagation ANN to predict the process parameters of using Taguchi L_9 and to train the ANN model. It can be seen that the Taguchi method and the ANN method can be used successfully together for predicting and optimizing the quality characteristics of coatings.

In summary, the material characteristics of individual alloy coatings are inadequate in hostile working conditions. Therefore, the use of FGMs with integrated material qualities is necessary. Furthermore, laser cladding process parameters must be optimized to produce higher-quality properties that can enhance the resilience of engineering components such as boiler pipes. The case study of a failure mechanism in the power-generating industry is detailed in the next section to explain why this research was carried out to address the occurrence of the same problem.

1.3 Heat Exchangers at Olkaria Power Plant

Due to the increased energy consumption brought on by population expansion, high-performance heat exchangers used in power generation sectors are becoming more and more necessary. However, most heat exchanger failures are linked to degradation

mechanisms such as corrosion erosion, corrosion cracking, and corrosion fatigue. Consequently, the failure analysis for a shell and tube heat exchanger (see Figure 1.3a) at Kenya's Olkaria V Power Station was carried out in the current study. The heat exchanger was made of copper tubes stacked into a tube bundle, as shown in Figure 1.3b.

Furthermore, the heat exchanger was operating in extreme temperatures and pressures, which are considered hostile working conditions that can aggravate degradation. Figure 1.3 is a schematic illustration of the flow configuration and the conditions of service.

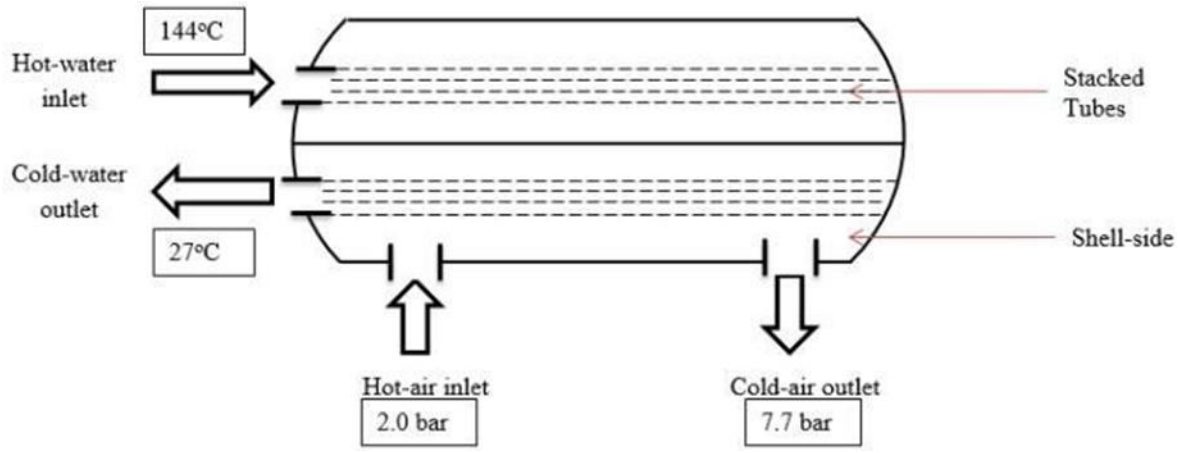

Figure 1.2b: Heat Exchanger Schematic Illustration of the Operating Conditions and Configuration

Figure 1.3: Failed Shell and Tube Heat Exchanger (a) General View of the Shell (b) Internal Stacked Copper Tubes

1.4 Statement of the Problem

Heat exchangers carry fluids at elevated temperatures that flow at high pressure and contain degrading chemicals such as wet hydrogen sulphide. Fluid pressure removes the protective material film that is usually introduced to the surface through a coating, leading to wear erosion and penetration of atomic hydrogen that weaken the microstructural integrity. This also leads to spontaneous interaction of the metallic surface with the environment making it susceptible to oxidation and localized forms of corrosion such as sulphide stress cracking when the material is stressed.

Also, the presence of chemically degrading agents in the fluid, such as chlorine, contributes to surface degradation due to chemical reactions with the metallic surface (Faes et al., 2019). Consequently, the increase of mechanical defects and erosion of the protective layer due to structural, metallurgical, the presence of surface degrading agents, and environmental factors are attributed to the reduced heat transfer process and failure of the heat exchanger piping system. In addition, deep pits can lead to perforations in the heat exchanger tubes leading to the escape of gaseous substances to the environment, which poses a significant health hazard to the surroundings. Failure leads to high maintenance costs across various process industries such as power plants,

petrochemical, and transportation industries due to the repair of worn-out or blocked heat exchanger tubes.

The surface modification technique can be the solution to these challenges. However, there is a need for critical material selection of coatings that can withstand harsh environmental conditions. The unsuccessful deposition of FGMs in the past has adversely impacted the fabrication of quality coating manufacturing materials, resulting in poorly developed mechanical properties that cannot endure degradation. Previously, copper and stainless steel FGMs have been attributed to having cracks and pores in the coating resulting from internal stresses, thermal shocks, and the formation of undesirable phases in the material which lowers functional performance. In addition, delamination during the fabrication of FGMs has resulted in undesirable materials with undesirable processing deformities, especially at the joint interface (Balu et al., 2015).

In recent years, there have been many attempts to investigate the influence of process parameters in FGMs fabricated by laser cladding additive manufacturing techniques. However, the processing deformities such as cracking, and porosity when joining dissimilar materials have become a major drawback in implementing this technique. This undesirable quality characteristic of porosity remains a major challenge in heat exchanger material fabrication. Ralls et al. (2020) revealed that this can be improved by optimizing process parameters. Inspired by this work, optimization techniques were employed to determine suitable parameters. This current study utilized the hybrid optimization technique combining Taguchi GRA and ANN to determine the best laser cladding process parameter that yields a higher grey relational grade (GRG).

Process parameter optimization is the motivation of this work to mitigate the prevalence of deformities in laser-cladded FGMs, for heat exchanger applications.

15 Objectives

The main objective is to optimize the quality characteristics of laser cladding functionally graded material for efficient application in heat exchangers.

1.5.1 Specific Objectives

To achieve the main objective, the following specific objectives were realized.

i. To carry out failure analysis and identify suitable candidate materials to clad boiler pipes and determine optimum laser cladding process parameters.
ii. To determine the effects of the LC process and material parameters on the microstructural evolution, surface characteristics, mechanical properties, and wear resistance of the fabricated FGM, for improved resilience of the heat exchanger in severe operating conditions.
iii. To optimize the quality characteristics of the FGM coating (microhardness, aspect ratio, surface roughness, porosity) via a hybrid optimization technique combining Taguchi grey relational analysis and artificial neural network methods.

1.6 Justification of the Study

This thesis made it possible to find potential coating materials for heat exchangers working in harsh environments. As such, this study will mitigate failure encountered in power plants and reduce the high maintenance costs. Using an emerging additive manufacturing approach termed laser cladding surface modification, deterioration can be reduced because of the superior material properties surpassing traditional manufacturing techniques' constraints.

Additionally, it aids in reducing the frequency of failure, which raises maintenance and replacement expenses. This requires a significant amount of the required capital, but because such failures will be less frequent or non-existent, process industries can save money and use it for business development and other projects that will increase revenue. Also, it gives room to reduce production halts brought on by heat exchanger failures, a problem that costs most businesses huge sums of money. Both process firms and the retail energy market will see an increase in revenue as a result of heat exchangers' efficient performance. In addition, a successful choice of material and process parameters aids in avoiding heat exchanger failure that could result in tube leakage and the release of toxic compounds into the atmosphere. Furthermore, because

some heat exchangers are employed in the food processing industry, fluid contact might result in the processing of the most toxic foods. As a result, this effort sought to end such crises that harm not only people but also the environment by polluting it to the point that even plants find it uninhabitable. This study was conducted so that the outcomes can significantly contribute to maintaining the ecosystem.

Additionally, when the artificial neural network model was created, it made it possible to build crucial information for future reference. Any other material or process parameters covered by the experimental domain of this study can now be optimized by scholars or researchers using the created optimization model. By doing this, users may encourage the growth of advanced manufacturing research centres, improve human capital development in Africa and around the world, and reduce the gap between academics and industry. Utilizing the findings from this study, the academic community can adopt the recently developing concept of incorporating machine learning into laser additive manufacturing procedures to use this effective and rapid prototyping method to address most of the important industrial concerns.

17 Scope of the Study

As noted, several candidate materials for making heat exchangers exist. For instance, metals (iron-based, nickel-based superalloys, titanium alloys, ceramics (monolithic, ceramic matrix composites), and polymers/plastics (PLA, Polymethacrylate) can all be used to create heat exchangers. However, due to their thermal conductivity, thermal expansion, performance, and efficiency under harsh climatic circumstances, metallic materials were the main focus of this study for the construction of heat exchangers. In a similar disposition, several additive manufacturing processes can create high-performance heat exchangers. For instance, powder bed fusion (selective laser melting), binder jetting (inkjet 3D printing), and directed energy deposition (laser cladding). However, due to its demonstrated skills in laying heat exchanger coatings with minimal dispersion and good metallurgical bonding, this study restricted its analysis to laser cladding.

The breakdown of heat exchangers or the decline in performance efficiency is related to many variables. Besides, there are numerous heat exchangers, including plate-type,

shell and tube, double pipe, condensers, and air-cooled models. The most adaptable type of heat exchanger, shell and tube, was the subject of this study. Moreover, several phenomena, including tube erosion, tube corrosion/oxidation, thermal fatigue, tube pitting, and steam/water hammer, are reported to contribute to such devices' failure pressure and pressure and pressure decrease. The primary focus of this investigation was a failure due to erosion-wear and corrosion since these two causes account for the majority of failures. Because of this, only wear testing was adopted for analysis.

Finally, hybrid optimization was carried out by combining Taguchi-grey relational analysis and Artificial Neural Network to obtain suitable process parameters for laser cladding of the FGM. The present study was limited to only Taguchi GRA and ANN hybrid optimization without employing other common optimization models such as response surface modelling, generic algorithm, regression models, and analysis of variance method because studies have proven them effective in the domain of these experimental work as compared to other types mentioned.

In conclusion, only three input parameters (laser power, scan speed, and powder flow rate) were employed because they have the most influence on the quality characteristics compared to the stand-off distance, shielding-gas flow rate, and laser spot diameter. Moreover, this study was limited to optimizing the laser clad material qualities including hardness, surface finish, and aspect ratio, without focusing on the corrosion behavior of the coating. Moreover, the aim was not to optimize the heat exchanger heat transfer properties or corrosion characteristics.

Future study is recommended based on the time-constraints and resources availed for the successful completion of this study.

1.8 Organization of the Thesis

There are five chapters in this thesis. The first chapter introduces laser-cladded FGMs, heat exchangers and failure analysis conducted, problem statement, objectives, scope, and justification of the study. The nature of the shell and tube heat exchanger degradation mechanism and methods for reducing it by using novel materials are also provided in Chapter Two. Chapter three describes the procedure for fabricating,

characterizing, and examining In625/SS316L FGM. The findings from the failure analysis of the heat exchanger tubes are presented in Chapter Four, together with the outcomes of the FGM fabrication process, including measurements of microstructural analysis, microhardness, porosity, X-ray analysis, and residual stresses. The results for the Taguchi GRA-ANN optimization procedure are also detailed in this section. The conclusion on the results and recommendations for further research to enhance the quality of HX FGMs are presented in Chapter Five.

CHAPTER TWO

LITERATURE REVIEW

2.1 Chapter Overview

This chapter gives an overview of heat exchangers and further explains the shell and tube heat exchangers because it is the most predominant. The nature of degradation is explored due to the significant number of documented failures in literature, particularly on power plants. Functionally graded materials considered to mitigate failure are varied. Laser cladding as an appropriate processing method for FGMs is provided, with special emphasis on the impact of process and material parameters. Finally, the optimization of the laser cladding process is explored to reduce or eliminate processing defects affecting the quality of fabricated heat exchanger parts.

2.2 Shell and Tube Heat Exchanger

The use of heat exchangers is growing rapidly in the power plant industries to meet the rising electricity demand brought on by a growing population. The device transfers thermal energy, or heat, between liquid or gaseous fluids (Banjare et al., 2015; McDonald and Magande, 2012; Sidebotham, 2015). These devices are frequently used in the organic Rankine cycle, in which heat from geothermal wells is converted into mechanical energy and propels turbines that generate electricity (Franco and Vaccaro, 2017). As a result, the industry has designed various heat exchanger types specifically for this usage. This includes cooling towers, condensers, evaporators, shell and tube types, plate types, and condensers (Vasiliev, 2005; Chen et al.,2012).

The shell and tube heat exchanger is the most often used because of its wide range of uses in various environmental settings, efficiency, suitability in high-pressure applications, affordability that has increased processing capacity (Patel & Mavani, 2012), and the high ratio of heat transfer area to volume and weight (Jin et al., 2021; Master et al., 2006). Meanwhile, several process industries have observed numerous shell and tube heat exchanger failures. When attempting to tackle this issue, a starting

point is to understand their working principle, the nature of degradation, and the ways of prevention.

2.2.1 Working Principle of the Shell and Tube Heat Exchanger

The shell and tube heat exchanger is made up of several tubes that are stacked inside a shell and are divided at the ends by tube sheets. The interior looped tubes of a shell and tube heat exchanger circulate a colder liquid while a hot liquid circulates in the shell side, which is the outer enclosed space, or vice versa. The warmer liquid is heated while the colder fluid is chilled through the fluid outlet and inlet tubes, as a thermal exchange mechanism, as shown in Figure 2.1. The process can be categorized based on the flow configuration, which includes the forms of fluid flow that are parallel, cross, or counter, see Figure 2.2 (Zohuri, 2017).

The fluids enter the heat exchanger chambers simultaneously in the parallel flow type with higher temperatures and flow in a parallel direction to cause the parallel tubes with various temperatures to approach one another. Two fluids enter the exchanger from opposite ends and flow in distinct directions when the exchanger is of the counterflow kind. Counterflow-type exchangers are the most inherently efficient since they produce a consistently higher temperature difference between two fluids (Abeykoon, 2014).

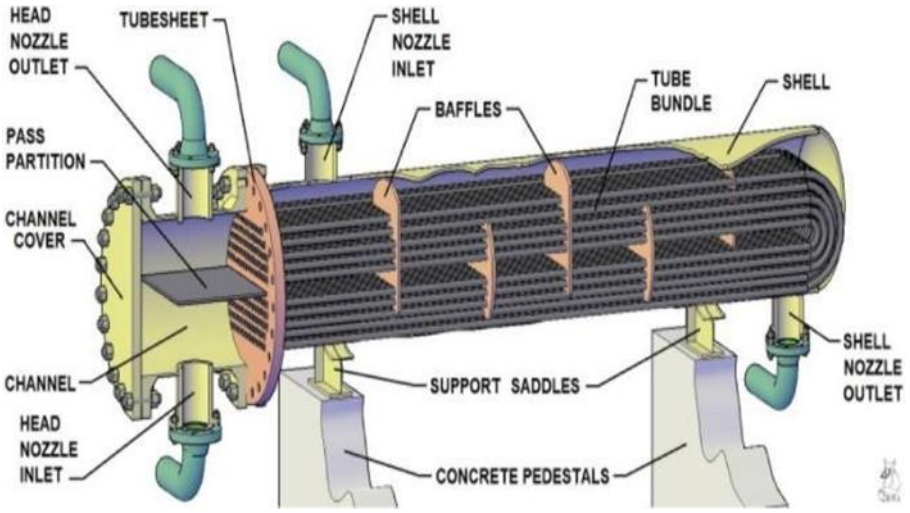

Figure 2.1: Structure of a Shell and Tube Heat Exchanger

Source: (Parisher, 2001)

When two fluids move in opposite directions around an exchanger, the flow pattern is known as cross flow. They are typically utilized in 2-phase flow processes like steam condensers. Recently designed heat exchangers employ a combination of different flow configurations because they combine several flow configurations (Bichkar et al., 2018; Zohuri, 2017).

Shell and tube heat exchangers are advantageous in process industries because of the effective heat transfer process, which can be built in the order of millimetres with a tube size of 16mm to 38mm for most conventional heat exchangers (Bichkar et al., 2018). This design criterion ensures an increase in the heat transfer rate because a smaller surface area will result in more turbulence, which will increase heat transfer (Johnson et al., 2020). Meanwhile, the use of boiler tubes can lead to clogging that might need frequent cleaning. Moreover, geothermal fluid residual deposits might result in failure and blockage of the heat transfer surface. It is crucial to comprehend the mechanism of deterioration in exchanger tubes to apply prevention measures.

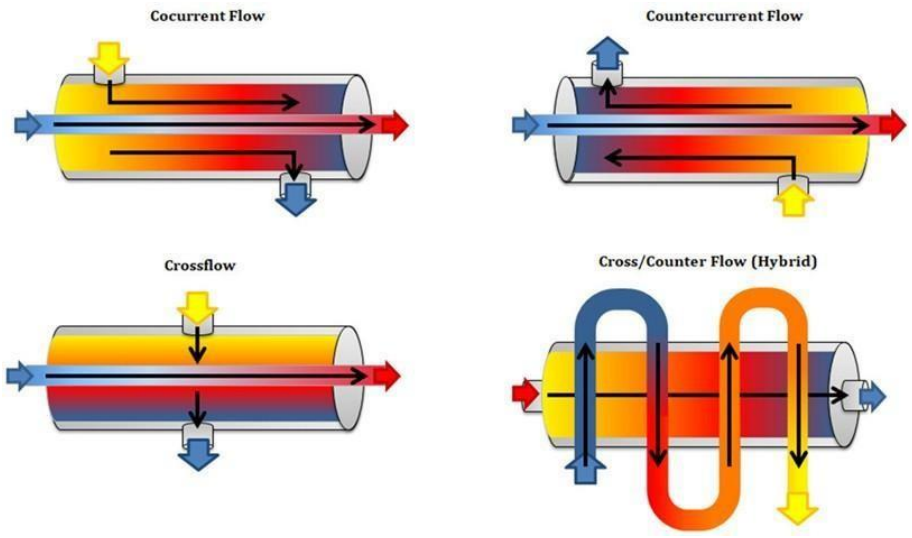

Figure 2.2: Flow Configuration of Fluids in Heat Exchangers

Source: (Martinez, 1995)

2.3 Failure Mechanisms in Shell and Tube Heat Exchangers

Corrosion, fouling, wear erosion, oxidation, vibrations, and fatigue are the main causes of tube failure, which are attributed to coating defects and unfavorable working conditions. Hence, this study strongly emphasizes the effective prevention of metal erosion and corrosion since they are the most frequently encountered failure mechanism in power plants and are the primary cause of the failed shell and tube heat exchanger under investigation (Faes et al., 2019).

Metal erosion occurs when fluids moving at high velocity wash away the metal protective surface leading to susceptibility to attack. For instance, erosion due to suspended solid particles moving at extreme velocity was found to have caused the failure of heat exchanger copper tubes used in industrial cooling of heat from 16

°C to 4 °C (Kuznicka, 2009). The shell and tube heat exchanger prematurely failed due to material degradation, which was accelerated by attacks from chloride- enriched water in a sulfate-concentrated environment. Wear can occur with corrosion-induced attacks as the main cause of failure. The process of tube surface deterioration as a result of chemical reactions in unfavorable conditions is known as tube corrosion (Faes et

al., 2019). Some of the hostile mediums include untreated industrial water with corrosive media such as chlorides, sulfates, and reducing acids (Ishii et al., 2002).

The interaction of alloys with harmful oxides formed by oxidizing reactions is what triggers boiler tube corrosion during operation (Sadeghi et al., 2019). In this case, metal often converts to rust which then blocks the heat transfer surface area, leading to pressure drops. Chlorine-induced corrosion is the most common type of corrosion in shell and tube heat exchangers because it can be aggravated by salt deposits and gaseous contaminants that react with the tube material and penetrate the surface (Wu et al., 2020). This is explained by the existence of manufacturing imperfections such as pores and cracks that act as a way for oxide passage. For instance, the presence of high chlorine content at the microstructural interface of a biomass boiler was reported by Oksa et al., (2014), causing a chemical reaction that led to a chlorine corrosion attack of the tube material, see Figure 2.3.

Uusitalo et al. (2004) observed a similar pattern of chlorine-induced attack when researching low-alloy stainless steel and austenitic stainless steel fabricated via the laser cladding and high-velocity oxy-fuel (HVOF) technique. They observed the disintegration of the microstructure at the splat boundaries of Ni-50Cr coating. This implies that corrosion can be reduced by producing quality coatings that can withstand degradation.

Furthermore, hostile operating conditions can aggravate the occurrence of corrosion-related failures. Wu et al. (2020) investigated the performance of two boiler tubes operating at 520 °C – 540 °C. The boiler tubes that were coated with Ni2Al3 were investigated in different temperature environments. Two failure counts were reported for the boiler tube operating at constant temperatures and monitored at constant range while 213 failure counts were reported for the boiler tube experiencing temperature fluctuations.

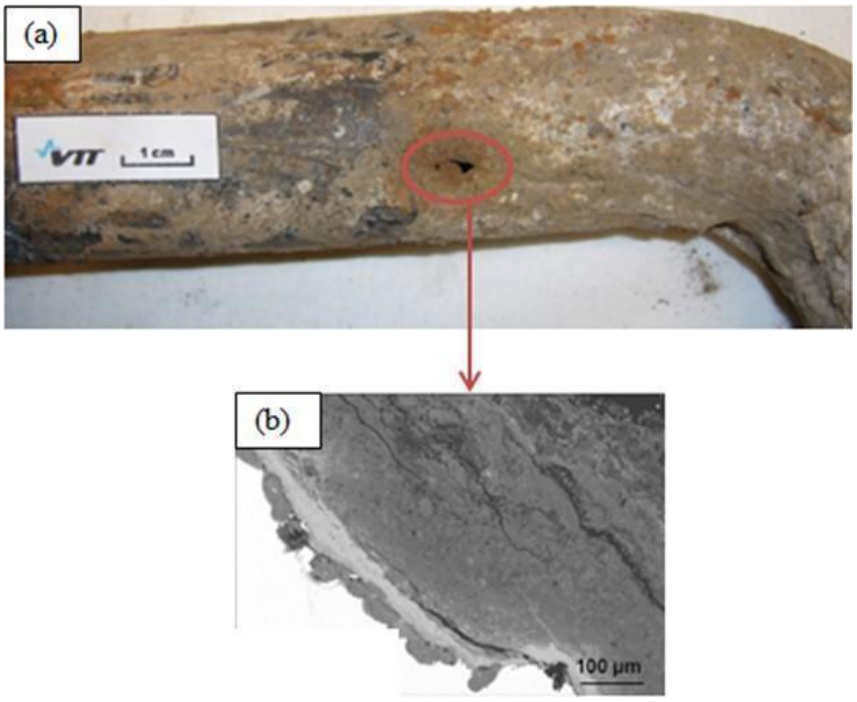

Figure 2.3: Chlorine-Induced Tube Failure Causing (a) Tube Leakage Observed and (b) Microstructural Crack Propagation at the Interface

Source: Oksa et al. (2014)

Figure 2.4 elucidates the attack at the coating's microstructural grains leading to tube corrosion. It can therefore be inferred that tubes operating in elevated temperatures require materials with good microstructural quality characteristics. Several distinct forms of corrosion, including pitting corrosion, stress corrosion cracking (SCC), galvanic corrosion, general corrosion, and crevice corrosion, attack boiler tubes. The failed exchanger tubes investigated in this thesis are attributed to SCC and pitting corrosion. Pitting corrosion is one of the most common types of localized corrosion, which creates holes or pits in the tube material, allowing fluids to escape and pressure drops. It is regarded as the most hazardous type of corrosion since it poses a threat to numerous lives due to environmental risk factors like explosions and potentially damaging effects when harmful substances escape.

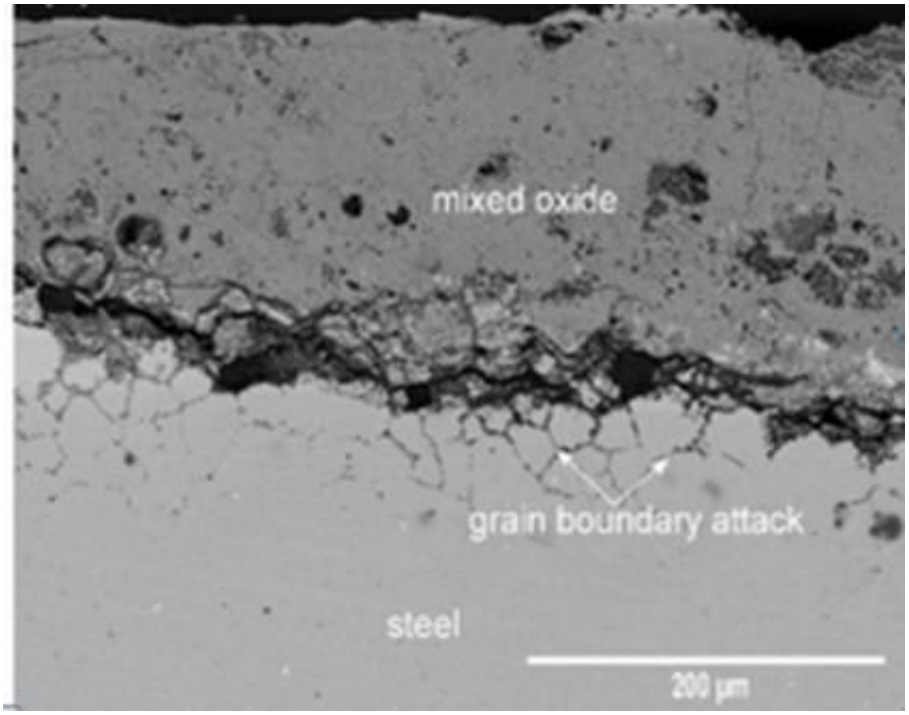

Figure 2.4: Corrosion attack on the Microstructural Grain Boundary of a Boiler Tube Operating in Hostile Temperature Conditions

Source: (Wu et al., 2020)

Stress corrosion cracking is another form of corrosion that causes cracking of the tube surface in the combination of tensile stresses, corrosive media, and moisture (Jin et al., 2021; Albanakis et al., 2009). For instance, Corleto & Argade (2017) observed crack propagation in Duplex SS and Carbon steel exchanger joints due to stress rupture that led to stress corrosion cracking. This shows that resilient materials with high tensile strength and excellent corrosion resistance are necessary to withstand- ing stress and pressure buildup in tubes to increase the service life.

It is clear from the discussion that corrosion poses a serious challenge to process industries. Therefore, research is needed to enhance material qualities so that they can endure degradation under demanding operating conditions. According to Faes et al. (2019), careful material selection can prevent material failure, which implies that before manufacturing boiler tubes, material selection must be carefully considered in the design stage (Permatasari & Yusuf, 2018). In light of this, some commonly utilized

tube coating materials, their material characteristics, and their microstructural behaviour are discussed in detail.

2.4 Materials for Heat Exchanger Pipes

According to Kapranos & Priestner (1987), viable materials for heat exchangers used in thermal conversion systems include stainless steel, copper-nickel alloys, nickel-based super alloys, aluminum, and titanium alloys. This study focuses only on stainless steel, nickel, and copper alloys because the heat exchanger tube investigated is made of copper alloy. Moreover, the proposed FGM combines stainless steel (SS316L) and Inconel-based super alloy (IN625).

2.4.1 Stainless Steel Substrates and Coatings

Steel is the most widely used tube material due to its strong oxidation-corrosion resistance, structural strength, availability at low costs, and endurance in harsh working conditions. Additionally, their high chromium and nickel content improves their thermal and corrosion resistance (Belsvik et al., 2020; Vasileiou et al., 2021). Different types of steel such as stainless steel, alloy steel, carbon steel, and tool steel have unique characteristics that make them find application in different fields. Stainless steel, particularly the austenitic type finds application in the manufacture of boiler tubes. This is attributed to its good material characteristics such as excellent corrosion resistance, high strength, and excellent formability. A typical example is the stainless steel 304 (SS304) and stainless steel 316 (SS316).

According to Lima et al. (2005), molybdenum can alter these steels' microstructure to improve resistance to pitting corrosion in highly corrosive conditions, making them ideal for power plant applications. Meanwhile, when working at higher temperatures between 400 °C and 850 °C, sensitization to these SS types has been reported to occur. This phenomenon involves chromium depletion and carbide precipitation at the grain boundaries, frequently exposing SS to boiler tube intergranular stress corrosion cracking. Corrosion problems can be solved by lowering the carbon content to levels below 0.3 wt.%, creating a better version known as SS304L and SS316L. However,

when operating at greater temperatures for an extended period, these latter varieties may also be susceptible to sensitization.

Yoo et al. (2022) revealed that SS304L contains a Cr element that offers significant corrosion resistance. However, it often precipitates along the grain boundaries when exposed to temperatures reaching 870 °C, which they attribute to the depletion of Cr along the zone close to the grain boundary, causing intergranular corrosion in heat exchanger tubes. The corrosion behavior of the FeCrAl coating applied to SA213-T11 steel using the thermal spray process for boiler tubes working at high temperatures was also examined (Rezakhani, 2007). They observed that the steels were attacked by salt deposits due to scale formation, demonstrating that scale formation is an industrial issue that causes components to deteriorate. After exposure at 550 °C, the corrosion products were seen.

Figure 2.5 depicts the substrate-coating interface as well as the microstructural cross-section of the coating that was attacked at its grain and splat boundaries. This could be explained by excess chlorine and sulfur reactions leading to the spallation of oxide layers and the depletion of chromium-protecting elements at the grain boundaries. The attack reveals that for improved corrosion resistance, there must be a proper bond with adequate substrate-coating consolidation.

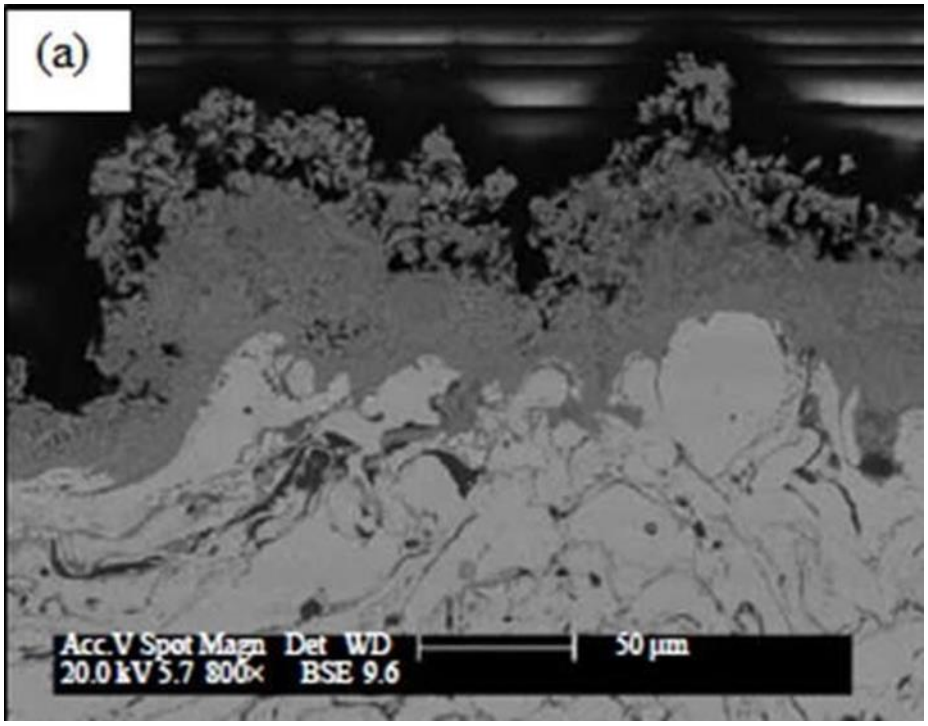

Figure 2.5: Corrosion Attack of FeCrAl Coating Deposited on SA213- T11 Steel Showing the Microstructural Substrate/Coating Interface

Source: Rezakhani (2007)

Voisin et al. (2022) demonstrated that SS316L is less vulnerable to pitting corrosion attack and can function in extremely corrosive environments by forming a major barrier consisting of a Cr_2O_3 film. Due to its larger chromium content, SS316L has excellent corrosion resistance, but it can still corrode if degrading chemicals penetrate the oxide film and create a nucleation site. This suggests that under controlled and optimal processing conditions, pitting corrosion in heat exchanger tubes can be decreased. This is because manufacturing imperfections such as phases, grain boundaries, and crystal dislocations in the microstructure affect performance. Additionally, they reveal that the development of a greater melt pool may serve as the starting for pits, which may be related to the proliferation of cracks along cellular structures.

Research on how melt pools affect pitting corrosion has not been adequately explored. Therefore, future research is required in this area of study to understand how the inclusion of Cr can reduce heat exchanger failures as well as the pit nucleation of

SS316L. Adding additional Cr to stainless steel will boost its corrosion resistance because Cr and oxygen combine to form an anti-corrosion passive layer. Because of that, the stainless steel 304L and 316L kinds are among the most popular choices for heat exchanger tubing due to lower carbon contents and higher chromium contents (10.5%), which enhance their corrosion resistance and mechanical properties.

The austenitic SS-types also possess an austenitic microstructure, which, during directed energy deposition, produces columnar dendritic morphology and typically yields homogeneous grain distribution. It is important to note that the processing method employed affects how the microstructure forms, so different processing methods, like selective laser melting (SLM), may not produce the same microstructure (Saboori et al., 2020). For example, Pokhmurskii et al. (2013) examined the erosion-corrosion behaviour of boiler tubes and concluded that a coating's microstructure is the most crucial factor in determining its oxidation resistance. They investigated the effects of adding alloying elements to the Fe-Cr- Al system, including Ti, Mn, B, Mg, Ni, and Si, and found that for arc-sprayed coatings, the wear resistance of boiler tubes at high temperatures is mostly dependent on the microstructure rather than the microhardness. This is explained by the homogeneity of the distribution of the elements in the coating, which affects how well it protects.

2.4.2 Copper-alloy Substrates and Coatings

Exceptional qualities of copper alloys, a noble ductile metal, include great electrical and thermal conductivity as well as good corrosion resistance. Consequently, it plays a significant role in the development of heat sinks and exchanger pipes that need to have high thermal resistance and effective heat transfer. Oxide coatings that serve as protective layers against corrosion are also produced when copper reacts with water. Mahmood et al. (2018) examined the thermal performance of copper coatings for heat exchangers using a thermal experimental setup. They discovered that the surface properties of copper can be enhanced by increasing the surface area through the microstructural grain size, which enhances heat transmission. This suggests that the choice of material has an impact on heat transmission effectiveness and corrosion

resistance. It also demonstrates how important the surface-to-volume ratio is to coatings made of copper for increased heat transfer.

Because copper has a good thermal conductivity that may reach up to 62%, higher than aluminum and stainless steel, two materials that are reportedly alternatives to copper, they chose copper for their investigation. Additionally, they demonstrated how equipment size reduction might benefit the design of heat exchangers by utilizing the anodized copper coating. This may aid in lowering costs and material waste. However, due to limited service life occasioned by surface degradation, among other things, its low strength, and low hardness, its industrial application is constrained. To get higher material qualities with combined functionality in heat exchanger applications, researchers continue to investigate its alloys.

Schleich (2004) stated that the CuNi 90/10 alloy has the potential as a piping coating material, particularly for marine subsystems. However, they point out that it is susceptible to erosion-corrosion and corrosion damage when utilized in contaminated waterways, emphasizing the need for careful design considerations and material selection before design. Additionally, they discuss how a cuprous film produced by a chemical reaction acts as a defence against corrosion attack, illustrating how copper-nickel alloys like CuNi 90/10 are resistant to some attacks like localized corrosion and can be used successfully in the manufacture of high- temperature devices like heat exchangers. Although copper has high thermal properties, Jin et al. (2021) stated that it is frequently challenging to carry out laser cladding on copper and its alloys. Nonetheless, several coatings can be deposited on copper alloys and still obtain a good metallurgical bond.

For instance, Yan et al. (2012) added TiB_2 and CaF_2 to Ni-Cr coating produced by laser cladding on Cu-Cr-Zn alloy substrate to improve the tribological properties, see Figure 2.6. The addition of TiB2 from 5 wt% to 20 wt% resulted in a microstructural transformation from martensitic structure, to cystic form- dendrites, and reinforced particles, see Figure 2.6. This resulted in improved microhardness reaching 946 $HV_{0.1}$, and improved wear resistance that was 6.32 times better than that of the copper

substrate. This implies that coatings can be used to improve the poor wear resistance of copper and other properties which are dependent on microstructural development.

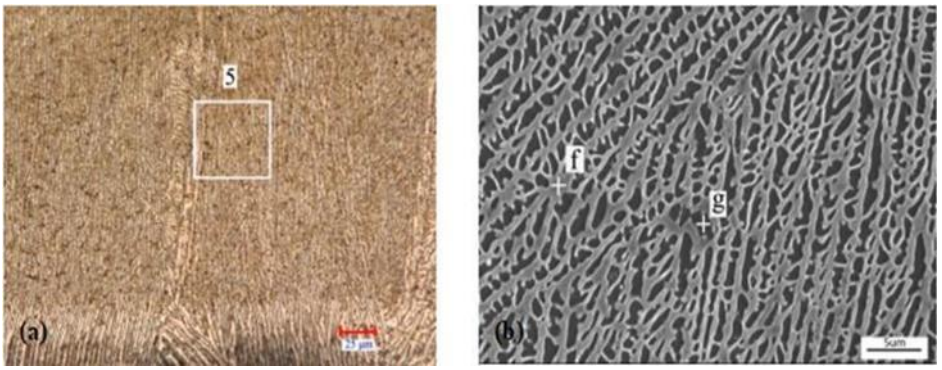

Figure 2.6: Microstructural Refinement in Laser-Cladding Nickel Coatings on a Copper Substrate (a) Martensitic Structure, to Cystic Form- Dendrites (b) Highlighted Square Viewed At a Larger Magnification

Source: (Yan et al., 2012).

Balu et al. (2015) laser-cladded copper substrate with nickel-based alloy to improve its wear resistance properties. The substrate was preheated at 300oC, meant to prevent processing defects caused by poor laser beam coupling, which could also be related to avoiding thermal shock. The coating had different microstructures at different regions analysed due to varying cooling rates as a function of time but exhibited a good consolidation mechanism. The good bond could mean the laser power was sufficient to cause a sufficient melt pool to create a good consolidation with the substrate, while the gas entrapped during laser cladding might have caused the crack formation, which can determine the performance of heat exchanger parts during high-pressure loading, leading to stress corrosion cracking.

Interestingly, it can be seen that copper and Ni-based coatings can form a good metallurgical bond with the substrate, which is desirable when modifying the surface of copper heat exchanger tubes. For example, Lv et al. (2021) successfully deposited Ni60A coating on copper heat exchanger tubes using the plasma cladding method and obtained good structures (Figure 2.7). The phase composition has been characterized by CrB phases with a grey dendritic phase. However, the hardness and wear resistance

have been reported to have decreased at temperatures above 850 °C. Intermetallic can be applied to the component to increase the wear resistance and hardness properties, which shorten the component's service life.

2.4.3 Nickel-based Substrates and Coatings

An alloy comprising nickel, cobalt, or iron as its main constituents is referred to as a superalloy. The alloy's outstanding high-temperature oxidation resistance, creep resistance, corrosion resistance, and erosion resistance are all a result of these base elements. A nickel-based superalloy is the best candidate for heat exchanger applications because it contains essential solutes that are defined by titanium and/or aluminium. The material reportedly possesses

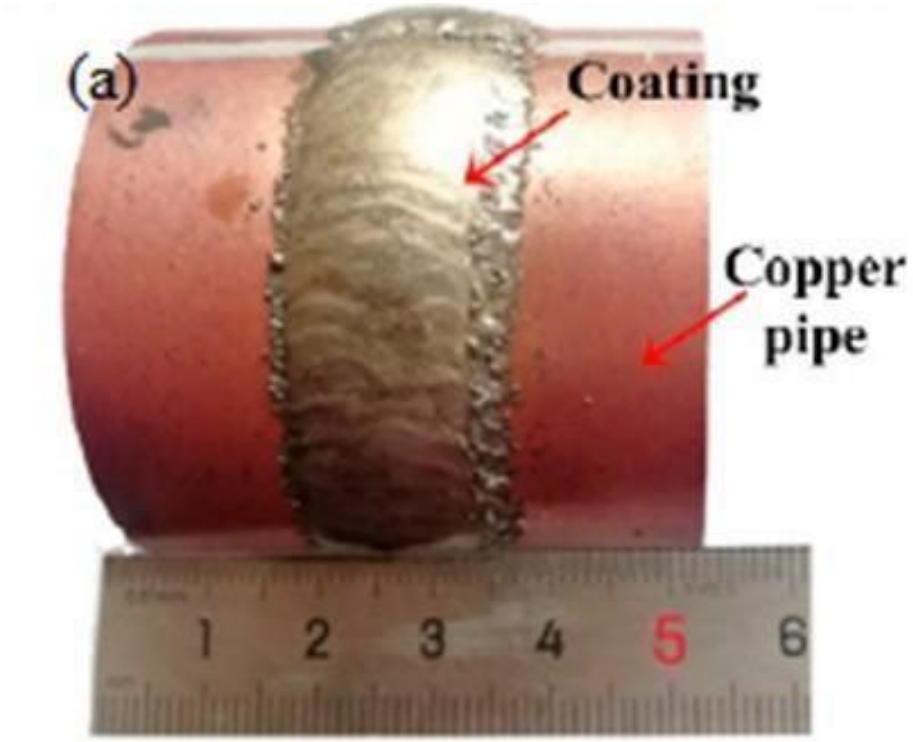

Figure 2.7: Laser Cladding Ni60A on Copper Pipes Original Copper Pipes before Deposition

Source: (Lv et al., 2021)

They have outstanding strength and creep resistance at high temperatures because of an FCC austenitic crystal structure that maintains the equilibrium microstructure and gamma prime (') structure. While in use, some nickel-based alloys, such as NiCrAl, NiCr, and NiCrMo, form oxide scales rich in aluminium that speed up the rate of corrosion protection (Wu et al., 2020).

Nickel-based coatings have also been utilized as boiler tube overlays because they offer great resistance to dry gases, such as carbon dioxide. Conversely, the coatings are harmed when used in environments with chlorine. How metal oxides and chlorine can penetrate nickel coatings is still not entirely clear from the literature. This study discusses how holes and fractures connected to fabrication change the microstructural resistance to corrosion attack.

According to Ahmad (2006), adding scale-forming components like Cr and Al can lengthen the usable life of items and increase the corrosion resistance of nickel coatings. This is due to the stable oxide layer that Cr produces. As a result, the corrosion protection of nickel coatings increases as the Cr content does. By creating a layer of surface protection, Chanda et al. (2020) demonstrated that increasing the Cr concentration increased the Ni-Cr-P coating's resistance to pitting corrosion when applied to AISI 1020 low-carbon steel. Due to the favourable material characteristics, manufacturers of heat exchangers are concentrating their research on using nickel-based coatings in boiler tubes to reduce degradation.

Due to their capacity to function at high temperatures while keeping their superior mechanical qualities, good corrosion resistance, and wear resistance capabilities, researchers have made numerous attempts to deposit additional nickel coatings on various substrate materials (Kracke & Allvac, 2010). Wang et al. (2022) used the laser cladding approach to deposit a coating of a Ni-based alloy on ductile cast iron while adjusting the laser power at 1.6 kW, 2.0 kW, and 2.4 kW. They were able to obtain dendrites that were made up of a dark-grey solid solution phase located inside the dendrites and a bright white eutectic structure that was found between the dendrites.

Because a higher heat input to nickel results in higher melting and a higher molten pool, which results in uniform solidification, which is what achieves component uniformity,

the researchers also noticed less C element segregation in both structures at the highest laser power of 2.4 kW and an increase in the size of the microstructure. As a result, they achieve a microstructure free of defects and with the maximum level of surface integrity possible, which is a desirable quality when applying nickel-based HX coatings.

Zhang et al. (2008) used the laser cladding process in a work comparable to theirs to create a nickel-based coating on a pure copper substrate. A 3.2 kW laser, a powder feed rate of 5.0 g/min, and a scanning speed of 5.0 mm/s were used to produce a strong metallurgical link between the substrate and coating. To combat the copper substrate's high reflectivity when it came into contact with the laser beam, they used a stronger laser and 300 C substrate preheating.

To get around this problem, an intermetallic can be added to the substrate before the coating is applied. This was demonstrated in the research of Wang and colleagues, who added n- Al_2O_3/Ni interlayers to the copper substrate before laser cladding the Ni-Co Duplex coating (Wang et al., 2016). This led to the creation of a defect-free microstructure that had improved microhardness characteristics that were 8.2 times better than those of the copper substrate. They also conducted the XRD and SEM analyses shown in Figure 2.8, and they discovered that the microstructure was made up primarily of the solid solution of nickel with a few metallic silicates and carbides. Therefore, it can be concluded that preheating before laser cladding nickel coatings can help achieve a strong interfacial bond free of cracks, which are frequently observed when brittle borides are created but weren't in this case.

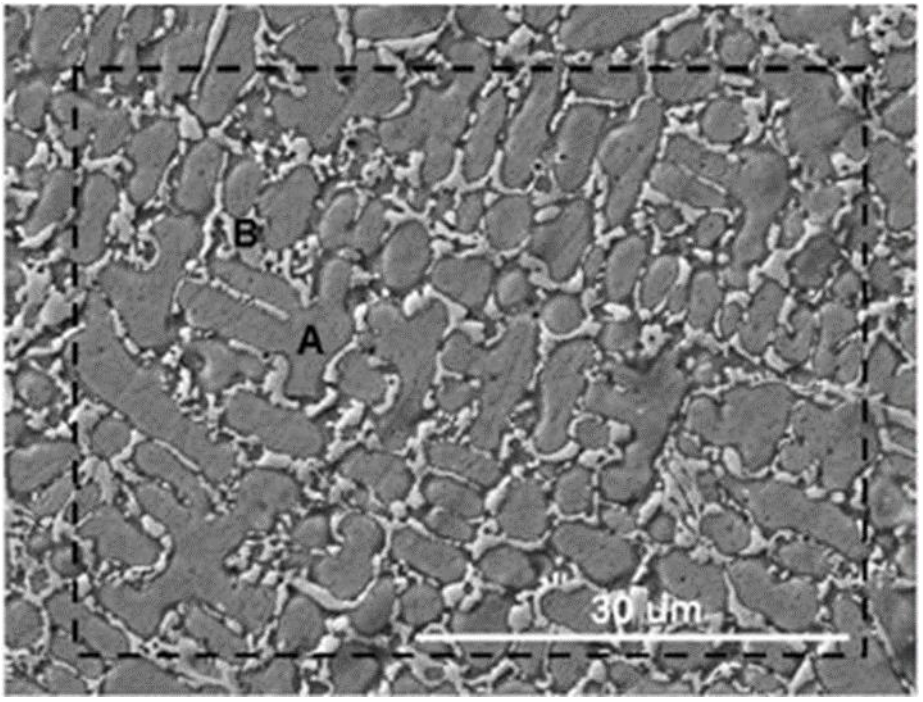

Figure 2.8: SEM Morphology of Nickel-Based Coating Showing: (a) Dendrite (b) Interdendritic Phase

Source: Wang et al. (2016)

Hussain et al. (2013) coated T9 boiler steel with coatings of In625, NiCr, and NiCrAlY. To learn how the deposition flux of alkali-iron tri sulfate affects fireside corrosion, the air-fired combustion gases were simulated at 1300 ppm SO_2 for 1000 hours at a temperature of 650 °C. The NiCr coatings were examined for incubation times underexposure and reached 900 hours, demonstrating the coating's ability as a suitable material for boiler manufacturers. However, adequate investigations are needed to develop the material for increased corrosion resistance. However, IN625 is also said to work well in boilers that burn waste-to-energy, particularly between 400 and 650 °C. Due to its high concentration of Nb, Mo, and Cr, which frequently create a protective layer of Cr_2O_3, including NiO, Nb_2O_3, and $NbCrO_4$, it is found to be efficient at preventing high-temperature oxidation and corrosion when used at elevated temperatures (Cuevas-Arteaga et al., 2010).

The corrosion behavior of nickel-based coatings at high temperatures was examined by Hruska et al. (2022). Two base materials that are candidates for use in biomass

boilers have their performance tested over 5000 hours in an atmosphere with HCl and SO_2. Low alloy steel $16Mo_3$ and austenite stainless steel AISI 310 both demonstrated excellent corrosion resistance with no porosity or oxidation visible, demonstrating their suitability as candidate materials. Dhaiveegan et al. (2016) carried out a similar study in which stainless steel 316L and 304 corrosion behaviour were examined for 3 years of exposure in an industrial, maritime, and urban environment.

In the presence of sulfur gases, particularly while operating at high temperatures, nickel-based superalloys are vulnerable to attack and embrittlement. Despite these drawbacks, it is clear that they have been used in heat exchangers because of their corrosion resistance, suggesting that their level of resistance can be increased for a particular application in heat exchangers. Hastelloy, Inconel 600/625, Chlorimet, Incoloy 825, and Inconel 600/625 were a few of the frequently used nickel-based alloys. Reeks and co-authors asserted that nickel superalloys should be thoroughly examined for the best performance because they are reported to have a complicated composition and new interlayer bonding characteristics (Reeks et al., 2020).

Individual coatings find application as heat exchanger coatings. However, it is also clear that if working conditions pass a certain threshold, they lose their thermo- mechanical properties and are vulnerable to deteriorating attacks in severe conditions. It suggests that a combination of different material properties using multifunctional may reduce the failure rate under severe operating conditions. The literature mentioned shows that steel is still the most frequently used tube material for all heat exchangers in power plants (Lazi´c et al., 2016) This is attributed to its easy claddability, excellent corrosion resistance, high strength, and low cost, even though these exceptional qualities are limited in severe operating conditions.

Saito et al. (2015) also showed the significance of nickel-based alloys as tube materials, which have high strength, excellent corrosion resistance at elevated temperatures, ability to join with different materials with dissimilar properties. However, it is prone to pitting and crevice corrosion in disposal environments due to the spontaneous layer developed in hostile environments. Moreover, it is clear that the high thermal conductivity of copper-based alloys makes them ideal for heat transfer

applications, and they are frequently combined with nickel-based alloys to produce cupronickels, which, along with ferritic steel, make up the mainstays of boilers.

2.5 Functionally Graded Coatings for Heat Exchanger Applications

A new type of multifunctional material called functionally graded materials (FGMs) can be used as surface modifiers to reduce the deterioration of heat exchanger parts (Hamatani et al., 2003). This is because their microstructure and compositional grading can be changed to achieve the desired function at a particular part location. FGMs are realized by linearly varying the composition and properties over a specified volume. Thus, grading of dissimilar materials has been a challenge for material researchers due to numerous requirements and a lack of clear understanding of the material's thermal, chemical, mechanical, metallurgical, and tribological properties, which have an impact on the microstructural-phase transformation during laser beam material interaction (Sathish et al., 2021). This section addresses the substrate and FGM interaction literature findings to clarify how material qualities affect the microstructural alteration of the FGM and how it affects performance characteristics including resistance to corrosion, wear-erosion, and oxidation.

Heat exchanger FGMs find applications in different process industries, as shown in Figure 2.9. The power production sector is one of the growing energy sectors that call for parts with outstanding material qualities that can survive harsh working conditions. However, high temperatures, abrasion from solid and marine particles, corrosion from chemical processes, and high pressures can cause wall thinning and eventual collapse in boiler tubes (Schwartz, 1982). As such, an individual alloy is limited in demanding applications, using FGMs with unique material properties.

Polat et al. (2002) asserted that the usage of FGMs is crucial because they lessen residual interfacial stresses and cracking that worsen the occurrence of disastrous failure consequences brought on by inadequate bond strength of coatings. According to the authors, FGMs are favourable because they lessen the thermal mismatch between the substrate and coating, which is affected by variables like thermal conductivity, coating thickness, bond strength, elastic modulus, and thermal expansion. El-Wazery & El-Desouky (2015) came to a similar conclusion when they

indicated that functionally graded coatings could be made from different materials, including ceramic-metal, and metal-metal, resulting in gradings with a less thermal mismatch at the interface. Therefore, FGMs are essential for preventing failures like stress-corrosion cracking, which is exacerbated by thermal strains in boiler tubes.

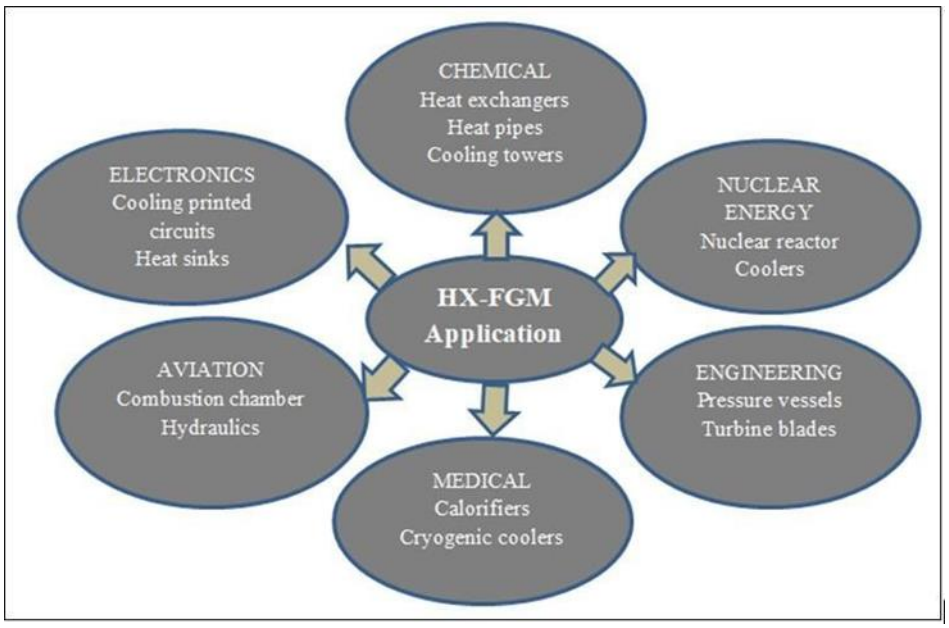

Figure 2.9: Potential Fields of FGM Application in the Heat Exchanger Industry

Due to the requirement for high-performance heat exchanger components, particularly those used in power generating industries, the use of FGMs made up of different materials including stainless steel and Inconel-based alloy combinations has drawn extensive study interest. As a result, there is a substantial amount of literature on FGMs developed with continuous material property discrepancy owing to their capacity to utilize both material properties and endure degradation as opposed to single alloy coatings materials.

For instance, the hot corrosion behavior of functionally graded Inconel 718/Haynes 25 that had a 75% Na2SO4 and 25% NaCl molten salt coating at 700 °C and 900

°C was examined by Luo et al. (2022). The FGM was made using the directed energy deposition method. The micrographs acquired demonstrated a microstructural change from coarse columnar dendrites in 100% Inconel to uniformly dispersed fine equiaxed

grains in 100% Haynes 25, as shown in Figure 2.10 (a-f). The homogeneous change of Inconel 718 is attributed to an increase in Haynes 25 content, resulting in a dense oxide layer that improves the material's resistance to hot corrosion due to the finer equiaxed grains produced by an increase in Cr content.

This may be because Haynes 25 is an alloy of cobalt, nickel, chromium, and tungsten. In general, it contains Cr, which tends to create passivation on surfaces during interaction with oxygen in the environment, leading to formation of a passive chromium oxide layer. The thin layer protects the surfaces from attack, being chemically reactive, and inhibiting corrosion-anticipated processes and corrosion product penetration through the material surface. This demonstrates that FGMs containing chromium can be used as heat exchanger coatings to improve another material's qualities resilience against degradation .

Ben-Artzy et al. (2021) also used directed energy deposition to combine disparate materials, including SS316L and C300 maraging steel, to create a grading. Because it is a cobalt-containing alloy with qualities strengthened by hardening intermetallic precipitates including molybdenum (Ni_3Mo Fe_7Mo_6), they chose C300 steel for its wear resistance and high strength. Since their goal was to create a graded material with good wear and corrosion resistance, SS316L's corrosion resistance made it suitable for grading. They noted that the graded coating lacked intermetallic, which they attribute to the creation of the $TiCr_2$ phase, which they stated that it reduced its occurrence.

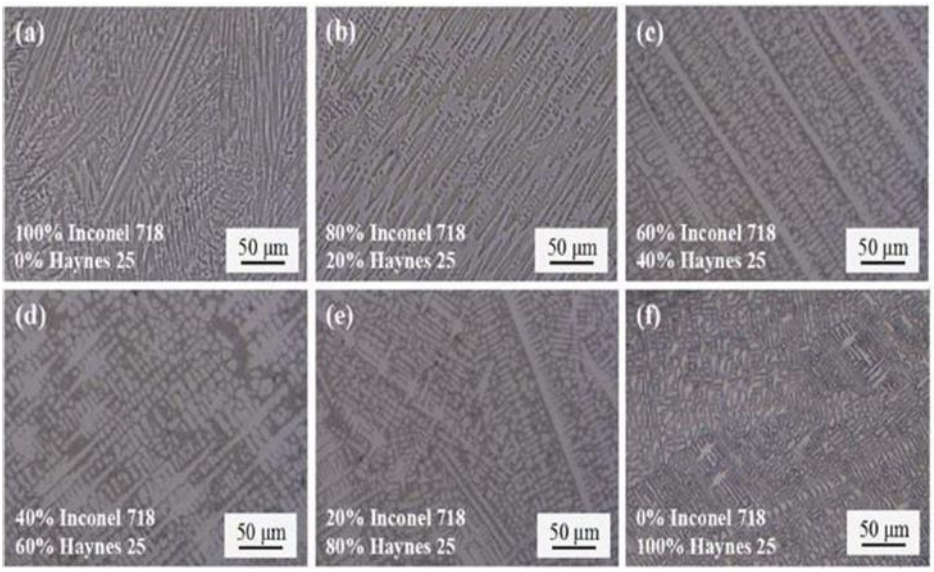

Figure 2.10: Variations in Microstructure with Increasing Content (a) Inconel 718 at 100% (b) Inconel 718 at 80% and 20% Haynes 40% Inconel 718 and 40% Haynes (d) 60% and Inconel 718 80% and Inconel 718 in Haynes (e) 205 100% Haynes (e) Haynes

Source: (Luo et al., 2022)

This grading could be regarded as successful because some intermetallics are undesirable when grading dissimilar materials because they can form intermetal- lic precipitation that makes heat exchanger coatings susceptible to localized corrosion, especially when the Cr and Mo alloying elements in SS316L get depleted in harsh environments.

Liang et al. (2010) developed two separate functionally graded SS316L and Inconel 718 using the laser-engineered net shaping (LENS) technique on the low- carbon steel substrate. The composition gradually transformed from a 100% layer of SS316L to a 100% layer of IN718. The microstructural evolution pattern rich in columnar dendritic growth occurred in their study in both the transverse and normal sections. They concluded that the solidification mode between the ferrite and austenitic structure during the columnar to cellular microstructural transition in the initial FGMs (FGM_1) led to decreased microhardness (0–50 v/o) between substrate and SS316L. However, the addition of Inconel 718 to the grading resulted in a considerable increase in the

microhardness of the second FGM due to the Cr and Mo elemental reinforcements that caused solid solution strengthening, as seen in Figure 2.11. Additionally, the wear resistance of FGM_2 was examined, and it was discovered to have outstanding wear resistance for 100% layers of both SS316L and In718. The inclusion of reinforcing materials like Cr and Mo content can greatly increase the hardness of FGM coatings, which is desirable for erosion-wear and corrosion resistance in heat exchanger boiler tubes

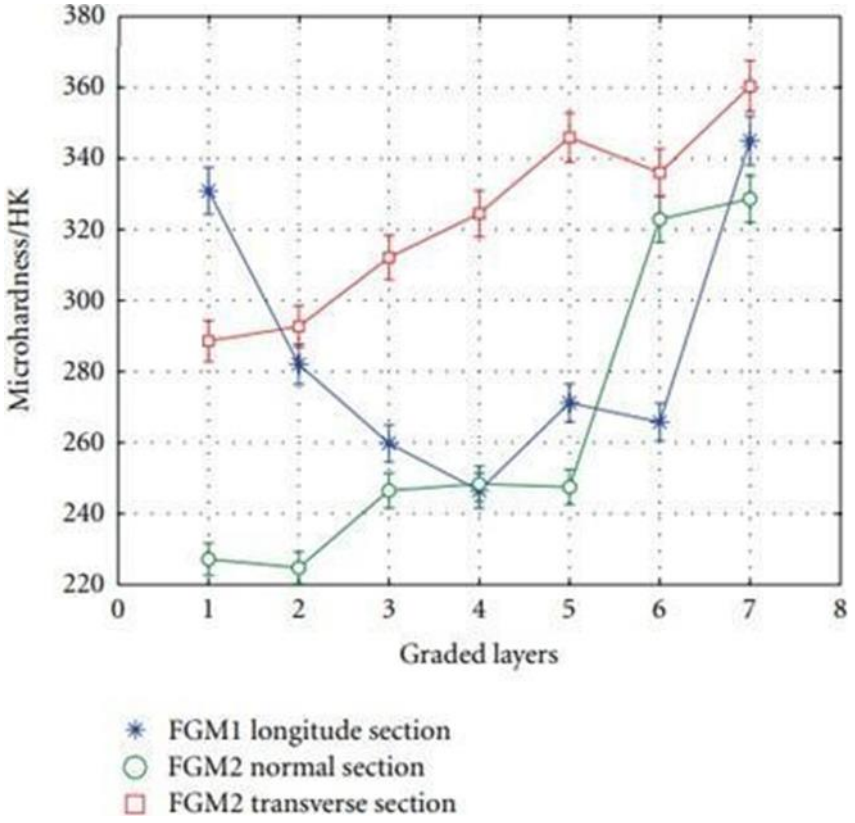

Figure 2.11: Microstructural Variation on Functionally Graded SS316L/In718

Source: (Wu et al., 2010)

Zhang et al. (2021) created a functionally graded SS316L/IN718/Cu material on an SS304L substrate by fusing disparate components with distinct material qualities together. SS316L was the first layer built up, then IN718, and ultimately pure copper. For parts exposed to challenging environmental conditions like elevated high pressure and corrosion, they developed the FGM, which combines the high thermal

conductivity of copper, the excellent high-temperature strength of SS316L, and the excellent high-temperature strength of IN718. The combined material qualities produced an outstanding interfacial bonding that resulted in a defect-free microstructure and a 125% increase in heat conductivity.

Figure 2.12 illustrates the good consolidation between the SS316L/IN718 contact that was seen when laser power was applied. The phase transformation in the SS316L layer, which had columnar dendrites initially in the vertical direction (Figure 2.12a) and converted to an equiaxed structure upon blending with In718 (Figure 2.12b), is of particular interest in their study. The technique can be further researched to improve the material qualities by figuring out the ideal parameters, which Zhang and co-investigators did not do in their study by varying the process parameters. Additionally, it is possible to use specific intermetallic materials, such as IN625, which are of importance to the heat exchanger tube sector, to take advantage of their resistance to degradations including pitting corrosion, erosion- wear, and stress-corrosion cracking.

Until recently, FGMs were created using traditional manufacturing processes (such as plasma spraying, powder metallurgy, and vapor deposition techniques). As a result, laser cladding has become a potential coating approach that gets around the drawbacks of traditional manufacturing processes. This is due to its ability to produce fully dense FGM coatings with minimal dilution and reduced thermal distortion (Reichardt et al., 2021). As a result, it may generate graded materials, such as exchanger tubing, that lessen the impact of corrosion and wear in harsh environmental conditions. On the other hand, the application of laser cladding has seen major downsides due to processing deformities, including cracking, porosity, and delamination, which are observed during the processing of FGMs. The literature is not clear on how the laser cladding technique and material parameters affect the laser beam interaction and microstructural/phase transformation performance features of heat exchangers. As a result, the section includes a thorough analysis of laser cladding of functionally graded coatings. The implications of process and material characteristics on the functional performance of FGMs for HX applications are explained via micrographs.

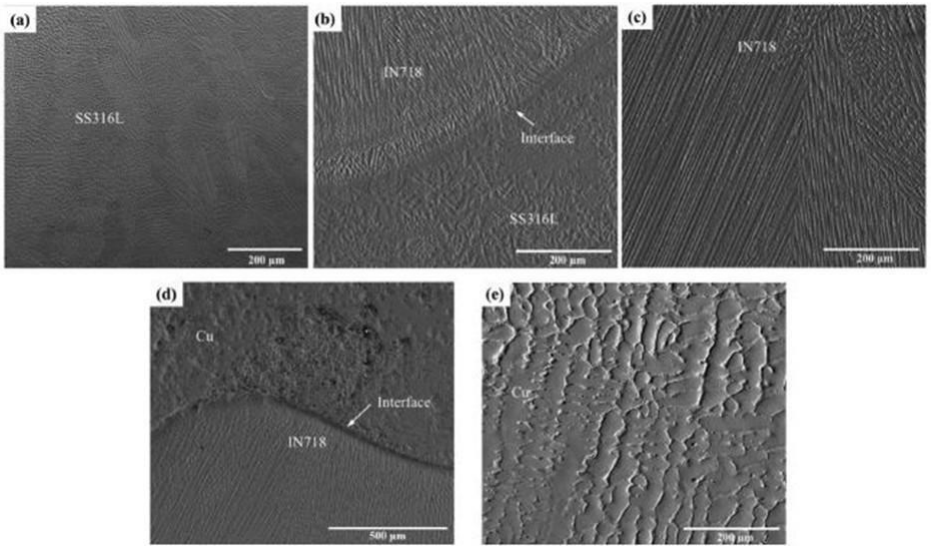

Figure 2.12: Microstructural Evolution of Laser Metal Deposited SS316L/IN718/Cu Functionally Graded Material (a) SS316L Columnar Dendrites (b) Good Bonding at the Interface (c) IN718 Equiaxed Structure

(c) good blending between Cu and IN718 (e) Transformed Cu microstructure (Zhang et al., 2021).

2.6 Laser Cladding Functionally Graded Materials for Heat Exchanger Pipe Coatings

Since the late 1990s, laser-based additive manufacturing (LBAM) techniques have been developed to increase component longevity through unique manufacturing procedures including laser cladding (LC). LC operates on a similar concept to laser metal deposition (LMD), directed laser fabrication (DLF), and laser-engineered net shaping (LENS). It melts metal powders with a laser beam and forms a thin film on a substrate material to generate consistent powder mixing. The laser beam causes the particles to melt, solidifying the molten substance in Figure 2.13. During this process, particles fuse and change the microstructure of the substrate material to create a coating. As a result, functionally graded coatings with fine-grained microstructures can solidify quickly.

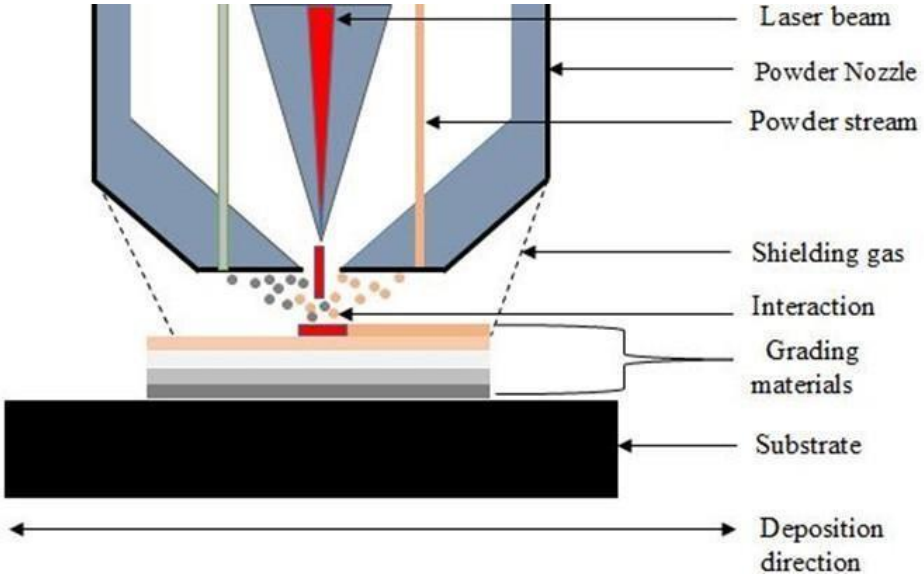

Figure 2.13: Interaction of the laser beam with FGM Powders during Laser Cladding

On the contrary, conventional manufacturing techniques previously used in fabricating heat exchanger parts (e.g. die-casting, milling, and folding techniques), have proven to be time-consuming, expensive, with limited geometries, and undesirable component weights (Klein et al., 2014). Such techniques can also cause poor metallurgical bonding, crack, and pore formation, as well as substrate distortion due to overheating during fabrication (Ferreira et al., 2021).

For instance, Saltzman et al. (2018), compared the performance of an oil heat exchanger cooler for aircraft fabricated with AlSi10Mg powder. They established that additively manufactured heat exchangers using powder bed fusion had a 10% increase in heat transfer and another 14% increase for the enhanced exchanger when compared to the one fabricated through traditional means. The reason is that AM provides avenues and opportunities for complex design configurations and optimized features having customized performance targets, which are challenging with conventional methods processes.

Laser cladding as an AM technique is a promising technique that finds application in process industries such as power generation and petrochemical plants due to its efficiency and ability to develop quality coatings with great process flexibility and

provide desirable economic benefits. For power plants, it is used to apply anti-corrosion and erosion-resistant coatings. As such, it can be adopted successfully in developing functionally graded material coatings for heat exchanger applications.

In this study, the laser-beam interaction with the functionally graded materials is elucidated for a clear understanding of the interaction effects to effectively enhance the fundamental microstructural features and quality of heat exchanger parts. Although a short interaction time is preferred during laser cladding, if the process parameters are not adequately regulated, it might result in processing deformities. Examples include a lack of bonding influenced by low heat input, porosity brought on by trapped inert gas, and cracking brought on by a significant temperature gradient between the substrate and the coating. Tensile residual stresses are also frequently produced during the LC process due to the highly concentrated energy input and quick manufacturing speeds. These stresses could hasten the failure of heat exchanger parts by spallation and cracking. They typically happen in the areas of tubes where stress corrosion cracking transitions from one state to another.

Nevertheless, it has been asserted that the manufacture of functionally graded materials using laser cladding reduces the residual stresses in the material caused by the interlayers responsible for expansions. The cumulative impact of residual stresses that are created in the material during fabrication can be reduced, according to this, using FGMs. The next part explains how a laser beam interacts with functionally graded materials to prevent microstructural deformation and material property changes (Roy et al., 2018; Updike et al., 1992; Zhang et al., 2021).

Elijah (2009) asserted that the heat generated during the laser cladding process results in melting and fluid flow, affecting the phases and grain structure of the microstructure, as well as dislocations and residual stresses, all of which have an impact on the quality of the parts that are produced. As shown in Figure 2.14, the Marangoni convention is a mass transfer fueled by surface tension, thermos- capillary forces, and elemental diffusion that can explain the convention effect. As the surface tension varies from low to high, this results in the creation of a shallow melt pool, which suggests that the deformation of the molten pool expands as the laser power increases. They also

demonstrated that if the movement of the heat source is not controlled, the velocity variation during a deposition could lead to unstable powder interactions with the substrate, which frequently results in processing defects like cracks or pores. Different melt-pool shapes were created due to the element's movement being prompted by surface tension forces, which are said to be directly related to temperature. According to Le & Lo (2019), the composition of the metal affects surface tensions.

This demonstrates that a larger concentration of an element existing in a material, such as sulfur, can increase surface tension and the melt pool because surface tensions regulate the flow pattern that forms in the melt pool. Equation 1 below, which is based on the dilution rate technique and assumes that the characteristics of the powder (Xpow) and substrate (Xsub) are linearly dependent on the thermal physical characteristics of the melt-pool (Xmix), can also be used to characterize the interaction between melted powders and substrate.

$$X_{\text{mix}} = \alpha X_{\text{sub}} + (1 - \alpha) X_{\text{pow}} \tag{2.1}$$

Where α is the mixture fraction governed by the dilution. The given literature makes clear that the copper substrate and IN625/SS316L laser material interaction have not been adequately explained. The experimental work tackled this mostly untapped area of needed research, which is why it was necessary. Moreover, a focus is on how the laser cladding process and material parameters affect the clad performance characteristics.

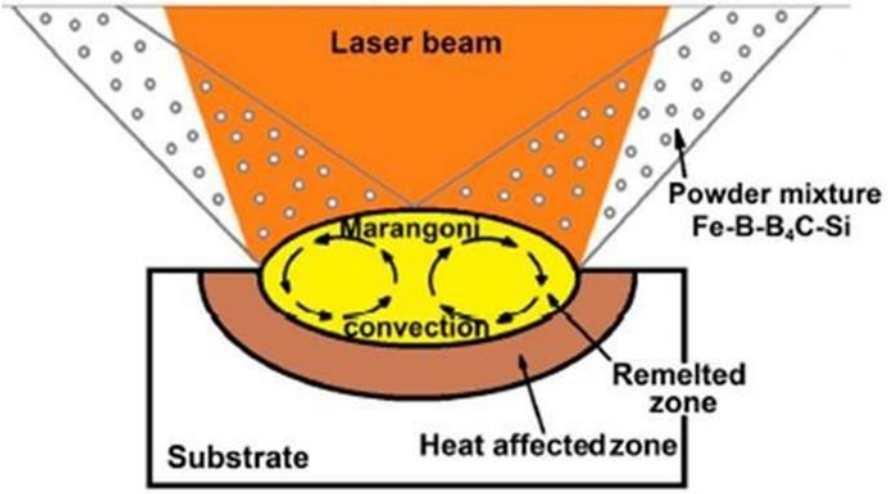

Figure 2.14: The Phenomenon of Marangoni Convection during Melting

Source: Bartkowski et al. 2020)

2.7 Laser Cladding Process Parameters

Control parameters during laser cladding have an impact on the microstructure and quality of functionally graded materials. The clad are divided into many categories since a variety of variables can affect their quality. The cause-and-effect diagram or fishbone diagram, which are other names of the Ishikawa diagram, is a well- known classification system.

As a result, Figure 2.15 uses the Ishikawa diagram to classify the factors influencing the clad quality during FGM production for heat exchanger surface modification. (Goodarzi et al., 2017) posited that the laser power, scanning speed, and powder flow rate have the most effects out of all the LC process factors.

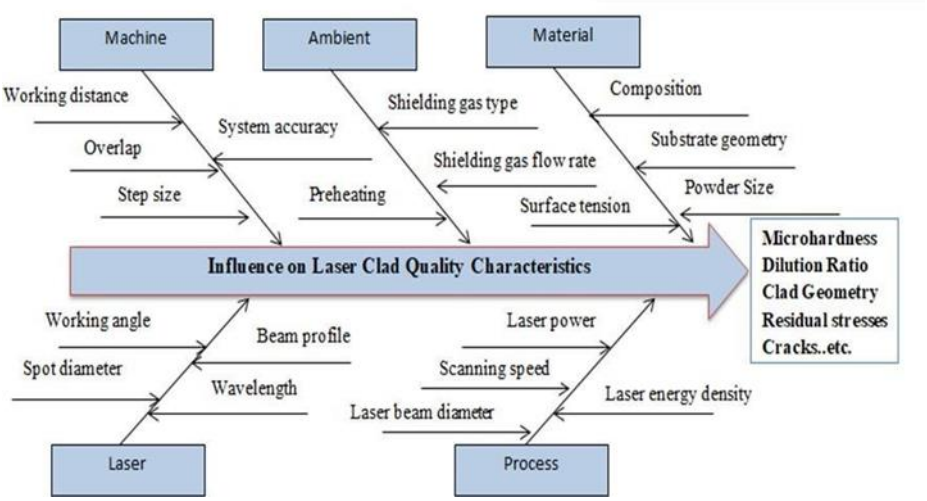

Figure 2.15: The Ishikawa Fish-Bone Diagram Illustrating the Influence of Laser Cladding Process Parameters on Cladding Quality Characteristics

This section combines and clarifies four crucial elements and their effects on the performance of heat exchanger parts utilizing research from the literature to address the poorly clad quality features generated owing to subpar manufacturing circumstances. This comprises (i) the laser energy density, (ii) the makeup and particle size distribution of the coating powders, (iii) the shield gas velocity, and (iv) the substrate preheating temperature. Since the laser energy density affects the melt pool and solidification mechanism, which determines the microstructural qualities that govern heat exchanger performance, it is chosen as the most crucial parameter. The type of powder composition and particle size distribution has an impact on how quickly melting and take place.

Shielding gas was chosen as another critical parameter since it can protect the material from the atmospheric reaction during LC processing because some inherent process faults, such as porosity, which impair FGM clads intended for boiler tube resistance to oxide penetration. Substrate preheating, which reduces thermal gradients that can inhibit fusion between boiler pipe surfaces and the layers of coating that is applied during surface modification, is another significant element that has been investigated. The most often observed failure mechanisms in heat exchangers are corrosion cracking, fatigue, and erosion, which are amplified by the inferior clad quality and

geometrical features. This refers to corrosion and wear, aspect ratio, and microhardness (Addepalli et al., 2015).

2.7.1 Laser Energy Density

According to equation 2.2, the laser energy density (LED), which is expressed in J/mm^2, has a directly proportional relationship to laser power (P) and an inverse relationship with speed (V) and beam diameter (d) (Olakanmi et al., 2019b). Simply put, the size of the molten pool, which affects the solidification process, the morphology of the grain structure, and the geometrical properties of the FGM clad, is determined by the energy dissipation rate as a function of time. Additionally, as the laser beam cannot dwell longer during deposition during fabrication, an increase in scanning speed will result in a smaller melt pool and a shorter duration of laser metal interaction, which will lower LED. The laser spot diameter, also known as the beam diameter, has a considerable impact on the sort of microstructure that is created. An increase in laser spot diameter will result in a reduction in the rapid cooling process caused by the energy density, which will also result in a drop in the melt pool temperature (Wei et al., 2020).

$$LED = P/(V.d) \tag{2.2}$$

Previous research has been done on the relationship between LED and wear characteristics. Undoubtedly, a smaller melt pool attributed to LED can lead to smaller, irregular grains, which often have more porosity and lower wear resistance (Watring et al., 2020). Additionally, a rise in LED's appropriate values can provide a desirable melt pool that, as a result of good microstructural development, increases the resistance of FGMs to wear and corrosion. The microstructure can develop pores and cracks if the LED is beyond a particular threshold because there may be an excessive melt pool that takes longer to solidify. Due to the ease with which oxide can penetrate the FGM clad, poor cladding quality can lead to heat exchanger pipes that display poor wear and corrosion properties (Siddiqui & Dubey, 2021).

As an illustration, Jing et al. (2021) created a functionally graded layer of HA-TiO_2 on a Ti6Al4V substrate via laser cladding while varying the LED between 20 J/mm^2 and

100 J/mm^2. The formation of pores was observed at LED of 20 J/mm^2, but as LED increased, they noticed a good consolidation mechanism that produced flat surfaces with strong bonds at LED of 60 J/mm^2, and smoother surfaces with no cracks or pores at LED of 70 J/mm^2, which is attributed to the uniform particle consolidation upon melting. Because corrosion resistance increases with decreasing surface roughness, this may also increase corrosion resistance. The creation of defects, such as thermal stress cracks, pores, and an uneven clad surface, increased as the LED's power was raised to 80 J/mm^2 and 90 J/mm^2, though, as illustrated in Figure 2.16. They asserted that the depletion of W, Ti, Co, and P caused by gasification, which resulted in increased tensile stress, was the cause of cracks in FGM clads.

Generally, strong bonds might also be a sign that the LED was perfectly positioned to produce a large enough melt pool to solidify with the substrate (Olakanmi et al., 2019b). A greater LED, on the other hand, resulted in an excessive melt pool that slowed down solidification and led to the formation of pores, which can impair the performance of heat exchanger parts under high-pressure loading and lead to stress corrosion cracking (Rebak, 2011). It was also discovered that corrosion resistance rose at 70 J/mm^2 with a lower corrosion rate of 0.062 mm.a-1, but fell at 90 J/mm^2 with a greater corrosion rate of 0.211 mm.a-1. This demonstrates how LED has an impact on the morphology and surface quality of graded coatings and how this has a major on wear and corrosion behavior, a crucial quality attribute required to increase the service life of heat exchanger parts operating in challenging conditions.

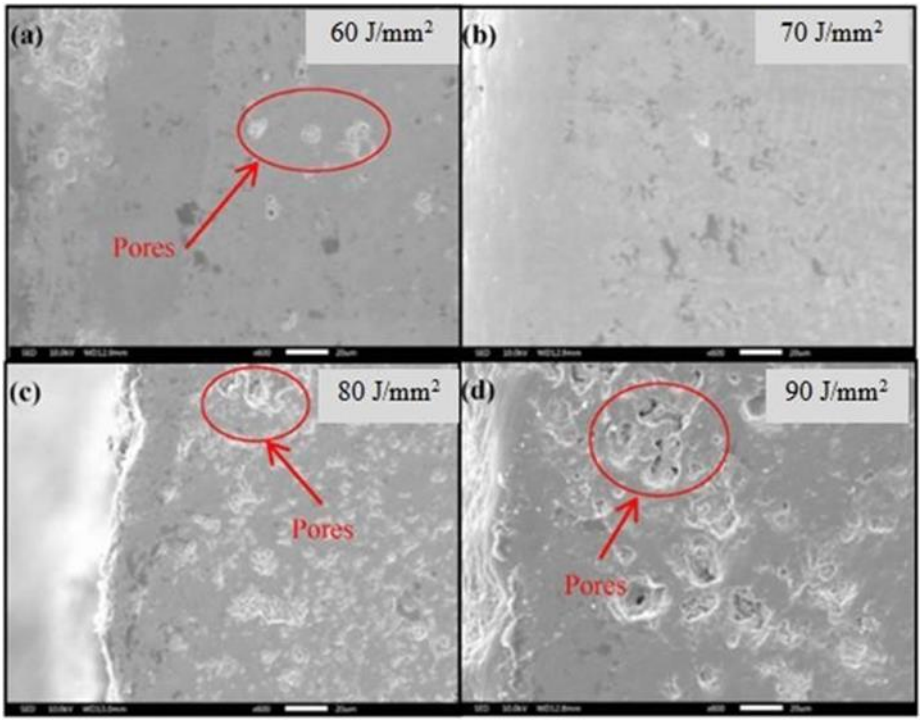

Figure 2.16: The Microstructure With Varying LED (a) Pore Defects at 60 J/mm2 (b) Optimum Structure without Defects (c,d) Large Pore Inclusions at 80 to 90 J/mm^2

As energy density rises, solid solutions, precipitated phases, grain refinement, and microstructural enhancement all often result in increased microhardness qualities (Cheng et al., 2018). Strong metallurgical linkages or structures are produced as a result of sufficient particle melting during high energy input, which increases the mechanical properties of heat exchanger coatings (Mahamood et al., 2013).

Higher LED increased dendritic structure, as was discovered by Shah et al. (2020) who developed Inconel 718 FGM and stainless steel 316L FGM. Fewer lave phases typically precipitate when LED rises, resulting in a dendritic structure that changes the microhardness characteristics. This suggests that employing the right LED parameters is crucial to achieving a suitable grain structure, higher deposition quality, and improved material performance. It may also be the result of undercooling, which alters the mechanical properties and promotes rapid dendritic development.

To increase corrosion and wear resistance qualities, Ocylok et al. (2010) used the laser cladding technique to create a layer of Stellite 31 and Marlok-graded material that was free of cracks. The authors noted a linear rise in hardness that varied between the transition layers. They claimed that the porosity level dropped as LED density increased, hence they attributed the improved microstruc- tural features to the conditions of LED processing. Olakanmi et al. (2019b) investigated how LED affected the microstructural characteristics, which in turn affected the microhardness characteristics. The titanium aluminide (Ti-Al) combined with TiC that was deposited on Ti6Al4Vsubstrate was made using three distinct amounts of laser energy density (12.50, 15.00, and 17.50 J/mm^2).

When the LED was set to 17.50 J/mm^2, they got a nice bond. As seen in Fig. 28 (g-i), optical micrographs of manufactured samples show that TiC particles melt well at energies of 12.50 and 15.00 J/mm^2, whereas aluminum melts poorly at these energies, which they attribute to a lack of energy input sufficient to start a metallurgical reaction. Intermetallic, such as the Ti2AlC, γ, and $\alpha 2$, was created as a result. The formation and intensity of the matrix phases were improved as the LED was increased.

According to cited literature, the same intermetallics contributed to the FGM-clad microhardness being higher than that of the Ti6Al4V substrate. Since the reaction was insufficient to generate intermetallics, the microhardness for the LED set at

12.50 and 15.00 J/mm^2 was reduced as a result. This demonstrates the necessity to eliminate process faults by optimizing the LED characteristics. According to (Mahamood and Akinlabi, 2015), the performance of optimized functionally graded Ti6Al4V/TiC was compared to that of similar materials made using fixed process parameters. They discovered that the microhardness and wear resistance were both greatly improved at the optimal LED parameters to 1200 HV, which was four times better than that of the substrate, demonstrating that improved parameters and clad quality resistance to wear can increase the microhardness. The aspect ratio and dilution of the FGM-clads are likewise affected by the LED. The aspect ratio in Eq. 3 can be calculated using the width and height of the clad track, while the dilution can be calculated using the deposit height and penetration depth (see Eq. 4).

$$\text{AspectRatio} = w/h \tag{2.3}$$

$$\text{Dilution} = D/(D + H) \tag{2.4}$$

Aspect ratio and dilution both rise with the LED density. This is due to the reason that higher energy densities lead to more melting, which promotes greater mixing between the base material and the FGM cladding material. In particular, the clad height reduces as the LED rises (Song et al., 2016). On the other hand, as the LED increases, so does the FGM clad width. This might be explained by the Marangoni convention phenomenon's melting force and flow viscous force, which results in the suppression of the deposited layer upon melting. As a result, the clad height is decreased, and the surface-level melt pool volume growth worsens the melted area, increasing the FGM clad width in this instance. Because the clad height is dependent on the quantity of FGM powders injected to form layers during deposition, it is obvious that it must be reduced when boiler tube surfaces are modified to increase cost- effectiveness and decrease clad weight. However, a wider clad is recommended because it enhances the coating's surface area and its ability to defend against various degrading attacks.

Grey Relational Analysis (GRA) with multiple responses was used by Lian et al., (2019) to maximize the flatness ratio and cladding efficiency. The ranges for the laser's output and scanning velocity were 1.2 to 1.5 kW and 5 to 8 mm/s, respectively. They contrasted the clad morphology of samples produced using the Taguchi L_{16} orthogonal experimental design's parameters and those produced using 1.5kW's optimal GRA values. Results demonstrated flaws in the clad morphology in non-optimized samples, as shown in Figure 2.17 (a,b), but when applying ideal parameters, as shown in Figure 2.17 (c,d), there was a reduction in flaws of partial fusion between the substrate and cladding layer. In addition, the method's tiny 0.97% prediction error demonstrated how using the best processing settings can improve the efficiency and geometry of the clad.

2.7.2 Composition and Powder Flow Rate

As the powders are altered during the cladding of FGMs, variations in the material composition can result in microstructural variation that can affect the mechanical properties of the clad. For instance, Ostolaza et al., (2021) looked at the clad quality traits

of functionally graded AISI 316L and AISI H13 generated by the DED process on AISI 1045 mild steel substrate as the material composition changed. As illustrated in Figure 2.18, after the first layer was initially deposited with 100% AISI 316L, the composition was altered at intervals of 20% until the top layer with 100% AISI H13.

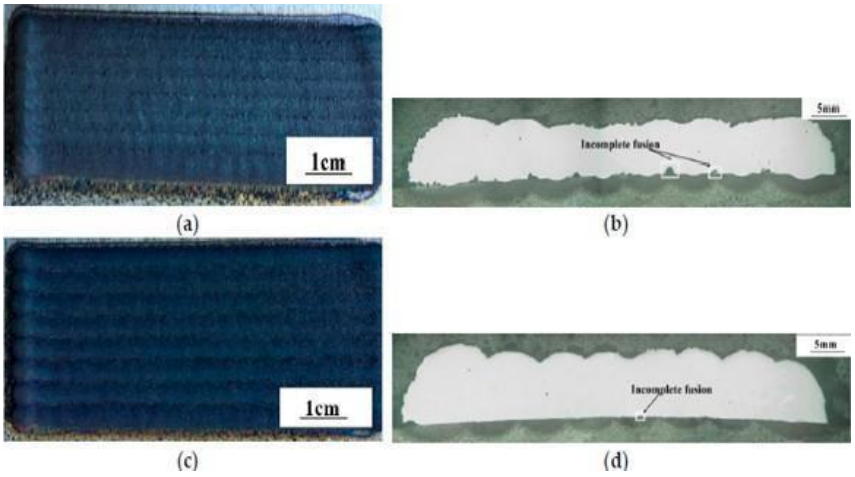

Figure 2.17: Comparison of Microstructural Bonding at the Interface for (a, b) Non-Optimized Deposition with Lack Of Fusion (c,d) Well-Optimized Deposition

Source: (Lian et al., 2019)

At the lower 316L layer, they noticed an austenitic with ferrite microstructure, and at the upper H13 layer, they noticed a progressive transition to martensite and austenite microstructure. They attributed the abrupt increase in micro-hardness from the lower to the higher layer caused by the addition of H13 powder to the rise in carbon content. As a result, the microhardness property was improved. This demonstrates that carbon content is a hardening ingredient that, when its quantity is raised during deposition, induces a significant increase in the microhardness of the FGM clad.

Carroll et al., (2016) concluded that, as shown in Figure 2.19, that compositional variation can affect the FGM microhardness qualities over the length of the gradient zone. Through a gradient zone, they used the DED method to deposit 20 layers of SS304L, followed by 19 layers of Inconel 625. Due to compositional and microstructural differences, cracks were seen in the area containing 79wt% SS304L and 21wt% IN625. They attributed crack initiation to the production of a secondary

phase with micron-sized particles rich in carbides with Nb and Mo content. This demonstrates how improper elemental powder composition can cause the production of defects that can impair the quality of the coated heat exchanger part by making it susceptible to weakening, hydrogen cracking, and embrittlement in different areas.

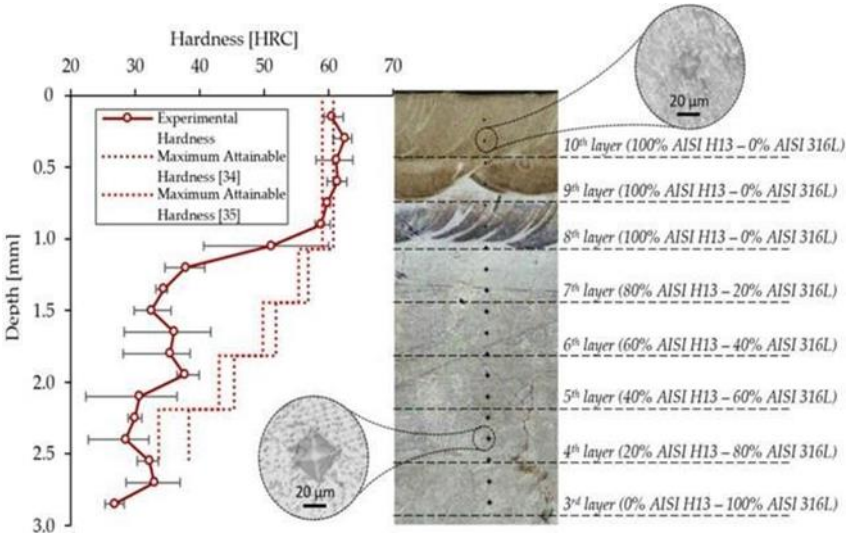

Figure 2.18: Increasing Microhardness Profile Concerning Composition Grading

Source: (Ostolaza et al., 2021)

The ”powder flow rate,” which is the rate at which the powder flows into the laser beam powder melting zone, also has a significant impact on the properties of the created FGM clads. To determine how the powder flow rate parameter impacts the properties of the FGM-clad surface, several studies have examined this issue. According to cited research, the quality of the surface finish improves when the powder flow rate is reduced during laser cladding. Accordingly, it is recommended that the powder flow rate be controlled, especially in the heat exchanger industry, to avoid secondary finishing procedures that might be costly. In addition, a higher powder flow rate causes the clad height and width to increase, which reduces the aspect ratio Mahamood & Akinlabi (2015). The clad shape can be explained by the excessive build- up that occurs when powder enters the matrix in bulk proportions, but the width decreases because so much energy per unit area is required to melt the amount of powder that is introduced to the matrix.

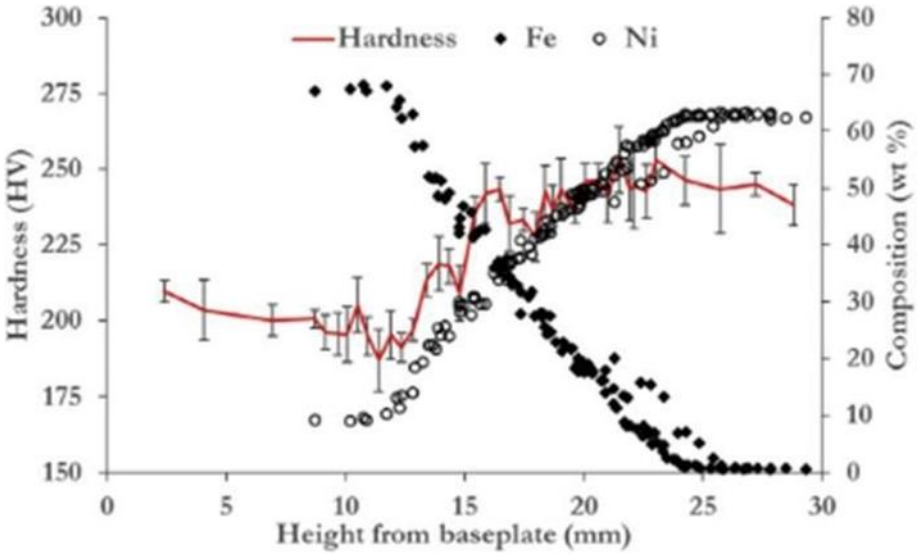

Figure 2.19: Microhardness Profile Variation with Increasing Elemental Content

Source: (Carroll et al., 2016)

It is obvious that the powder flow rate plays a significant role in determining the clad geometry, highlighting the need for optimization techniques to create trustworthy surface clads (Tiwari et al., 2020). For instance, Tiwari et al. (2020) employed the hybrid optimization technique, which combines the artificial neural network (ANN) and particle swarm optimization (PSO), to raise the aspect ratio quality attributes. The developed ANN-PSO model is suitable for forecasting and adjusting quality attributes during laser cladding because the simulation results and the actual outcomes were in agreement. It had an 8.68% mistake. A general ANN structure has an input, hidden, and output layer to connect the function between process parameters and output parameters/performance characteristics (Marrey et al., 2019), as shown in Figure 2.20.

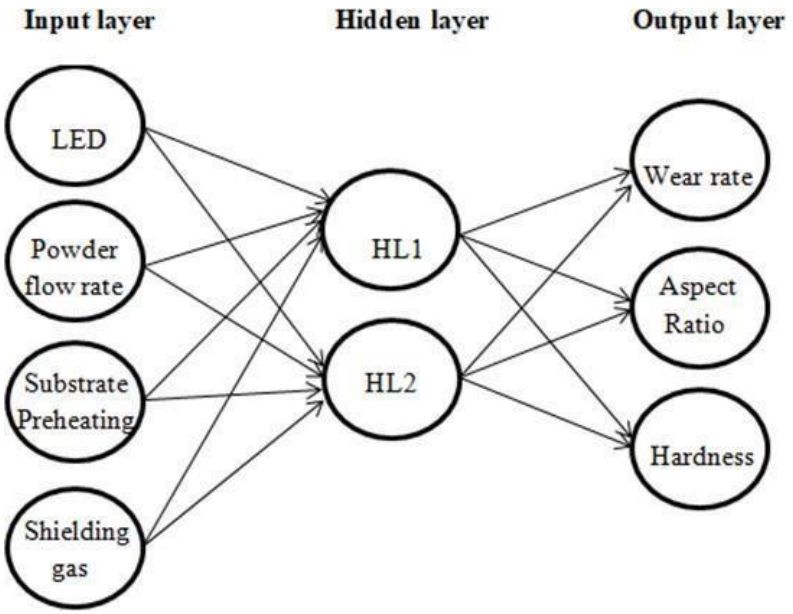

Figure 2.20: Input to Output Structure of the Artificial Neural Network

2.7.3 Substrate Preheating

Before laser irradiation of the produced FGM layer, the base material can be heated using a "substrate preheating" approach to minimize processing defects that occur during the manufacture of FGMs (Nyadongo et al., 2021). Substrate preheating can be utilized to reduce undesirable aspects like residual stress buildup and temperature mismatch between the substrate and the deposited layers. Significant temperature gradients form between the substrate and the FGM clads, and it is discovered that rapid cooling rates have an impact on fracture growth. Therefore, substrate preheating is a key factor in preventing the early failure of boiler pipes in difficult operating conditions by lowering internal tensions and cooling rates. This is true because an increase in temperature reduces the buildup of residual stresses, which reduces the risk of cracking Jendrzejewski et al. (2008).

Studies have been carried out to ascertain the impacts of substrate preheating during the fabrication of FGM and its impact on the clad quality characteristics, such as corrosion and wear behavior, aspect ratio, and microhardness qualities

Meng et al. (2020). For instance, residual stresses and the temperature gradient were reduced by Meng et al.'s 5-minute synchronous preheating of functionally graded

316L/Inconel 625 generated by LMD. The changing temperature differential in the molten pool affected the grain shape through a microstructural change from columnar to equiaxed structure. They also showed that the temperature gradient decreased as the FGM deposit layers expanded. Nb and Mo eutectic segregated along grain boundaries during non-preheated deposition, which caused solidification fractures in the centre (See Figure 2.21). When grading Inconel 625 to Ti6Al4V, Meng et al., (2020) also noticed crack development in the transition zone for the non-preheated samples. They explained that once Cr- and Mo-enriched phases formed, cracking was reduced in samples that had been warmed simultaneously.

This shows how preheating impacts the phase development and solidification of FGM layers. Strong interface adhesion can also be developed as a result, which helps to reduce processing faults such as fracture formation and residual stresses. This is due to the possibility that temperature mismatch and laser beam reflection can make clads prone to poorly clad quality features that reduce performance in challenging operating conditions (Zhang et al., 2008). Thus, it is reasonable to conclude that as the preheating temperature increases, the likelihood of crack propagation reduces.

Meng et al. (2020) also observed crack growth in the transition zone for the non-preheated samples while grading Inconel 625 to Ti6Al4V. They indicsated that cracking was diminished in samples heated simultaneously once Cr- and Mo- enriched phases had developed. This demonstrates the effects of preheating on the phase development and layer solidification of FGM. As a result, it is also possible to produce strong interface adhesion, which aids in lowering processing flaws such as fracture development and residual stresses.

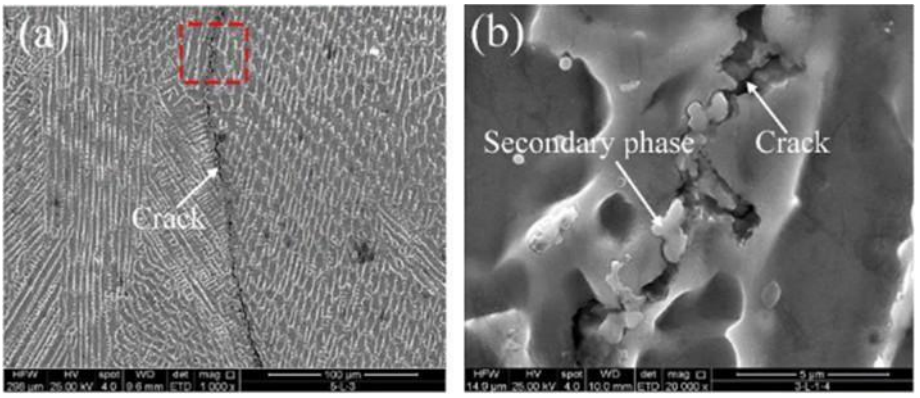

Figure 2.21: Microstructure Characterized By (a) Cracks at the Interface (b) Secondary Phase and Inclusions

Source: (Meng et al., 2020)

This is because temperature mismatch and laser beam reflection may render clads more susceptible to subpar clad characteristics that will lower performance under demanding operating conditions. As a result, it's reasonable sense to draw the conclusion that as preheating temperature increases, the likelihood of fracture development decreases. When building TA15-Inconel718 FGM, Shang et al. (2020) showed that preheating can assist avoid fracture formation. When they compared samples that had been preheated to samples that had not been preheated, they found that preheating at 500 °C prevented cracks from forming.

Internal stresses were also reduced as a result, and they found that the tensile strength of these internal stresses was 207 MPa, which was below the yield strength. It demonstrates that preheating can improve tensile strength, which improves microhardness properties because yield strength and tensile strength usually correspond with microhardness properties. The non-preheated FGM, on the other hand, showed cracks in the area between 80% and 100% of the Inconel 718 layer (see Figure 2.22), highlighting the importance of substrate preheating in the prevention of defects can affect the performance of coated boiler pipes.

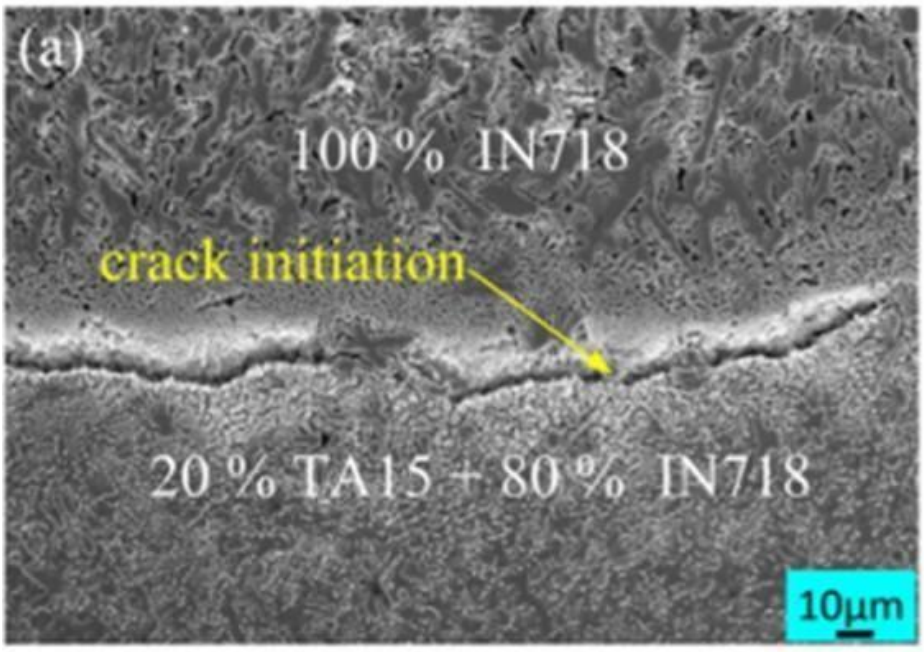

Figure 2.22: Crack Propagation at the Interface of Functionally Graded Material

Source: (Shang et al., 2020)

Preheating can be utilized as a process optimization approach to lessen substrate warping and distortion since an increase in preheating temperature increases total accumulated substrate distortion as a result of thermal contractions (Corbin et al., 2018) The temperature difference in the substrates probably is the reason because during laser cladding, the top of the surface is often hotter than the bottom. This implies that substrate distortion is reduced by preheating for thin substrates but increased for thick substrates. Additionally, the rate of deposition rises with increasing preheating temperature. This illustrates how the clad height increases as the preheating temperature increases. However, more research is required on how substrate preheating affects aspect ratio, wear, and corrosion quality parameters. Ac- cording to research, pipes operating in difficult environments can have their surfaces modified before being preheated to increase wear and corrosion resistance.

For instance, Liu et al. (2022) successfully warmed copper alloy and deposited a Ni60-WC cladding coating with no flaws. The (Fe, Ni), M_7C_3, and WC reinforcement phases were able to form as a result, improving the copper substrate's wear resistance as the

wear rate was 910-5$mm^3N^{-1}m^{-1}$ and accounted for 1.14% of the substrate material. With a corrosion current density that was better than the substrate's, $2.3410^{-7}mAmm^{-2}$, higher corrosion resistance was also attained. This shows how preheating can promote the creation of reinforcing phases, which is what gives the material enhanced wear and corrosion resistance.

2.7.4 Shielding Gas Type and Velocity

To stop the deposition from oxidizing as a result of interaction with ambient gases, shielding gas, measured in L/min, creates an inert gas environment. Argon gas is the shielding gas that is most frequently used in laser cladding. Shielding gas is an important characteristic because the presence of hazardous gases can cause the oxidation of cladding, which reduces the cladding's quality and resistance to degrading attacks in heat exchangers (Li et al., 2020). The authors deposited bulk components of four clad with different external shielding gas rates, designated Q1 (14 L/min), Q2 (18 L/min), Q3 (30 L/min), and Q4 (50 L/min). They noticed that at lower shielding gas values of Q1, oxidation caused bluish discoloration, which turned yellowish in Q2 and silver in Q3 and Q4, as shown in Figure 2.23.

It is clear that oxidation damages the clads surface integrity, making galvanic corrosion a threat to FGM clads intended for boiler pipe surface modification. Additionally, due to the strong reactivity at lower shielding gas values, inclusions, and oxide development in the microstructure are possible. For instance, when steels react with oxygen, oxides rich in Si and Mn may be introduced, which affects the stress corrosion cracking behavior (Saboori et al., 2020).

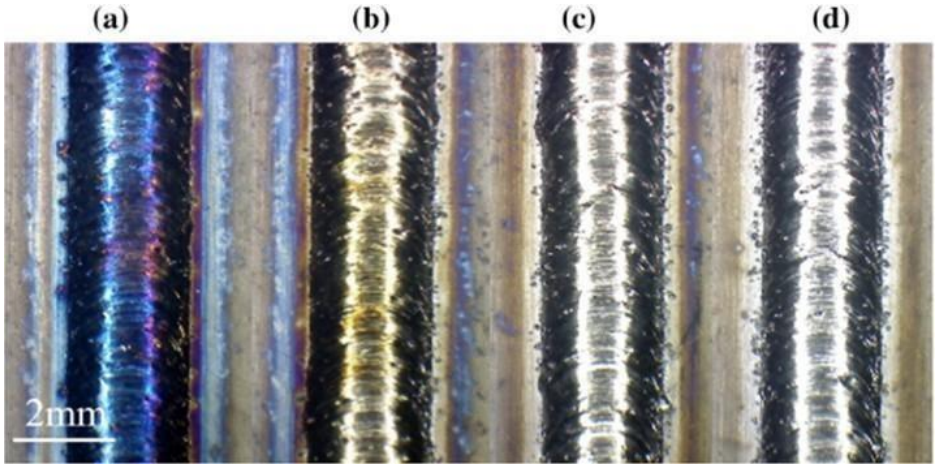

Figure 2.23: TMicrostructure with varying LED (a) Pore Defects at 60 J/mm^2 (b) Optimum Structure without Defects (c,d) Large Pore Inclusions at 80 to 90 J/mm^2

This is because the microstructure's intergranular Si-rich oxides reduce the material's ability to resist corrosion, which causes the deterioration of heat exchanger parts. This demonstrates the need for the melt pool to be shielded with oxides to reduce atmospheric reactivity because doing so can enhance the amount of oxide on the FGM clad. The mechanical properties of laser-clad FGM are also impacted by the shielding gas since it is connected to one of the most fundamental porosity problems. The phases decarburize when the atmospheric reaction is stopped, which increases their microhardness characteristics while decreasing the porosity. Because of this, the microhardness of clads rises as shielding gas velocity does (Singh et al., 2019).

2.8 Summary of Literature

The failure mechanisms encountered in heat exchangers have been presented. Pitting, chemical-induced, stress-corrosion cracking, erosion-wear, inter-granular, and galvanic forms of corrosion have been identified as the most prevalent in heat exchanger components, worsened by poor material selection. Several coatings have been developed to reduce the prevalence of failure in heat exchanger pipes. However, mitigation of stress-corrosion cracking of heat ex- changer tubes has proven inadequate, and graded coatings have not been utilized before. Surveyed literature has revealed that the failure emanates when protective oxides are eroded or penetrated by degrading agents (chlorides, sulfates, ammonia), due to poor processing conditions

leading to the formation of defects such as pores and cracks. Optimization of laser cladding process parameters via statistical and machine learning tools has also been shown through cited literature to be an emerging area of research that can enhance the properties, performance, and quality characteristics of fabricated functionally graded coatings.

Meanwhile, research on the optimization of Cu-based FGMs has not been explored using hybrid optimization techniques including Taguchi-GRA and ANN. Substrate preheating can enhance the mi- crostructural properties and reduce crack formation that lowers clad quality. The literature is still unclear regarding the influence of substrate preheating and shielding gas on the FGM-clad aspect ratio because there haven't been many experiments conducted in this area. This is an area of study that must be explored to improve the quality characteristics of FGM.

Therefore, this study developed a novel approach of depositing In625/SS316L FGM on a copper substrate, as well as optimizing the laser cladding process parameters using Taguchi-GRA and correlation of input to output parameters using the ANN QA method. Table 2.3 summarizes previous work carried out of HX, LC, FGMs, and optimization.

Table 2.1: Summary of Gaps Identified in the Literature

Author	Research Interest	Findings	Gaps	Present study
(Faes et al., 2019)	Factors attributed to the failure of heat exchangers	Corrosion Erosion Pitting Fatigue Fatigue	Quantifying and elucidating how erosion wear cause Hydrogen sulfide to penetrate The microstructural defects to cause degradation	Failure analysis conducted and the mechanism of degradation elucidated using
(Solke et al., 2021)	Suitable materials for fabricating heat exchanger pipes	Metals includes; Inconel, Copper, and steel esp. AISI 316L	Joining of copper and stainless steel dissimilar materials scarce.	To join pure copper and stainless steel 316L dissimilar materials.
(Chen et al., 2020)	Functionally graded materials developed for surface modification At extreme temperatures	Laser cladding is suitable for fabricating FGMs.	Laser cladding of SS316L/IN625 on pure copper substrate not explored	This study will developed a graded SS316L/IN625 on a pure copper substrate.
(Maodzeka et al., 2023)	Optimization of quality characteristics of coatings using Taguchi and ANN	ANN is effective In optimized laser Deposited materials.	Hybrid optimization of In625/SS316L unexplored using Taguchi GRA and ANN techniques.	Taguchi GRA and ANN utilized in optimizing quality characteristics (MH, AR, SR, and P)

CHAPTER THREE

RESEARCH METHODOLOGY

3.1 Chapter Overview

This chapter presents the procedure for failure analysis of the failed shell and tube heat exchanger. The experimental steps employed to fabricate the In625/SS316L functionally graded materials using the laser cladding technique are detailed. In addition, the method for sample preparation and the types of equipment used for microstructural analysis, phase analysis, and mechanical tests are described. The final section elucidates the hybrid optimization techniques that combine the Taguchi-GRA and ANN methods.

3.2 Heat Exchanger Failure Analysis Procedure

Visual inspection, chemical analysis, microstructural examination, and mechanical tests were all used in the experimental technique to determine the cause of tube failure.

3.2.1 Visual Inspection of the Tube Samples

Two heat exchanger tubes were extracted from the exchanger and tested for functionality. As illustrated in Figure 3.1, the first tube was determined to be the intact tube and served as the control tube (sample T1). The second tube was determined to be the ruptured/failed tube (sample T2). To find failure features that can be seen with the naked eye, the failed heat exchanger tubes underwent visual inspection. Moreover, pressure was blown through the tubes, and the leakage sound was used to distinguish between functional and ruptured tubes.

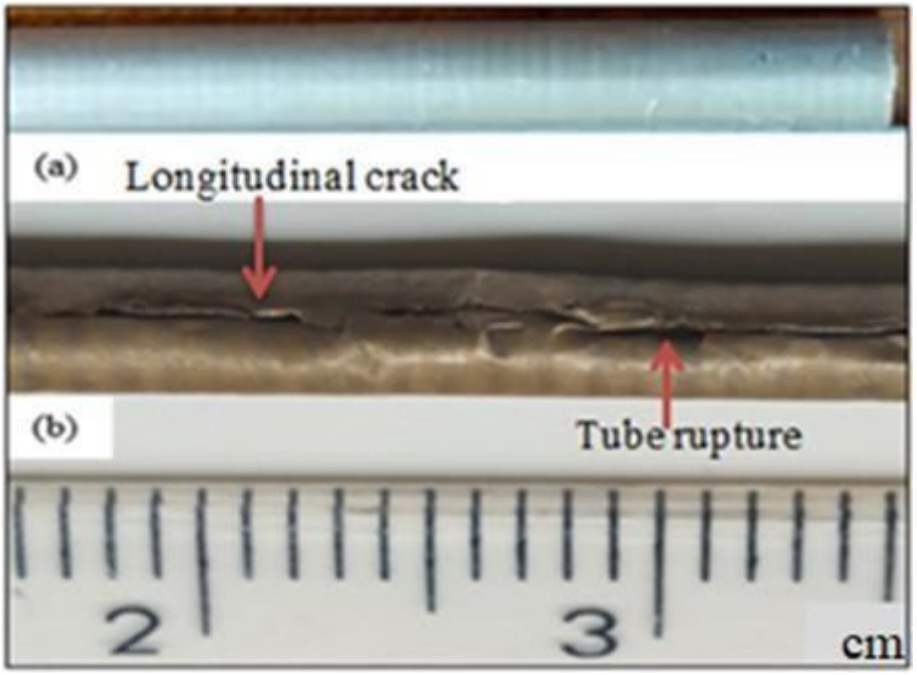

Figure 3.1: Sample Heat Exchanger Tubes Investigated for Failure (a) Intact Tube, Sample T1 (b) Failed Tube, Sample T2.

3.2.2 Chemical Analysis of the Water

Using a UV spectrophotometer (Shimadzu Cooperation, Japan), the chemical composition of the condensate utilised for cooling in the heat exchanger chambers and the corroded water collected from the failed heat exchanger tubes was examined for compounds. The cloudiness of the water was measured using a turbidity meter for the Nephelometric Turbidity unit (NTU) test. Additionally, the total dissolved solids (TDS) were measured using the oven drying method, and the metallic ions were measured using the Flame emission spectrophotometer (FES) and Atomic absorption spectroscopy (AAS) techniques. While the corroded and condensate water sulphides were analysed using the iodometric method, the hydrogen sulphite in the geothermal environment was studied using lead acetate test paper.

3.2.3 Microstructural Investigation of the Failure Samples

3.2.3.1 Sample Preparation

Using a Struers Labotom-15 cutting machine, sample T1 and T2 heat exchanger tubes were divided along the cross-section. The third sample was circumferentially sectioned for analysis to observe the internal corrosion products in the failing tube. By employing a mounting press and abrasive grit of sizes 320, 500, and 1200, samples were mounted on polymer resin. The samples were then polished to a mirror shine using MD Largo cloth and 9 m diamond suspension. The sample was gold-plated to ensure surface conductivity for SEM investigation.

3.2.3.2 Optical Microscopic Observation of Samples

An Olympus optical microscope was used for analysis to discover the internal abnormalities in samples T1 and T2. This includes examining the surface fractures and pits to identify the main cause of failure.

3.2.3.3 Scanning Electron Microscope of Samples (Including EDS)

JSM-7100F scanning electron microscope configured with energy-dispersive spectroscopy (SEM-EDS) was used to discover failure features at greater magnification. The main goals were to locate the point of failure, track the growth of the crack, and quantify the assortment of defects (cracks, pits, and inclusions) that were present. The oxides and elements in the corrosion residues were identified using a Horiba XGT-9000 X-ray Fluorescence analyzer (Kyoto, Japan). SEM-EDS was also used to validate the outcomes.

Table 3.1: Summary of the Sample Information and the Measuring Conditions

Description	**Value**
Sample distance(Monitor)	51.00 mm
X-ray tube voltage	30.00 kV
Tilt angle	35.0 deg
Peak analysis method	**Fitting Lorentz**
Total measurement count	50
X-ray irradiation time(Max)	50 sec

3.2.4 Residual Stress Measurements

Residual stresses were measured using the -X360s Portable X-ray Residual Stress Analyzer (Pulstec Ltd, Japan). Table 3.1 provides a summary of the parameters selected for the residual stress measurements. The residual stresses for samples T1 and T2 were measured. The final stresses were measured at the tube surface in the circumferential direction (see Figure 3.2).

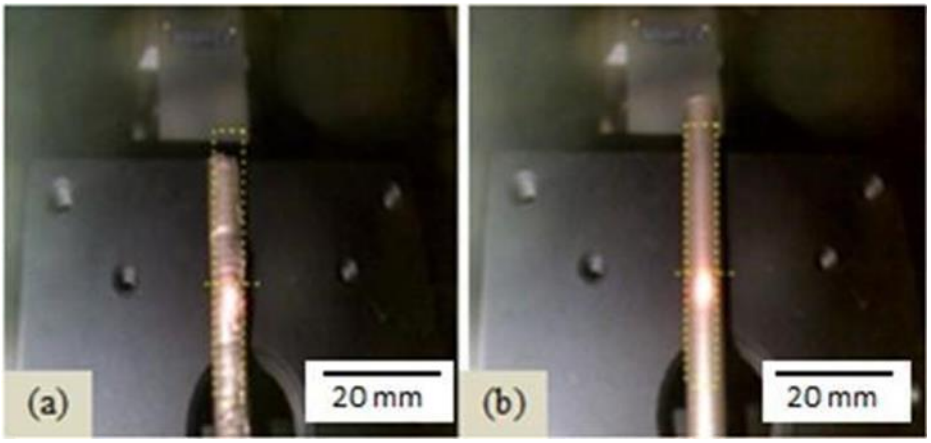

Figure 3.2: Sample Positioning for Residual Stress Measurements (a) Failed Tube and (b) Intact Tube

Table 3.2: Chemical Composition of the SS316L and IN625 Materials (wt-%)

Materials	Fe	Cr	Ni	Cu	Nb	Mn	Si	P	S	C	Al	Ti
SS316L	Bal.	17.17	10.57	-	-	1.05	0.64	0.005	0.003	0.01	-	-
IN625	1.96	21.80	Bal.	-	4.10	0.01	0.04	0.01	0.003	0.078	0.22	0.17
Cu	-	-	-	100.0	-	-	-	-	-	-	-	-

3.3 Fabrication of FGM Samples Using Laser Cladding

3.3.1 Materials and Methods

The functionally graded material was created using powdered SS316L (+45 - 90 m) and IN625 (+45 - 90 m), which were placed on a 100 x 50 x 10 mm pure copper substrate. South African company Avimetal AM Tech (PTY) LTD provided the materials. The powder particle morphologies are depicted in Figure 3.3 and have a

satellite-like, almost spherical morphology. Due to its uniform surface, this spherical powder shape can considerably improve the surface finish and powder deposition efficiency. The chemical makeup of the powder was confirmed and is shown in Table 3.2.

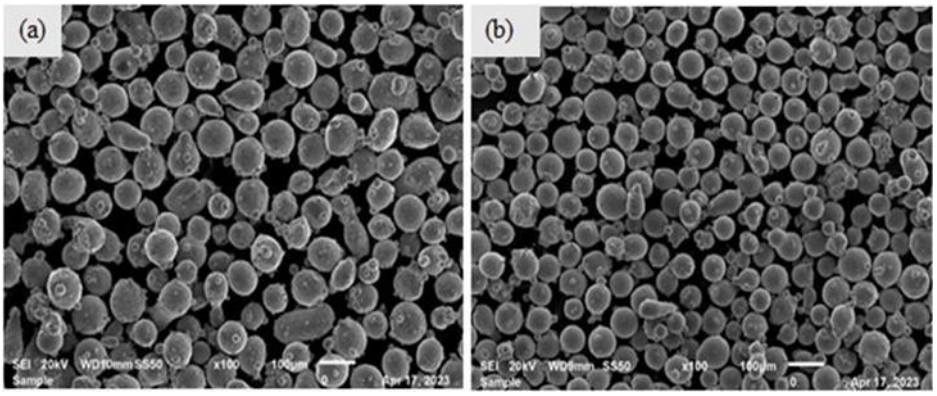

Figure 3.3: SEM Powder Morphology of (a) Stainless Steel 316L (b) Inconel 625

3.3.2 Laser Cladding Process

Figure 3.4 shows the laser cladding machine at the Council of Scientific and Industrial Research (CSIR), Pretoria in South Africa (SA). It consists of a 5kW IPG YLS fiber laser system with a Kuka robot connected to a 2-feeder hopper system, which injects powders through a coaxial nozzle with an argon carrier gas and shielding gas to prevent material oxidation. The argon gas and shielding gas were kept constant during deposition at 18 l/min and 8 l/min, respectively. The laser beam had a 2 mm spot diameter and the standoff distance was kept constant at a 10 mm distance above the substrate with a 60 tilt angle to overcome the high reflectivity of copper during deposition. Prior to deposition, the substrates were all cleaned with acetone to remove impurities from the surface.

To achieve a strong metallurgical bond, the initial layers were deposited using 1800W, 600mm/min, and 2 g/min. Since no research has been done to explore the laser cladding of functionally graded SS316L/IN625 on a pure copper substrate, initial parameters were determined using preliminary experiments with laser powers of 2700 W, 2400 W, 2100 W, and 1800 W. All laser values between 2700 W and 2100 W, except for the 1800W parameter, caused delamination, hence this value was selected as the

appropriate parameter. Due to copper's high reflectivity, which necessitates a greater energy input to form a metallurgical bond between copper and SS316L, a higher laser energy input was initially used. The Taguchi approach was used to fabricate the remaining layers.

Before continuous deposition, experimental design used Taguchi L9 (33) orthogonal array (OA). For each of the nine levels, the laser cladding experiments were carried out three times and given the labels TR1, TR2, and TR3. The laser power output ranged from 700 to 1000 W, the scanning speed from 400 to 600 mm/min, and the powder flow rate from 2 to 6 g/min. The matrix is extensively detailed in Table 3.3. By measuring the flow rate of the powder for two minutes and averaging the results of three comparable trials,

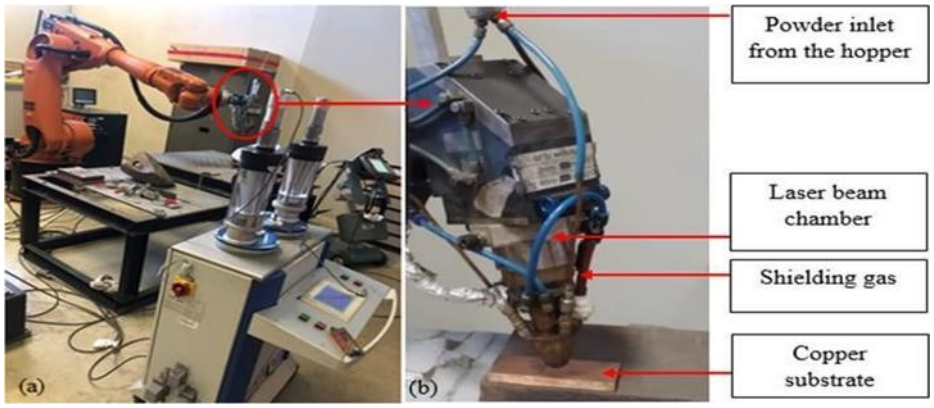

Figure 3.4: Laser Cladding System (a) Kuka Robot with a 5kW IPG YLS 5000 Fiber Laser System (b) Coaxial Nozzle

Table 3.3: Taguchi L9 Orthogonal Array for Fabricating SS316L/IN625 FGM

Run		Scanning speed,	Powder feed rate,
	W	mm/min	g/min
1	700	400	2
2	700	500	4
3	700	600	6
4	850	400	4
5	850	500	6
6	850	600	2
7	1000	400	6
8	1000	500	2
9	1000	600	4

A linear flowability graph with values in revolutions per minute (rpm) was created. The laser-clad layer thickness was maintained at 0.8 mm and a laser track overlap of 50% was also used.

3.5 Sample Preparation and Characterization

The Struers Labotom-15 cutting machine was used to section the fabricated samples along the transverse section for mounting, grounding, polishing, microstructural characterization, and mechanical testing.

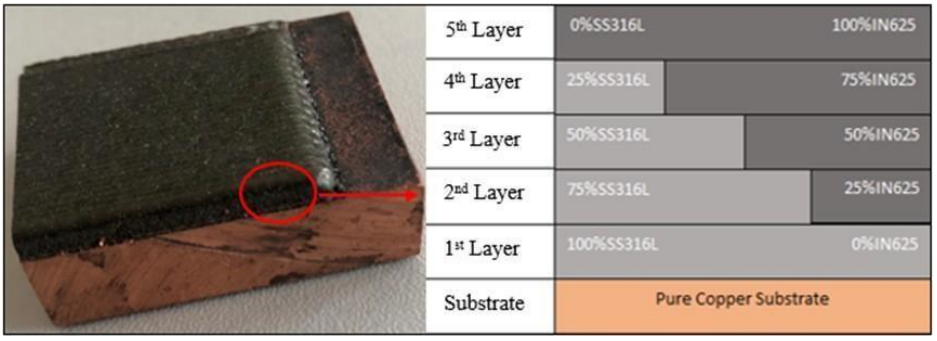

Figure 3.5: FGM Layer Build-Up (a) As-Built SS316L/IN625 clad (b) Compositional Variation (wt.%)

Hot mounting the cross-sectioned component in epoxy resin and grinding it with abrasive sheets of 120, 320, 800, 1200, and 4000 grit were both used. OP-S suspension, 9, 6, and 3 microns were used for polishing. A 50/50 solution of oxalic acid and water was then used to electrochemically etch the samples for 5 seconds. An optical

microscope (Olympus BX51M) was used to measure the clad geometry. The aspect ratio (W/H) was computed using measurements of the clad weight and height, as illustrated in Figure 3.4.

The porosity level of the FGM samples was also evaluated and measured using optical microscopy images and ImageJ software. Micrographs were changed to binary black and white to automate computations depending on contrast level. The microstructure and elemental composition were investigated using a scanning electron microscope with an energy-dispersive spectrometer (SEM-EDS). The microhardness was measured using a Struers Vickers microhardness tester (Leitz, Germany) with a force of 10 N for 10.0s. With 0.5 mm between the clad top across the build direction and the substrate, it was possible to make consecutive indentations with 1000 m spacing along the Y direction and 430 m spacing along the X direction. The average was calculated using the three created samples for each parameter, each of which contained 13 indentations.

3.6 Analysis of Data

The Taguchi L9 array was created using the Minitab statistical software (version 21.1.0) for the design of experiments and the Taguchi-based GRA analy- sis. The LMBP algorithm was utilised for ANN optimisation using the R2023a Matlab programme. The process parameters were used as inputs, and the grey relational grade as output to obtain optimum parameters. After op- timisation, a one-factor- at-a-time confirmatory test was conducted, and the samples were made using laser cladding while using the ANN optimum pa- rameters. Microstructural analysis was used to characterise the ANN optimal samples and confirm the influence of process factors on clad quality characteristics. The residual stresses for the optimal sample were measured using the Cu x-ray tube at 45 C inclination angle and 30 sec irradiation time on the Pulstec residual stress analysing equipment (Tokyo, Japan). This was done to determine if tensile residual stresses exist in the optimum sample. Thereafter, heat treatment was performed at 1050 °C for 2 hours following water quenching for the optimum sample, to increase the microhardness that can mitigate stress cracking in boiler pipes (Rodrigues et al., 2022).

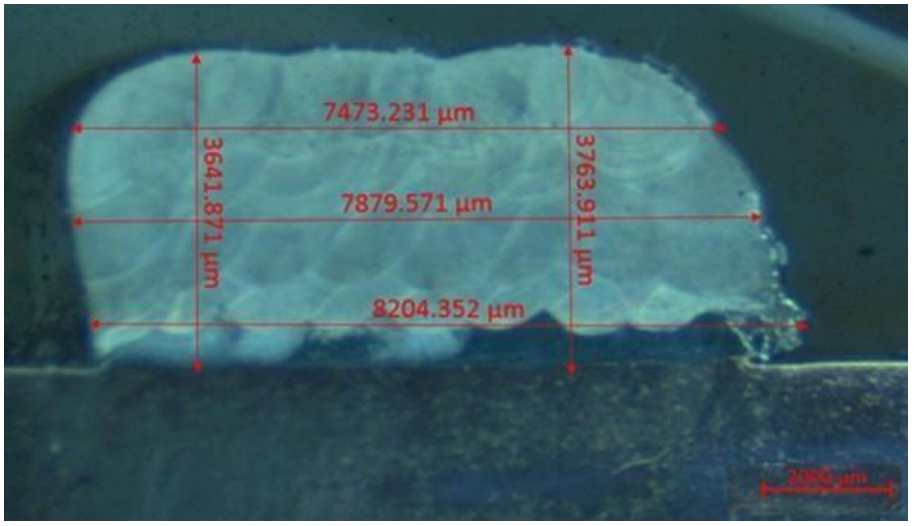

Figure 3.6: SEM Powder Morphology of (a) Stainless Steel 316L (b) Inconel 625.

CHAPTER FOUR

RESULTS AND DISCUSSION

4.1 Chapter Overview

This chapter presents the results of the failure analysis performed on the shell and tube heat exchanger. The results of the fabricated In625/SS316L FGM are also presented. The results of the microstructural transformation are discussed through the use of optical and SEM micrographs. Peak intensity, contour plots and their relationship to compositional grading and process parameters are highlighted in the discussion of the results of the phase analysis. Finally, the created microstructure is validated with the optimization findings and the most important process parameter is identified.

4.2 Failure Analysis of Shell and Tube Heat Exchanger

The visual inspection results are interpreted in light of the mechanical study to clarify the mechanism by which the visible failure features emerged. Figure 3.1 shows the cross-section of the virtually inspected stacked exchanger tubes. White blockage media introduced to the exchanger by the Olkaria Company were observed at the tube end (see Figure 4.2), and found to correspond to the blocked dysfunctional tubes.

4.2.1 Visual inspection of the Tube Samples

On the contrary, the tubes at the outer region of the bore appeared to be in good shape and to be working properly.

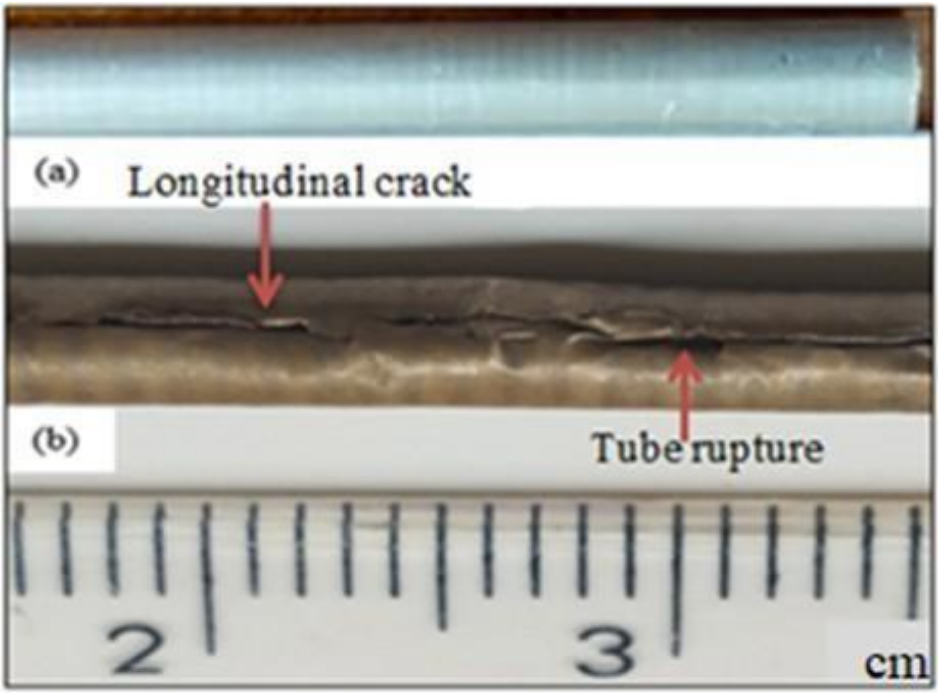

Figure 4.1: Failed Exchanger Tubes Examined (a) Intact Sample T1 (b) Fracture T2

To confirm this, the pressure was blown through the pipe and dysfunctional tubes were identified by leakage sound. This may indicate that corrosion predominantly took place at the centre because cracking was primarily concentrated at the tube bundle's centre and stretched along the tube's longitudinal direction, as illustrated in Figure 4.1 (b). This could also be due to the shell side turbulent pressure concentrated at the centre, implying that the exchanger failure emanated from the centre tubes due to high-stress concentrated regions.

The assertion on the occurrence of high-stress concentrations at the tubes located at the centre of the heat exchanger is corroborated by the outcomes of mechanical analysis of samples T1 and T2, see Figure 4.3. It is clear from Figure 4.3 that the failed tube (sample T2) exhibited high levels of tensile residual stresses with a value of positive 172 MPa. The presence of residual stress reduces the material fracture toughness, rendering the tube more likely to experience failure through crack propagation.

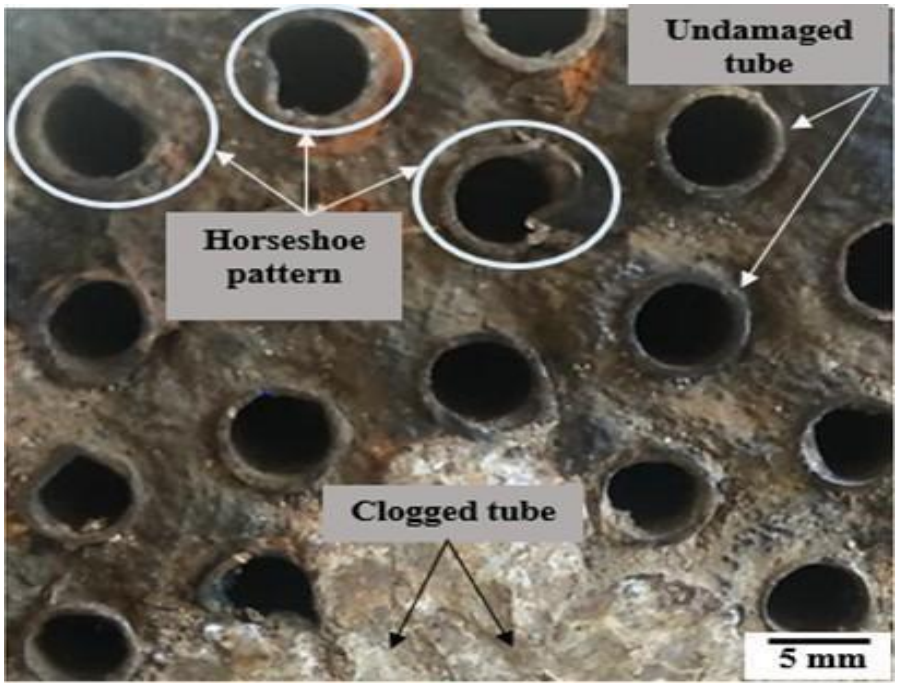

Figure 4.2: Top View of the Failed Heat Exchanger Tube Bundle

Compressive residual stresses, which are not harmful nor speed up tube deterioration were detected for sample 1. This is because compressive residual stresses on tube surfaces are suggested to prevent the movement or diffusion of hydrogen atoms. After all, they increase the material's hardness. Enhancing the integrity of the material reduces the diffusion and concentration of hydrogen concentration in the material, and the prevalence of hydrogen stress cracking is controlled. Meanwhile, the concentration of hydrogen invasion and ultimate cracking is exacerbated by tensile residual stresses since they suppress fatigue strength. Therefore, it can be inferred that the material quality of sample T1 was still in its integrity with less hydrogen concentration, thereby reducing the likelihood of hydrogen-induced cracking.

The peak profile of the intact tube had a low level of stress intensity, which affects the rate at which cracks propagate, and was distinguished by a thin blue lining to indicate decreased stress intensity. Figure 4.3 (a) shows the residual stress values for sample T1 (Intact tube) and sample T2 (failed tube), which were auto-generated by the residual stress analysing machine. It is evident from Figure 4.3 (a) that the failed tube has tensile residual stresses of positive 172 MPa, while the intact tube has compressive residual stresses of negative 56 MPa. The failed tube's distortion (Figure 4.3b) is also higher

than the undamaged tube's due to high-stress concentrations, measuring 2.823 mm, which supports the explanation behind the expanded region of the failed tube observed in Figure 3.1. Furthermore, the intact tube is more accurately depicted in Figure 4.3 (b) with a circumference that is close to circular, as opposed to the failed tube in Figure 4.3 (c) with a more distorted shape. In contrast, the failed tube's peak profile in Figure 4.3 (c) featured a thick peak profile with a yellow-red line signifying high-stress intensity.

A similar observation was reached by Usman & Khan (2008) when investigating ASTM A213 grade T11 heat exchanger tubes. They found that stresses induced by cyclic temperature swings caused tube cracking because of thermal fatigue, which indicates that stresses influence the material's resistance to degradation. Therefore, it can be argued that the CuNi experienced high stress levels beyond its yield point, leading to cracking, which in the presence of high sulphate content became sulphide-induced stress corrosion cracking. This was also seen in the work of Miyamoto et al. (2012), who investigated the stress corrosion cracking of pure copper and found that it was caused by the accumulation of residual stress and strain at grain boundaries.

In a related study, Xu et al. (2015) conducted a failure analysis on stainless steel heat exchanger tubes and concluded that SCC due to residual tensile stresses was the cause of premature failure, showing that tensile residual stresses can exacerbate the SCC failure mechanism.

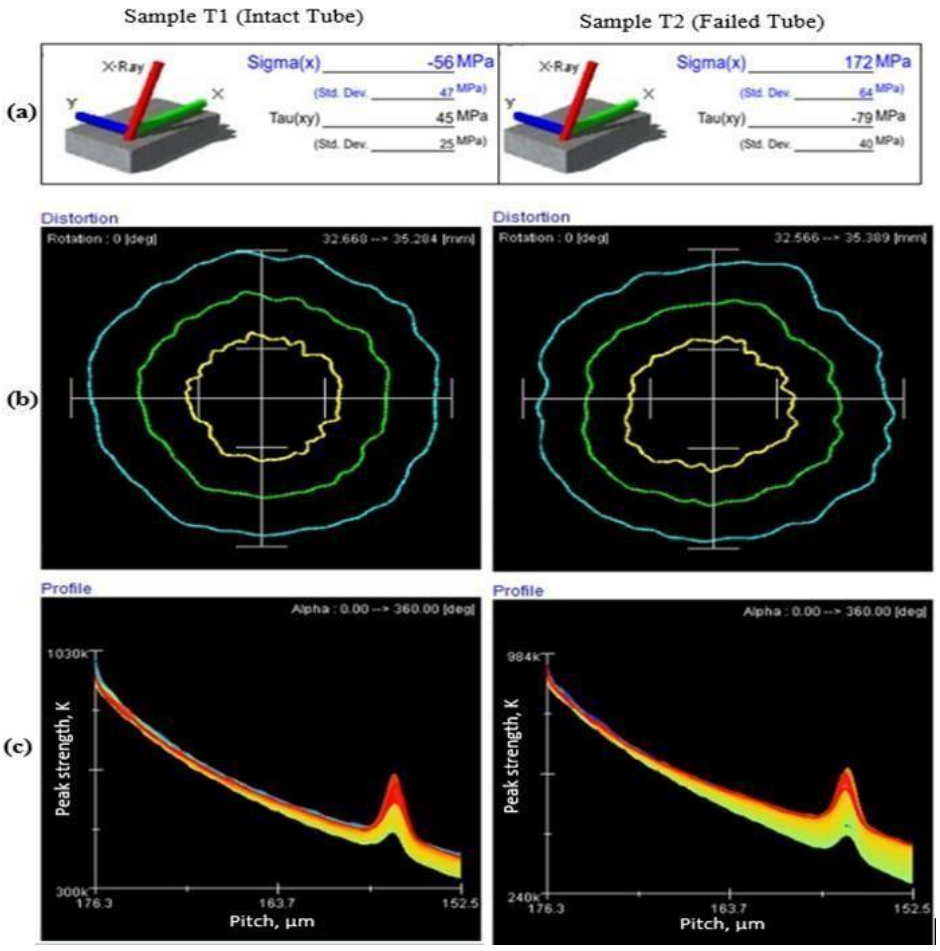

Figure 4.3: Measurement of Internal Residual Stresses at Tube Surface Compared for Sample T1 and T2 (a) Stress Values (b) Distortion (c) Residual Stress Profile

Furthermore, horseshoe patterns could be seen in the tube entrance, implying the occurrence of erosion. The horseshoe pattern is categorized by an extended circular arc with a narrow bottom view, just like typical horseshoeing (see Figure 4.2). This suggests that the tube took on a shape resembling a normal horseshoe footprint due to distortion spurred by high fluid pressure. Also, the high-pressure water turbulence encountered when water divides from the large pipe into the smaller diameter tubes at high velocities resulted in tube thinning and dislocation aggravated by abrasive particles in the fluid. Visual observations of the shell and tube heat exchanger cover also showed the presence of brownish-to-red corrosion products with black layers, as indicated in Figure 4.4. However, the gasket did not fail as it was intact with no signs of cracking or dislocation.

According to Chandra et al. (2014), the reddish-brown substance observed is a cuprous oxide (Cu_2O) formed when the copper reacts with air, acting as a protective film against degradation. In this case, it possibly eroded and washed away in the presence of corrosive products formed by chemical reactions. Corrosion product migration can occur in CuNi tubes, as seen in the work of (Mousavian et al., 2011) when corrosion products moved from the tube front-end into heat exchanger copper tubes.

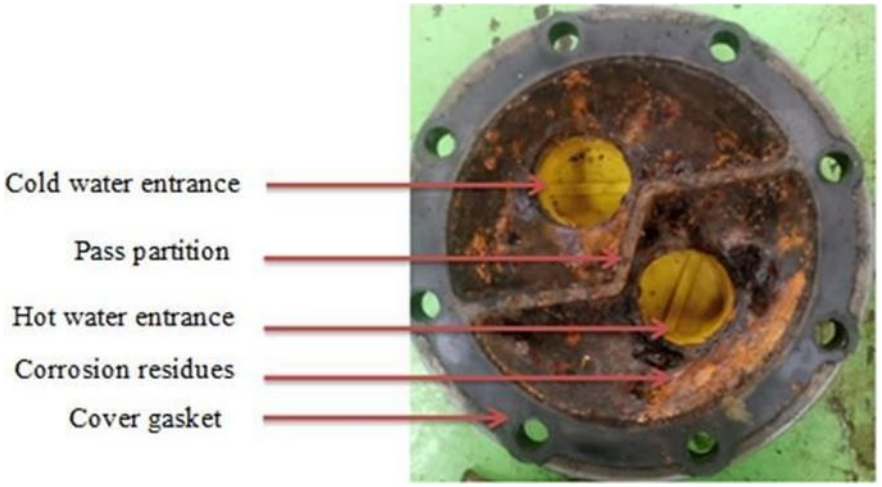

Figure 4.4: Corroded Heat Exchanger Cover Showing Brownish-to- Red Corrosion Products with Black Layers

4.2.2 Chemical Analysis of Water Samples and Corrosion Residue

Table 4.2 summarizes recorded values obtained for both industrial water (W1) and steam condensate (W2). The water analysis revealed that both samples W1 and W2 contain high sulfide content, which has been reported to be the main corrosion-degrading agent for sulphide stress cracking of pipelines. Studies have shown that sulfides, even at low concentrations (<10 ppm), can be lethal and cause corrosion in industrial plant equipment (Chan et al., 2022). However, it is seen from Table 4.2 that sample W2 contain higher content sulphates relative to W1. This is due to the chemical reactions that led to the formation of corrosion products, as can be seen with an increase in totally dissolved solids and conductivity. Because of this, sul- phates are believed to have caused stress corrosion cracking. Generally, when a material under stress (or

residual stress) is exposed to sulphur-induced contaminants or sulphates, it becomes susceptible to sulphide stress corrosion cracking.

Tuck & Emea (2016) posited that, while cupronickel is not frequently prone to sulphide stress corrosion cracking in fluids containing low sulphate concentrations, it can experience catastrophic pipe failure when the sulphate concentration is high (>100 ppm). Based on this argument, it is certain the high sulphate content in the industrial water contributed to crack propagation. On the other hand, excess chloride content is also reported to contribute to stress corrosion cracking. (Wang et al., 2019) revealed that copper can be oxidized in a reaction with water and chloride ions, causing the replacement of the Cu_2O oxide layer with chloride ions, and eventually leading to pit formation and crack growth. Corte et al. (2015) established that the high chloride content contained in the cooling water initiated cracks leading to SCC failure. Therefore, it is highly probable that the chloride ions in the present study contributed to pit formation.

4.2.3 X-Ray Fluorescence Analysis

The corrosion residues from the tube bundle and shell cover were analysed using Brukers XRF machine for elemental analysis. The elements greater than 1% picked in XRF analysis were iron oxide (Fe3O4), silicon dioxide (SiO2), aluminium oxide (Al2O3), and sulphur, respectively.

The compounds discovered in the residues are represented graphically in Figure 4.5 except for (Fe_3O_4), which was present in excess and balanced the composition. The pit formation of CuNi pipes due to iron oxidation led to the depletion of iron in the presence of H2S, which gave room for the diffusion of hydrogen ions and susceptibility of embrittlement, resulting in hydrogen-induced cracking in sulfide- concentrated environment. This is evidenced by the black and orange-brown colour of the corrosion residues that were examined, referred to as iron oxide, and commonly known as rust. Furthermore, the presence of sulphur was observed to be excessive. It can lead to sulfidation that results in sulphide or sulphate formation due to the compounds triggered by Fe and Ni, which are significant contributions and responsible for acceleration

corrosion in copper-nickel tubes and cracking. Thus, the presence of iron in the corroded powder could mean iron was oxidized at the anode to its ferrous form and reacted with steam containing hydrogen sulfide at the cathode, forming an unprotected iron oxide (Fe_3O_4). Figure 4.6 also shows the degrading mechanism in the presence of magnetite, which is a product of iron oxide, is formed on the steam side of the boiler tubes under high pressure and high temperature in a humid environment.

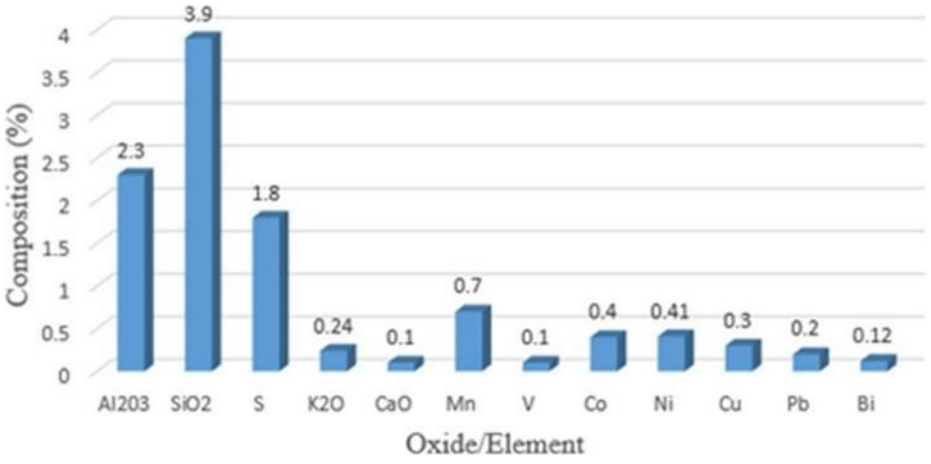

Figure 4.5: Elemental Distribution and Composition of Corrosion Residue

Table 4.1: Chemical Composition of the Water Circulating in the Heat Exchanger

Elements	Steam condensate	Corroded water
Total dissolved solids, TDS (ppm)	218	1833
pH level	6.89	8.10
Turbidity, NTU	4.6	430.8
Conductivity (μS/cm)	340.10	2860
Chloride ions, Cl^-(ppm)	8.25	23.75
Total Phosphates, PO_4(ppm)	0.02	0.045
Sulphates, $^{2-}SO^{2-}$(ppm)	1159.59	1248.06
Ammonia nitrogen, NH_4(ppm)	47.1	258.61
Sulfides (ppm)	49.5	126.27
Nitrates, $^{-NO}3-$(ppm)	2.36	26.8
Magnesium, Mg	0.98	1.55
Sodium, Na	6.08	11.3
Potassium, K	0.94	3.21
Zinc, Zn	0.02	0.03
Iron, Fe	0.01	1.4
Calcium, Ca	0.22	2.16

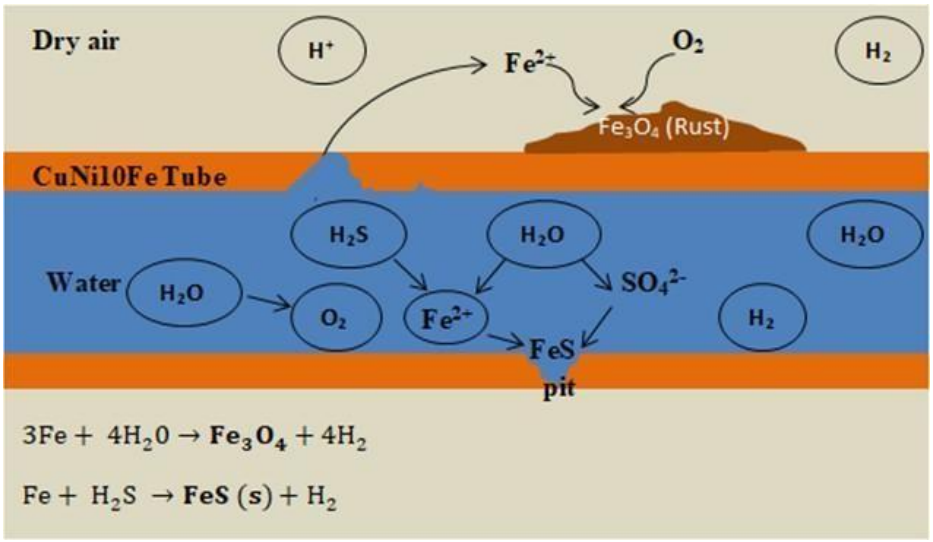

Figure 4.6: Schematic Illustration of the Corrosion Process of CuNi10Fe

Figure 4.6 attempts to explain the chemical process of degradation that could have led to tube rapture. The presence of hydrogen sulfide (H_2S) could have caused a chemical reaction to occur during interaction with steam (H_2S), leading to wet sulfide and hydrogen molecules (H_2). Since cupronickel pipes contain iron elements (Fe), it is

possible that iron reacted in an oxygen-reach environment, leading to the formation of rust (Fe_3O_4). On the other hand, the reaction of the iron element with the sulfur element led to the formation of iron sulfide (FeS), which is generally known for pit formation. The prevalence of pits is what could have aggravated the escape of oxides and hydrogen into the microstructure, leading to hydrogen embrittlement, and ultimate rupture when excessive pressure was applied to the tubes.

4.2.4 Optical Microscopy Analysis

The optical micrograph in Figure 4.7 shows the microstructure of the failed tube. The thinning of the tube lining characterized by pits can be seen along the surface. In the examined case, it is apparent that the direct contact of the cupronickel surface with degrading impurities particularly sulphates, resulted in micro-segregation of elements and pit formation along the grain boundaries.

Figure 4.7: Micrographs of Heat Exchanger Tubes (a) Failed Tube with Surface Defects (b) Intact Heat Exchanger Tube with Less Surface Distortion (c) Surface Cracks Pits Growing from the Inside

According to Yang et al. (2020), sulphur segregation can damage grain boundaries and cause cracking corrosion. This is explained by the fact that vanadium and sulphur together can produce salts, which can cause sedimentation and pit development. Pits crack when they experience tensile tension. On the contrary, the wall thickness of the intact tube is seen to be compact with cracks and pits, which could be the reason that the tubes did not rupture, leak, or fail during service. Meanwhile, the intact tube also experienced erosion wear since the circumferential thickness was not uniform. This suggests the first mechanism of degradation was erosion-wear of the tube wall, followed by pit formation and crack due to depletion of the protective layer.

4.2.5 Scanning Electron Microscopic and EDS Analysis

Scanning electron microscopic (SEM) analysis was employed in this study to identify the microstructure, morphology, point of origin, orientation, and growth of the cracks. EDS analysis helped to determine the chemical composition of inclusions and corrosion residues present in the corroded exchanger tubes. Figure

4.8 shows the fracture surface of the failed tube with surface pits visible at the outer edge of the tube wall. Additionally, a primary crack branch can be seen propagating from the tube surface, taking the form of SCC caused by a sulphide- rich medium. This could mean some chemical reactions took place and led to an attack on the tube lining.

Ziaei et al. (2014) observed the same failure pattern for the control valve body of the A216-WCC weld head. The wet, H_2S-rich atmosphere was cited as the source of sulfide stress corrosion cracking. Surface pits with corrosion by-products are a defining feature of sulphide-induced SCC. In the present study, the crack branching could be due to the direct contact of the pipe's external surface with H_2S during service at the geothermal power plant.

In the geothermal environment, CuNi10Fe interacts with hydrogen sulphide gas to produce corrosion products including metal sulphides (MeS) and atomic hydrogen (H), which combine to generate H2. The created H2 then disperses into the matrix of the material. As a result, the material develops cavities and loses its mechanical strength.

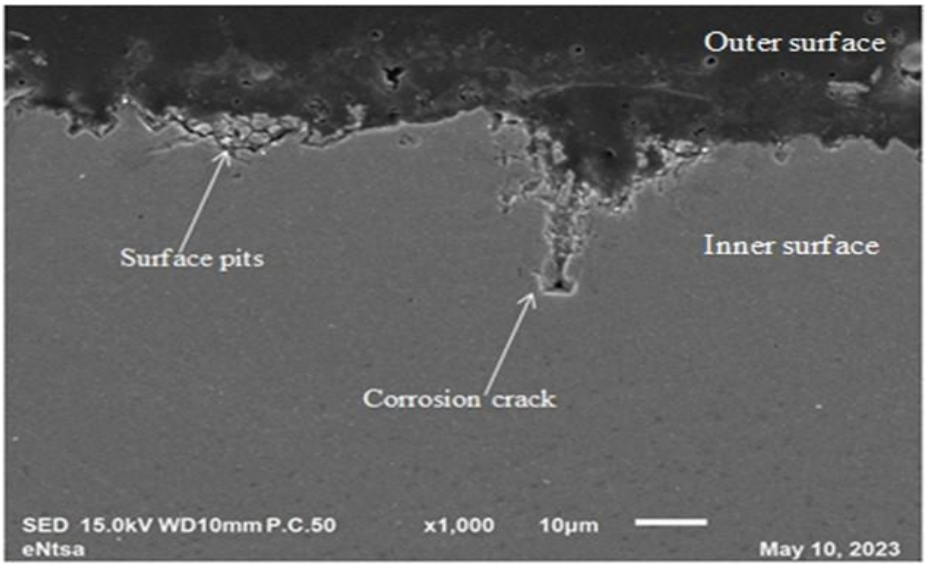

Figure 4.8: SEM Morphology of Sulphide-Induced Corrosion Crack

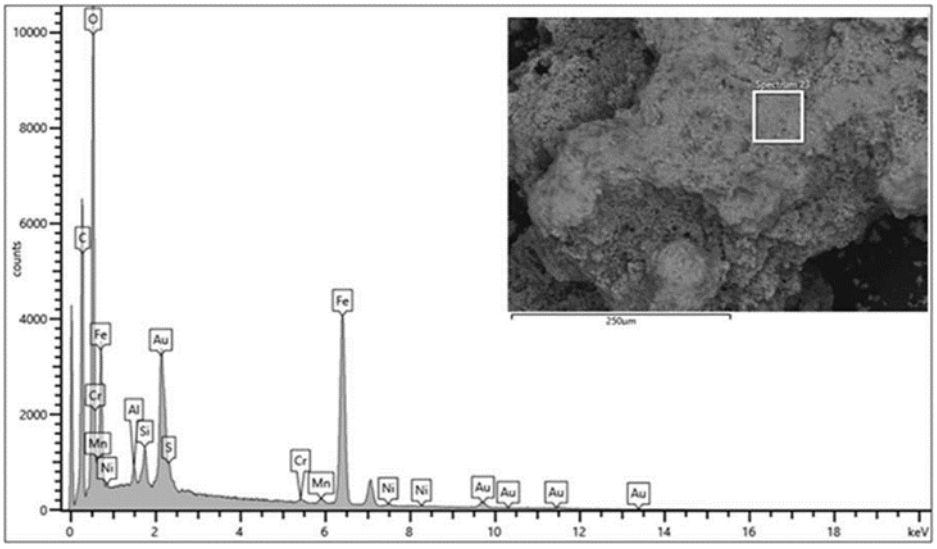

Figure 4.9: Feature of the Corrosion Residues and the Spectrum of SEM Elemental Analysis

These voids can trigger the primary crack propagating (hydrogen induced cracks) and ultimate tube rapture through sulphide stress cracking mechanism when the material being subjected to high fluid pressures.

Table 4.2: Chemical Composition of the Exchanger Tubes and Corrosion Residue

Element	Cu	Fe	S	Cl	O	Ca	Mn	Si	Al	Ni
Corrosion residues	-	60.28	1.24	-	33.24	-	1.19	1.71	0.97	0.83
Intact (wt. %)	83.11	1.76	0.33	0.29	2.87	0.30	0.74	-	-	10.60
Failed (wt. %)	89.22	-	-	-	9.38	-	-	-	-	1.40

Figure 4.10 shows the micro-cracks due to hydrogen voids, leading to hydrogen-induced cracks. When the material continues being subject to applied stress during service, the crack propagates. This mechanism of degradation has been reported by several researchers in the cited literature.

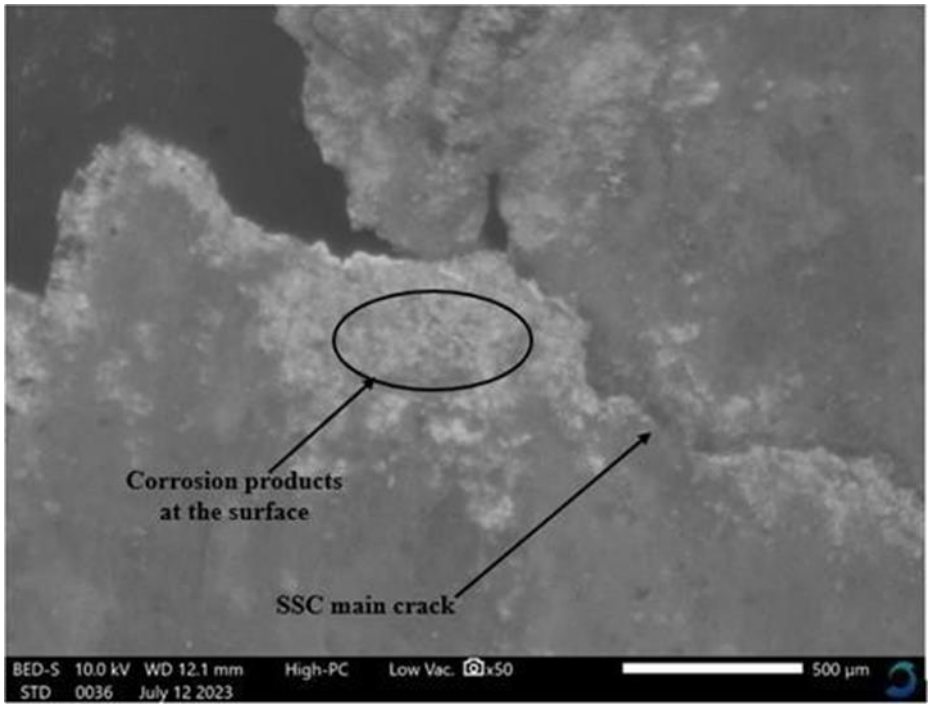

Figure 4.10: SEM Micrographs Showing the Main Crack at the Surface Due to Sulfide Stress Cracking

4.2.5 X-Ray Diffraction Analysis

The corrosion residue that was scraped from the heat exchanger is depicted in Figure 4.11 using an XRD pattern. The spectrum reveals the existence of several phases, including magnetite (Fe3O4), lepidocrocite (FeO2), goethite (FeHO2), and chromium iron oxide (Cr2FeO4).

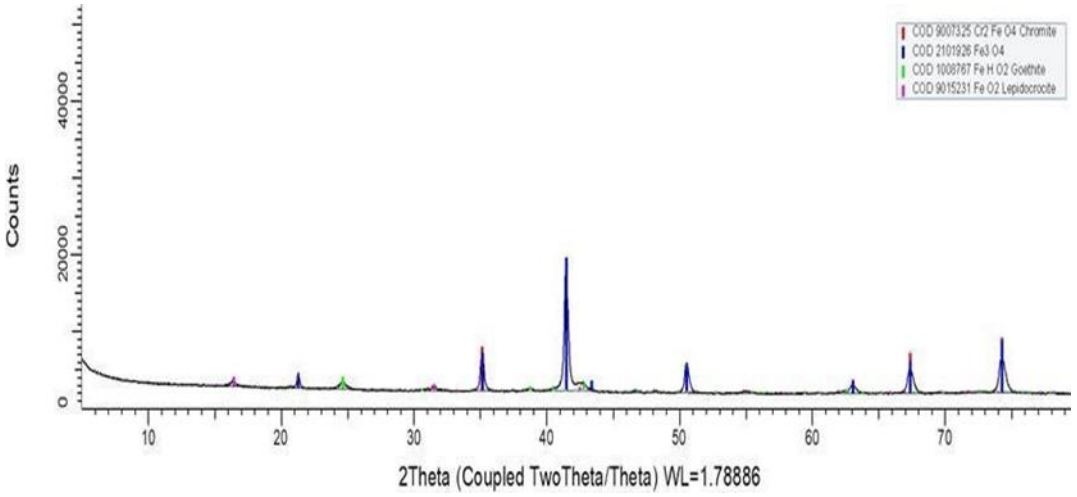

Figure 4.11: XRD Pattern of Corrosion Residues from CuNi10Fe Failed Tube

Cupronickel pipes benefit from the strengthening elements of iron and manganese. However, the oxidation of iron can form corrosion products that aggravate the corrosion mechanism. According to the findings, the most prevalent oxide that formed as a deposit on the tube surface is iron oxide (Fe_3O_4). This suggests that the catalytic reaction at the tube surface caused by the iron oxide deposits developed as a result of oxidation led to pit development at the surface, as shown in Figure 4.12.

4.2.6 Mitigation Measures to Combat the Degradation of Heat Exchangers

The findings suggest that the heat exchanger's premature failure was caused by inappropriate material choice, poor tube design for the high-pressure application, and hostile operating conditions. Hence, there is a need to redesign the tube to increase thickness which will transform it into a pipe structure which accommodates large applications because tubes are used where small diameters

are required. Also, the coating will be applied on the tube outside/external surface. This shall be meant to protect the pipe from hydrogen-induced cracking that was observed to cause failure at the surface, though it emanated from the inside of the tube.

Additionally, the surface coating at the outside surface will mitigate wear at the tube entrance, which was reported to be at the tube surface. Therefore, to avoid such shortcomings, careful selection is required to identify a material resistant to sulphur-

induced stress corrosion cracking and one that can withstand iron oxidation. This includes materials such as Inconel 625 and stainless steel 316L that have high corrosion resistance and high strength in severe operating conditions. These materials can also be applied as surface coatings to prevent degradation. Functionally graded materials (FGMs) are an emerging class of novel materials that can be used as surface modifiers. FGMs are realized through the combination of materials with different material properties, varied spatially over volume, and custom-tailored for a specific function. For instance, an FGM comprising stainless steel 316L/Inconel 625 can be used to improve the corrosion resistance of CuNi10Fe on the tube inside the wall by taking advantage of the excellent corrosion resistance of stainless steel 316L, while improving the wear resistance properties on the outside due to the high strength of Inconel 625, as shown in Figure 4.12.

The findings of this study were used to formulate an experimental work to fabricate a functionally graded SS316L/IN625 material on a copper substrate in future. This shall comprise the use of the laser cladding tech- nique, followed by heat treatment to reduce the residual stresses generated during manufacturing. In addition, it is necessary to modify the exchanger tubes and employ acrolein to treat hydrogen sulfate in condensate because it is a less expensive approach.

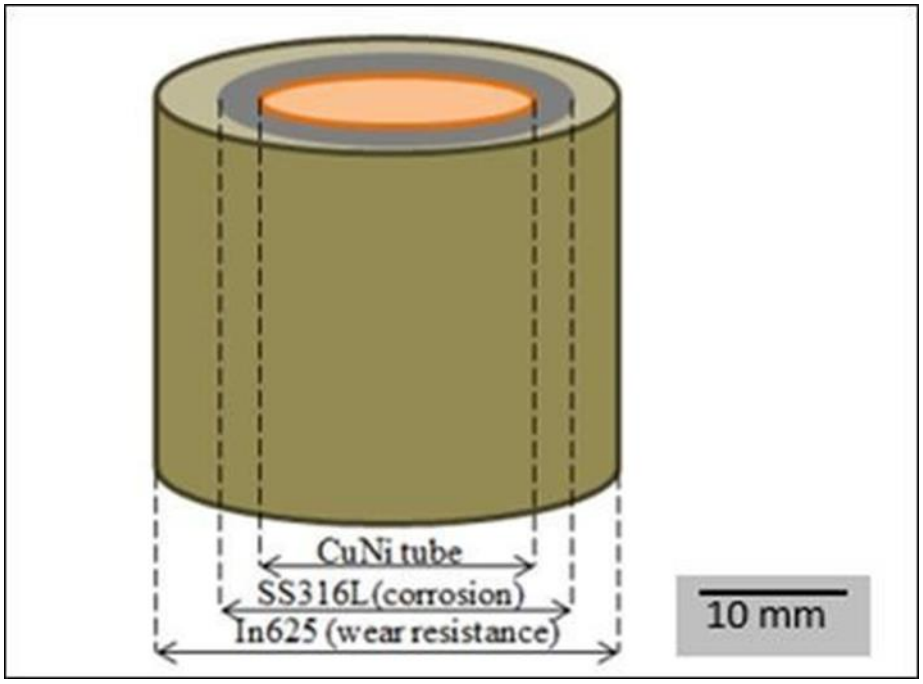

Figure 4.12: Illustration of SS316L/IN625 Functionally Graded Coating on CuNi Tube

4.2.6.1 Taguchi-Grey Relational Analysis

The multi-objective optimization problem was addressed using the grey relational analysis (GRA) method, which made use of the Taguchi experimental matrix to determine the ideal values. Optimum parameters were evaluated using a five-step procedure (i) acquiring output responses (ii) normalization of the data (iii) computing deviation sequence (iv) calculating the grey relational coefficient and grey relational grade of normalized data and (v) computing the average GRG using values of the Taguchi matrix.

Table 4.3: GRA Experimental Output Responses for Quality Characteristics

	Input parameter			Output Parameters											
	A	B	C	Aspect ratio (mm)			Microhardness (HV)			Surface roughness (Ra)			Porosity (%)		
Exp				TR1	TR2	TR3	TR1	TR2	TR3	TR1	TR2	TR3	TR1	TR2	TR3
1	1	1	1	1.94	1.95	1.93	235.00	234.00	232.90	6.55	7.11	6.60	0.04	0.04	0.0
2	1	2	2	1.96	1.96	2.03	239.83	238.21	237.65	6.00	6.97	6.10	0.27	0.25	0.3
3	1	3	3	2.12	2.14	2.11	253.00	250.00	245.00	10.75	9.65	10.88	0.18	0.19	0.2
4	2	1	2	1.71	1.7	1.69	221.41	222.40	220.00	11.51	10.10	11.74	0.04	0.03	0.0
5	2	2	3	2.11	1.88	1.90	225.81	227.00	227.30	10.13	11.40	10.10	0.15	0.15	0.1
6	2	3	1	3.59	3.68	3.61	240.67	241.89	242.60	5.66	5.99	5.60	0.03	0.02	0.0
7	3	1	3	1.17	1.15	1.71	207.00	209.00	198.76	14.13	16.80	15.20	0.48	0.57	0.5
8	3	2	2	1.99	2.01	1.92	230.67	233.27	233.40	7.22	8.37	7.50	0.04	0.05	0.0
9	3	3	1	1.43	2.15	2.10	230.34	230.10	230.70	10.73	11.50	10.80	0.34	0.35	0.4

4.2.6.2 Taguchi L9 Orthogonal Array Output Data

The Taguchi method uses the relation between the input and the output to determine variance and response settings. The experimental samples obtained from Table 2 of the Taguchi L9 OA were measured for the quality characteristics (aspect ratio, microhardness, and porosity) and the results are shown in Table 4.3. Thereafter, the results were transformed into Table 4 using signal-to-noise (S/N) ratios of the Analysis of Variance (ANOVA) method.

4.2.6.3 Data Normalization

The Taguchi method reduces variability in a process by minimizing uncontrollable factors referred to as noise factors. Higher signal-to-noise (S/N) values are used to minimize noise factors. Different S/N ratios can be selected to maximize or minimize the responses. In this study, the S/N ratio for higher the better maximized the microhardness and aspect ratio, while the S/N ratio for lower the better minimized the porosity and surface roughness. Equations 4.1 and 4.2 were used for normalizing larger-the-better and smaller-the-better, respectively.

Table 4.4: Normalized Response Values for Output Variables

N	TR1	TR2	TR3	TR1	TR2	TR3	TR1	TR2	TR3	TR1	TR2	TR3
1	0.3123	0.3162	0.3083	0.6681	0.6497	0.6294	0.9152	0.8652	0.9107	0.9636	0.9636	0.9818
2	0.3202	0.3202	0.3478	0.7572	0.7273	0.7170	0.9643	0.8777	0.9554	0.5455	0.5818	0.4182
3	0.3834	0.3913	0.3794	1.0000	0.9447	0.8525	0.5402	0.6384	0.5286	0.7091	0.6909	0.6364
4	0.2213	0.2174	0.2134	0.4176	0.4358	0.3916	0.4723	0.5982	0.4518	0.9636	0.9818	0.9636
5	0.3794	0.2885	0.2964	0.4987	0.5206	0.5262	0.5955	0.4821	0.5982	0.7636	0.7636	0.7273
6	0.9644	1.0000	0.9723	0.7727	0.7952	0.8083	0.9946	0.9652	1.0000	0.9818	1.0000	0.9818
7	0.0079	0.0000	0.2213	0.1519	0.1888	0.0000	0.2384	0.0000	0.1429	0.1636	0.0000	0.1273
8	0.3320	0.3399	0.3043	0.5883	0.6362	0.6386	0.8554	0.7527	0.8304	0.9636	0.9455	0.9636
9	0.1107	0.3953	0.3755	0.5822	0.5778	0.5889	0.5420	0.4732	0.5357	0.4182	0.4000	0.2909

Aspect ratio (mm) Microhardness (HV)Surface roughness (Ra) Porosity (%)

Table 4.4 presents the normalized values of the S/N response variables.

$$X_p(j) = \frac{Y_p(j) - \min(Y_p(j))}{\max(Y_p(j)) - \min(Y_p(j))}$$

$$X_p\prime(j) = \frac{Y_p(j) - \min(Y_p(j))}{(\max(Y_p(j)) - \min(Y_p(j))} \tag{4.2}$$

Where $X_p(j)$ and $X_p^{'}(j)$ are the normalized S/N ratios, $Y_p(j)$ is the corresponding experimental S/N value, and max $Y_p(j)$ and min $Y_p(j)$ are the maximum and minimum Taguchi *S/N* ratio values.

4.2.6.4 Deviation Sequence

The deviation sequence is denoted by Δ_{oi} (j) and computed using equation 4.3 to evaluate the complete variance. Table 5 displays the results for the normalized response deviation.

$$\Delta_{oi}(j) = |x'(j) - x'(j)| \tag{4.3}$$

4.2.6.5 Grey Relational Coefficient and Grey Relational Grade

The grey relational coefficient (GRC), denoted by δ, is used to measure the correlation between two responses. It is computed using Equation 4.4. Thereafter, the grey relational grade (GRG) is computed by taking the average of all the GRC (MH, AR, SR, P), and the results are presented in Table 4.6.

$$\delta_{ij} = \frac{\Delta_{min} + \epsilon\Delta_{max}}{\Delta_{ij} + \epsilon\Delta_{max}} \tag{4.4}$$

where ϵ is the distinguishing coefficient taken as 0.5, Δ is the deviation and δ_{max} and Δ_{min} denote the maximum and minimum absolute differences, respectively. Table 4.6 gives a summary of the GRC and GRG values. The rank was calculated using the GRG

values, with the highest values indicating the most desirable clad quality characteristics with favourable conditions.

Table 4.7 shows the Analysis of Variance (ANOVA) response table of the grey relational grade, meant to identify the parameter that most significantly influences the performance attributes. The parameters were ranked by significance using the sum of squared deviation for the entire variability of the grey relational grade. The findings show that, with the highest percentage of 47.36%, scanning speed has the greatest influence on performance characteristics, while laser power and powder flow rate were the least significant with a percentage of 26.33 and 26.31%, respectively. Additionally, the ideal values for the laser power, scanning speed, and powder flow rate, respectively, correspond to levels 2, 3, and 1 (2-3-1). This implies that the sample 6 parameters exhibited the highest performance characteristics, including higher microhardness and aspect ratio, reduced porosity, and smoother surface, at a laser power of 850 W, scanning speed of 600 mm/min, and powder flow rate of 2 g/min.

Table 4.5: Deviation Sequences of the Normalized Responses

N	TR1	TR2	TR3	TR1	TR2	TR3	TR 1	TR2	TR3	TR1	TR2	TR3
1	0.6877	0.6838	0.6917	0.3319	0.3503	0.3706	0.0848	0.1348	0.0893	0.0364	0.0364	0.0182
2	0.6798	0.6798	0.6522	0.2428	0.2727	0.2830	0.0357	0.1223	0.0446	0.4545	0.4182	0.5818
3	0.6166	0.6087	0.6206	0.0000	0.0553	0.1475	0.4598	0.3616	0.4714	0.2909	0.3091	0.3636
4	0.7787	0.7826	0.7866	0.5824	0.5642	0.6084	0.5277	0.4018	0.5482	0.0364	0.0182	0.0364
5	0.6206	0.7115	0.7036	0.5013	0.4794	0.4738	0.4045	0.5179	0.4018	0.2364	0.2364	0.2727
6	0.0356	0.0000	0.0277	0.2273	0.2048	0.1917	0.0054	0.0348	0.0000	0.0182	0.0000	0.0182
7	0.9921	1.0000	0.7787	0.8481	0.8112	1.0000	0.7616	1.0000	0.8571	0.8364	1.0000	0.8727
8	0.6680	0.6601	0.6957	0.4117	0.3638	0.3614	0.1446	0.2473	0.1696	0.0364	0.0545	0.0364
9	0.8893	0.6047	0.6245	0.4178	0.4222	0.4111	0.4580	0.5268	0.4643	0.5818	0.6000	0.7091

Aspect ratio (mm) Microhardness (HV) Surface roughness (Ra) Porosity (%)

Table 4.6: Grey Relational Coefficient, Grey Relational Graded, and their Ranking

	Grey relational coefficient			Grey relational grade		
Exp. No	Aspect ratio	Microhardness	Surface roughness	Porosity	GRG	Rank
1TR1	0.4210	0.6011	0.8550	0.9322	0.702299	4
1 TR2	0.4224	0.5880	0.7876	0.9322	0.682557	6
1 TR3	0.4196	0.5743	0.8485	0.9649	0.701825	5
2 TR1	0.4238	0.6731	0.9333	0.5238	0.638512	11
2TR2	0.4238	0.6471	0.8034	0.5446	0.604721	14
2 TR3	0.4340	0.6386	0.9180	0.4622	0.613187	13
3 TR1	0.4478	1.0000	0.5209	0.6322	0.650225	9
3 TR2	0.4510	0.9004	0.5803	0.6180	0.637417	12
3 TR3	0.4462	0.7722	0.5147	0.5789	0.578018	16
4 TR1	0.3910	0.4619	0.4865	0.9322	0.567926	17
4 TR2	0.3898	0.4699	0.5545	0.9649	0.594763	15
4 TR3	0.3886	0.4511	0.4770	0.9322	0.562234	18
5 TR1	0.4462	0.4994	0.5528	0.6790	0.544347	19
5 TR2	0.4127	0.5105	0.4912	0.6790	0.523377	21
5 TR3	0.4154	0.5134	0.5545	0.6471	0.532598	20
6 TR1	0.9336	0.6875	0.9894	0.9649	0.893836	3
6 TR2	1.0000	0.7094	0.9349	1.0000	0.911071	1
6 TR3	0.9476	0.7228	1.0000	0.9649	0.908823	2
7 TR1	0.3351	0.3709	0.3963	0.3741	0.369117	25
7 TR2	0.3333	0.3813	0.3333	0.3333	0.345332	27
7 TR3	0.3910	0.3333	0.3684	0.3642	0.364257	26
8 TR1	0.4281	0.5484	0.7756	0.9322	0.671087	7
8 TR2	0.4310	0.5789	0.6691	0.9016	0.645142	10
8 TR3	0.4182	0.5805	0.7467	0.9322	0.669383	8
9 TR1	0.3599	0.5448	0.5219	0.4622	0.472192	24
9 TR2	0.4526	0.5422	0.4870	0.4545	0.484070	22
9 TR3	0.4446	0.5488	0.5185	0.4135	0.481364	23

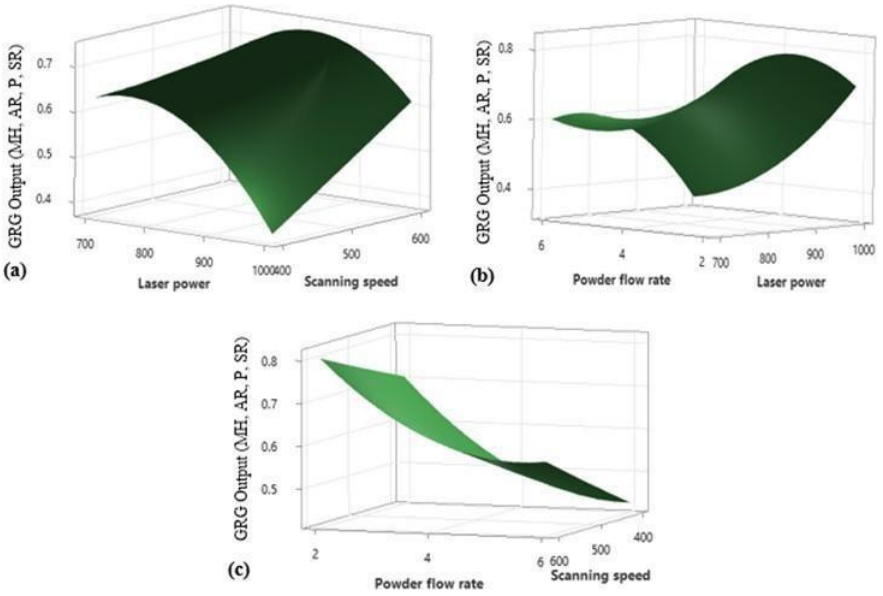

Figure 4.13: Surface Plot Interaction of Process Parameters on GRG Output for (a) Scanning speed, Laser Power (b) Powder Flow Rate, Laser Power (c) Powder Flow Rate, Scanning Speed

Figure 4.13 (a) shows the interaction of laser power and scanning speed with GRG output of FGM-clad quality characteristics (MH, AR, P, and SR). It can be seen that when the powder flow rate is set at zero level, the highest GRA output is obtained when laser power and scanning speed are is set at 700 to 850 W, and 500 to 600 mm/min, respectively. Meanwhile, when scanning speed is set at zero, the GRG output in Figure 4.13 (b) shows laser power and powder flow rate interaction, whereby a higher GRG value is obtained at 900W laser power and 3 g/min of powder flow rate. Figure 4.13 (c) shows that increasing scanning speed to 6 mm/min and lowing powder flow rate to 2 g/min significantly enhance the clad qualities.

Table 4.7: Architecture for Different Trials Employed in ANN Predicting

Trial No.	Network Structure	Mean Square Error	R values			
			Training	Validation	Testing	All
1	$3-2-1$	0.0022	0.9012	0.9980	0.9987	0.9061
2	$3-4-1$	0.0001	0.9933	0.9970	0.9798	0.9889
3	$3-6-1$	0.0056	0.9882	1.0000	0.9940	0.9902
4	$3-8-1$	0.0002	0.9254	0.9988	0.9208	0.9419
5	$3-10-1$	0.0027	0.9968	0.9491	0.9836	0.9878
6	$3-12-1$	0.0038	0.9863	0.9905	0.9996	0.9901
7	$3-14-1$	$4.0343e-04$	0.9880	0.9996	0.9973	0.9901
8	$3-16-1$	$4.2555e-04$	0.9893	0.9999	0.9876	0.9901
9	$3-18-1$	0.0012	0.9684	0.9933	0.9995	0.9746
10	$3-20-1$	$4.3435e-04$	0.9899	0.9854	0.9534	0.9900

The topology of the neural network model comprising GRC values as inputs (laser power, scanning speed, and powder flow rate), four hidden layers, and GRA values as the outputs parameter is presented in Figure 4.14. The model was created using all the GRA experimental output as data and trained using the Levenberg- Marquardt back propagation (LMBP) algorithm to predict GRG values. Thereafter, the mean square error (MSE) and the R-value were used to measure the performance of the model computed using the transfer function utilizing the tangent sigmoid for hidden layers and output as a linear function model.

This was based on the approach adopted by Maodzeka et al. (2023); Lin (2012); Wakchaure et al. (2018).

The hidden layer architecture was chosen because it gave the least MSE. The R values of 0.98883 training, 0.99968 testing, 0.99969 validating, and 0.99311 of the overall prediction were used to evaluate the performance of the model, as shown in Figure 4.7. The trials using various network architectures are presented in Table

4.8. The network structure (3-4-1) gave the best value because of the lowest MSE, and the regression plot is shown in Figure 4.15.

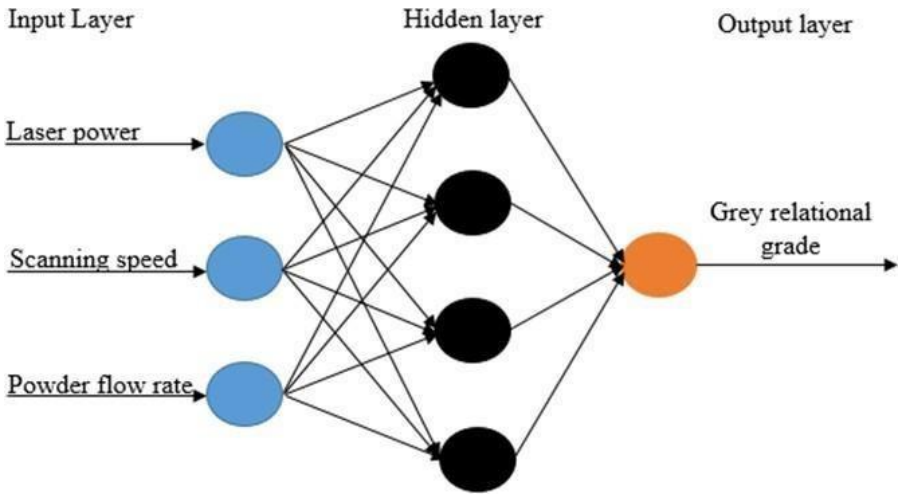

Figure 4.14: Topology of the Developed ANN Model

In choosing the data set for training and testing, a random selection technique was used, with 80% of the data used for training, 10% for testing, and 10 % for training. The training was focused on minimizing the mean square error (MSE) and the average prediction error (Etr), which are computed by equations 4.5 and 4.6, respectively. The best fit of the regression plot is presented in Figure 4.15. Additionally, the ANN efficiency for predicting GRG values was explored by comparing the results with the average GRG output for experimental results, and the results are presented in Table 4.9. It can be seen that the ANN-developed model has a better prediction accuracy and the GRGs obtained have a mean percentage error of 0.002 and a prediction accuracy of 99.15 %, showing that the ANN model can be used for optimizing the experimental GRG (see Figure 4.16).

$$MSE = \frac{1}{p}\sum_{p}\sum_{i}(T_{ip} - O_{ip})^2$$

$$E_{tr}(y) = \frac{1}{N}\sum_{i=1}^{N}|(T_i(y) - O_i(y))| \qquad (4.6)$$

Table 4.8: Comparison of the GRG Values Predicted by ANN and Those Calculated by GRA

Trial No.	Experimental GRG	ANN Predicted GRG	Network Error
1 TR1	0.702299	0.692045	0.010253
1 TR2	0.682557	0.628078	0.010433
1 TR3	0.701825	0.608563	0.041662
2 TR1	0.638512	0.574855	-0.006930
2 TR2	0.604721	0.527197	0.017150
2 TR3	0.613187	0.894094	-0.000259
3 TR1	0.650225	0.357876	0.011240
3 TR2	0.637417	0.647749	0.023337
3 TR3	0.578018	0.494340	-0.022148
4 TR1	0.567926	0.692045	-0.009488
4 TR2	0.594763	0.628078	-0.023357
4 TR3	0.562234	0.608563	0.028854
5 TR1	0.544347	0.574855	0.019908
5 TR2	0.523377	0.527197	-0.003820
5 TR3	0.532598	0.894094	0.016976
6 TR1	0.893836	0.357876	-0.012545
6 TR2	0.911071	0.647749	-0.002607
6 TR3	0.908823	0.494340	-0.010271
7 TR1	0.369117	0.692045	0.009780
7 TR2	0.345332	0.628078	-0.014891
7 TR3	0.364257	0.608563	-0.030545
8 TR1	0.671087	0.574855	-0.012622
8 TR2	0.645142	0.527197	0.0054008
8 TR3	0.669383	0.894094	0.0147286
9 TR1	0.472192	0.357876	0.0063804
9 TR2	0.484070	0.647749	0.021633
9 TR3	0.481364	0.494340	-0.012976

Figure 4.16 establishes that the ANN predictive model agrees well with the experimental GRA, showing that the chosen architecture can be employed to predict the GRG of performance characteristics without carrying out exper- iments. It also affirms that the developed prediction model agrees well with the experimental results.

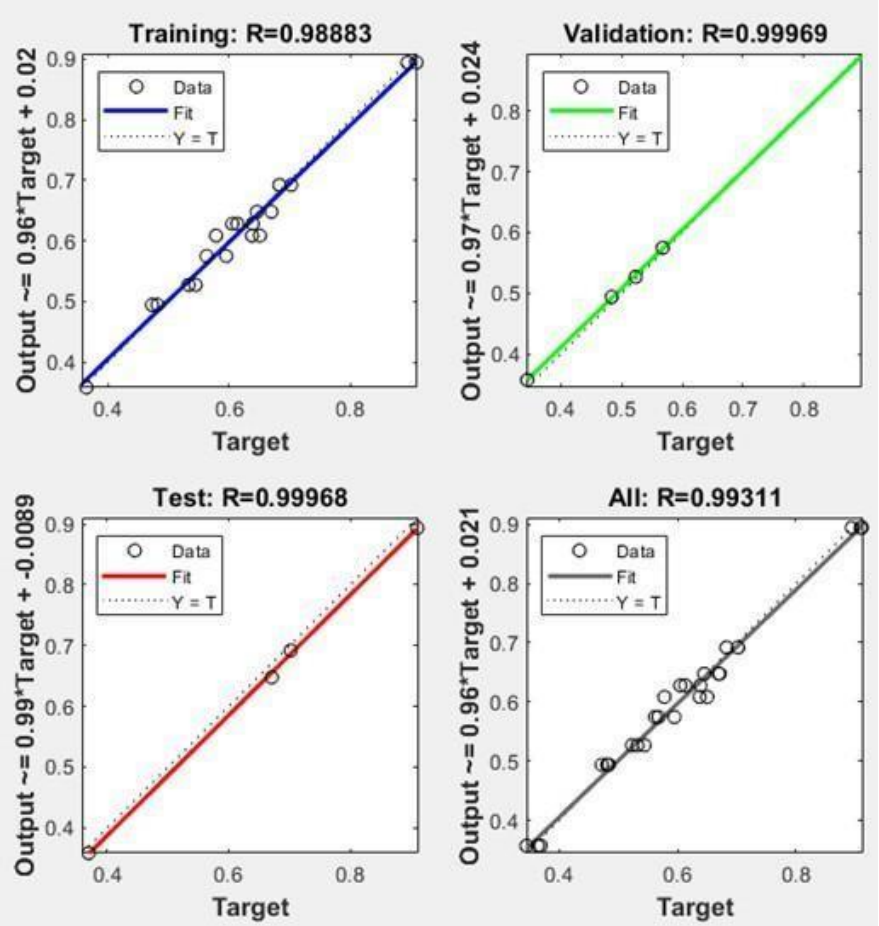

Figure 4.15: Regression Plot of the Developed Model

4.3 Effects of Process Parameter on Clad Quality Characteristics

The fabricated samples were characterized and the influence of process parameters on the MH, AR, P, and SR attributes are detailed in this section.

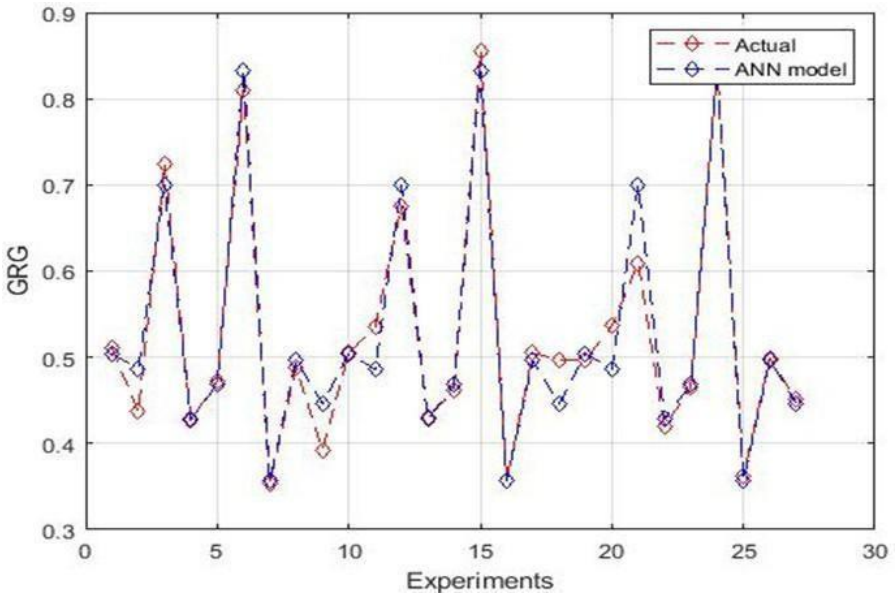

Figure 4.16: Comparative Analysis of ANN Simulated GRG with the Experimental GRG

Effects of process parameters on the microhard- ness properties The main effects plots of laser power, scanning speed, and powder flow rate S/N ratios are shown in Figure 4.17. It can be seen that microhardness increases when the scanning speed is increased from 400 to 600 mm/min (Figure 4.17b). This is because when speed is increased, the interaction time during deposition will be reduced, leading to a thicker layer and coarse microstructure, which can be

attributed to the increased microhardness. On the other hand, both laser power (Figure 4.17a) and powder flow rate (Figure 4.17c) have an inverse relationship with microhardness. This is affirmed by Table 4.10 which provides a summary of the responses of the S/N ratios on microhardness. Based on the S/N responses, it can be deduced that the microhardness is most significantly influenced by scanning speed, followed by laser power and then powder flow rate. This outcome can be attributed to the consolidation mechanism during the LC process. According to Zhang et al. (2008), adequate melting leads to grain refinement and microstructural enhancement responsible for promoting strong metallurgical bonds and higher

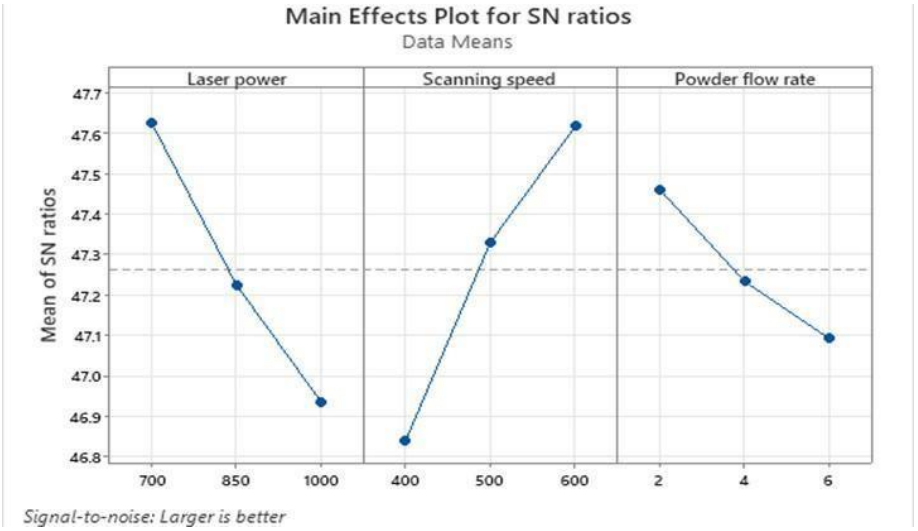

Figure 4.17: Main Effect Plot for S/N Ratios of the FGM Microhardness

Table 4.9: Response for the S/N Ratios of the FGM Microhardness

Level	Laser power	Scanning speed	Powder flow rate
1	47.62	46.84	47.46
2	47.22	47.33	47.23
3	46.94	47.62	47.09
Delta	0.69	0.78	0.37
Rank	2	1	3

Microhardness. The FGM clad/substrate interface micrographs for the samples with the highest and lowest microhardness are shown in Figure 10 for comparison. Figure 4.18 (a) confirms that sample 6, which has the highest microhardness (HV), is characterised by a dense microstructure without cracks, having a good consolidation with the substrate. This could be attributed to the laser material interaction that decreases as the scanning speed is increased, leading to an adequate melting and enhanced microstructure with good metallurgical bonding without cracks. However, sample 7 which had the lowest microhardness (HV) was characterized by poor substrate bonding, interface cracks, and larger pores.

The formation of defects is attributed to the higher laser power. When laser power is increased from 850 to 1000 W, the microhardness is significantly reduced due to the high dilution and thermal stresses when the stress level exceeds the yield limit of the

material. Additionally, when the powder flow rate increased from 4 g/min to 6 g/min, the microhardness decreased. This is because excess powder requires more power and reduced scanning time for adequate melting. When these conditions are not met, there is insufficient bonding due to incomplete melting and pore and crack defect formation, as seen in Figure 4.18b. Therefore, it can be inferred that poor consolidation and microstructural defects significantly reduced the FGM microhardness.

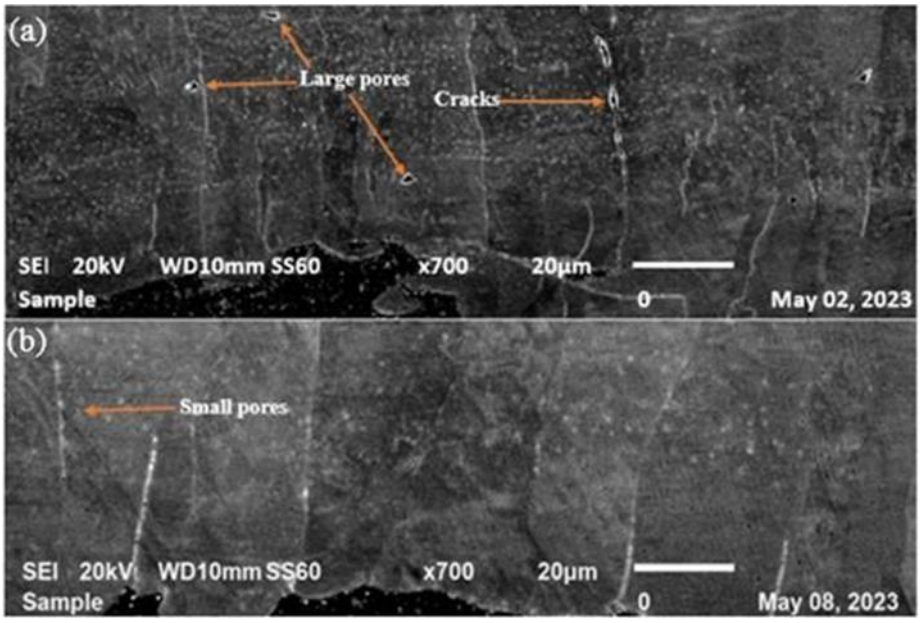

Figure 4.18: SEM Micrographs of FGM Samples with (a) Lowest Microhardness for Sample 7 (b) Highest Microhardness for Sample 6

Figure 4.19 shows the effects of process parameters interaction on microhardness. Figure 4.19 (a) was developed by varying laser power and scanning speed, while the powder flow rate was set at zero level value. It can be seen that when the scanning speed was varied between 500 to 600 mm/min, the microhardness increased above 240 HV, and when laser power was varied between 700 and 850.

When the laser power is set to zero value, the microhardness is highest at a powder flow rate of 2 g/min and the scanning speed is set to the highest value of 600 mm/min, as shown in Figure 4.19 (b). This shows that increasing the powder rate and laser power to values greater than 4.5 g/min and 900 W, respectively, reduces the microhardness to less than 210 HV, as shown in Figure 4.19 (c). Thus, it can be inferred that maximum

hardness >240 HV can be archived when scanning speed higher than 6 mm/min, laser power between 700 to 850 W, and powder flow rate less than 2 g/min.

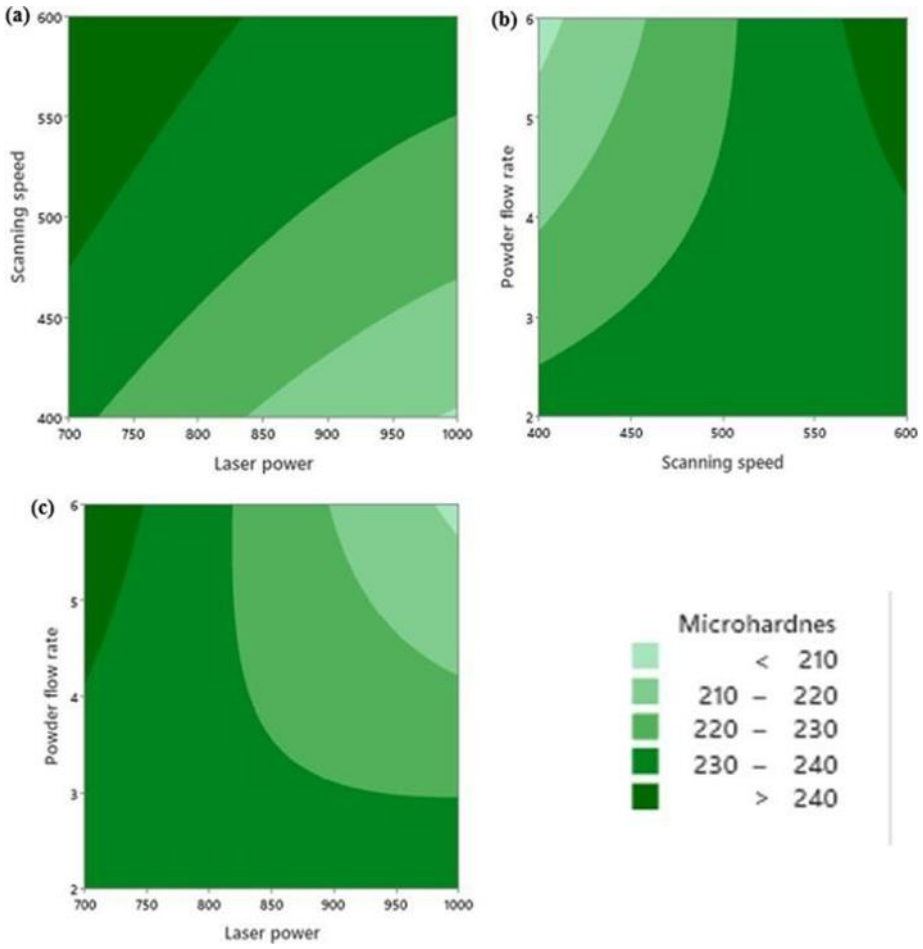

Figure 4.19: Contour Plots of the Microhardness Interaction Effects of (a) Laser Power and Scanning Speed (b) Powder Flow Rate and Scanning Speed (c) Laser Power and Powder Flow Rate

4.3.1 Effects of Process Parameters on Aspect Ratio

The main effect graphs of the process parameters on the aspect ratio (AR) are shown in Figure 4.20. The results show that as scanning speed increases, the aspect ratio gets higher. When examining the effects of increasing speed on AR, (Fatoba et al., 2021) noticed the same correlation, which they attributed to the decrease in clad height that occurs when scanning speed is increased. They argued that scanning speed affects clad height in a greater way than clad width, which increases the AR in the process. AR

increases when the molten pool increases as a result of widening clad width as the melt pool spreads. It is also clear from Figure 4.20 that the AR increases to a certain threshold, then decreases gradually due to higher powder flow that leads to excessive clad buildup.

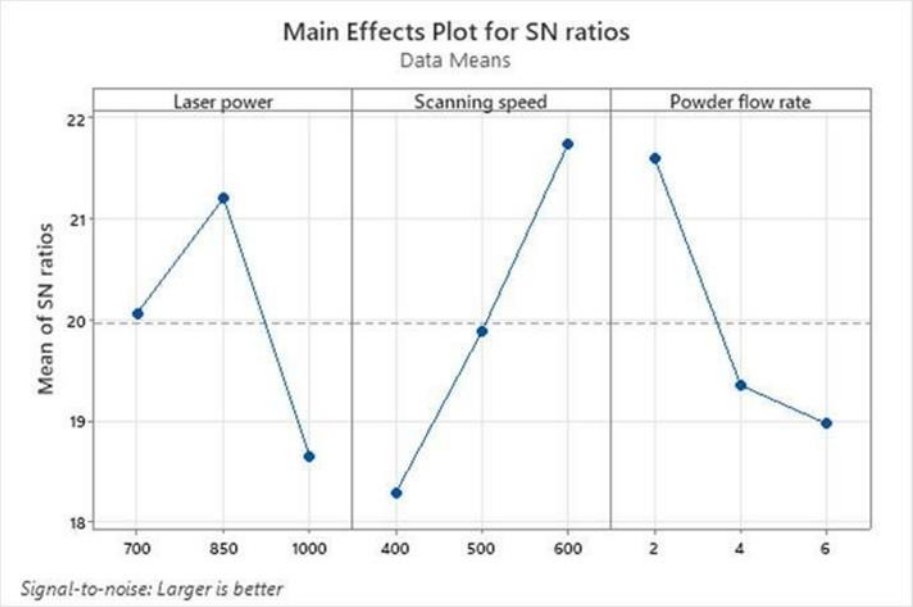

Figure 4.20: Main Effect Plot for S/N Ratios of the FGM Aspect Ratio

Table 4.10: Response Table for the S/N Ratios of the FGM Microhardness.

Level	Laser power	Scanning speed	Powder flow rate
1	20.06	18.29	21.60
2	21.20	19.88	19.35
3	18.65	21.74	18.97
Delta	2.55	3.45	2.63
Rank	3	1	2

According to Table 4.11 for the S/N responses, the parameter that most significantly influences aspect ratio is scanning speed, followed by powder flow rate, and laser power has the least significant impact. Generally, an increase in powder flow causes the clad height to increase, while reducing the clad height. This reduces the clad height and leads to a bulky layer coating. In Figure 4.21, contour plots are presented for aspect ratio interaction effects between laser power and scanning speed, powder flow rate and scanning speed, as well as powder flow rate and laser power.

It is evident from Figure 4.21 that AR is best maximized when the laser power is set at 750 to 900 mm/min. However, when laser power is set outside the region of 950 to 1000 W, the aspect ratio reduces. Generally, increasing laser power increases the AR because it reduces clad height due to the spreadability of the meltpool and widening of the clad height.

4.3.2 Effects of Process Parameter on Porosity

Figure 4.22 shows the mean effect plot of the smaller the better the FGM porosity level. An increase in laser power from 700 to 1000W and powder flow rate from 2 to 6 g/min increases the amount of porosity. Contrarywise, increasing the scanning speed from 400 to 500 mm/min reduces the porosity level until it reaches a certain threshold, then it increases porosity at a higher scanning speed reaching 6 mm/min. A study of Figure 4.23 (a,e, i) indicates that the porosity increased as laser power increased from 700 to 1000 W.

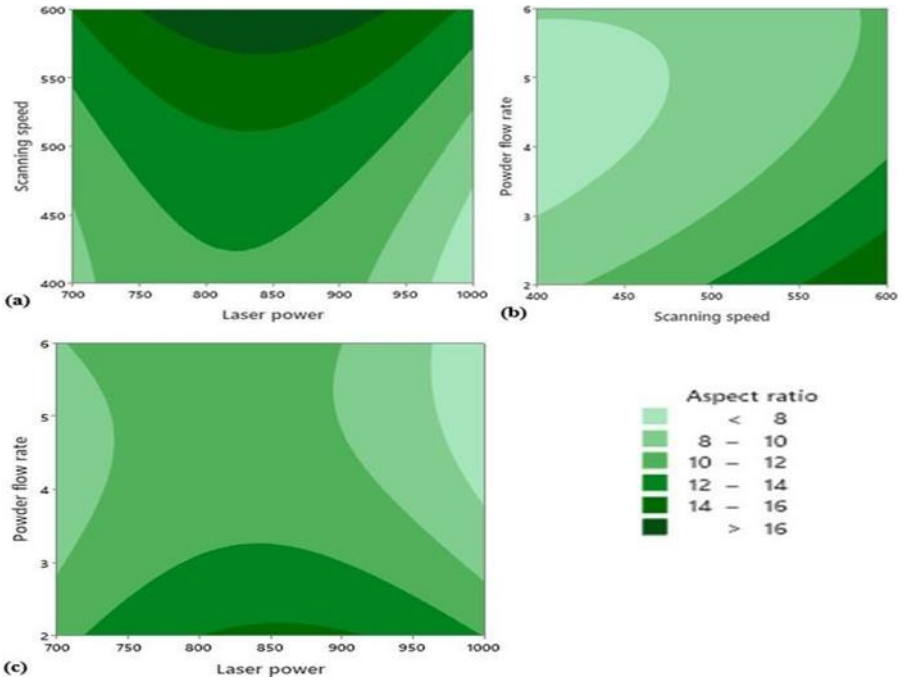

Figure 4.21: Contour Plots of the Aspect Ratio Interaction Effects of (a) Scanning Speed and Laser Power (b) Powder Flow Rate and Scanning Speed (c) Powder Flow Rate and Laser Power

This can be explained by a larger molten pool attributed to higher heat input that results in gas entrapment and causes porosity Qi et al. (2009). Figure 4.23 (a and i) shows that as powder flow rate increased from 2 to 6 g/min, the amount of porosity increased. This is because more energy input is used to melt more powder particles, resulting in some of the unmelted powder particles that leads to pore formation. It is also certain from Figure 4.23 (c and d) that an increase in scanning speed (400 to 500 mm/min) reduced the amount of porosity, but further increasing the scanning speed to 600 mm/min resulted in increased porosity, as shown in Figure 4.23 (h).

The porosity is attributed to unmelted particles because higher scanning speeds reaching 600 mm/min decrease the amount of energy input required for particle melting since it decrease the laser interaction time.

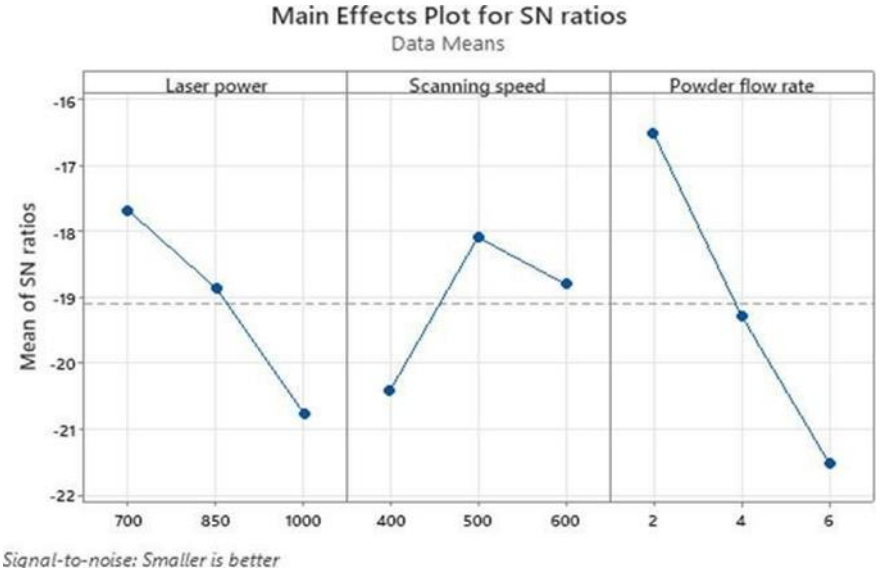

Figure 4.22: Main Effect Plot for S/N Ratios of the FGM Porosity Level

Table 4.11: Response Table for the S/N Ratios of the FGM Porosity.

Level	Laser power	Scanning speed	Powder flow rate
1	-17.67	-20.42	-16.50
2	-18.86	-18.08	-19.27
3	-20.77	-18.80	-21.52
Delta	3.09	2.33	5.02
Rank	2	3	1

Meanwhile, samples fabricated at lower scanning speeds of 400 mm/min lead to higher porosity levels because it lowers the working temperature, which leads to partial melting, leaving some interparticle porosity. Therefore, it is evident that the amount of powder fed into the system and that melted significantly influences the porosity level. Table 4.12 ascertains that powder flow rate has the most influence on FGM porosity level, followed by laser power and scanning speed, respectively. In Figure 4.24, contour plots are used to illustrate the interactions between laser power and powder flow rate, powder flow rate and scanning speed, as well as scanning speed and laser power on porosity. Two parameters were varied with the third kept at zero level.

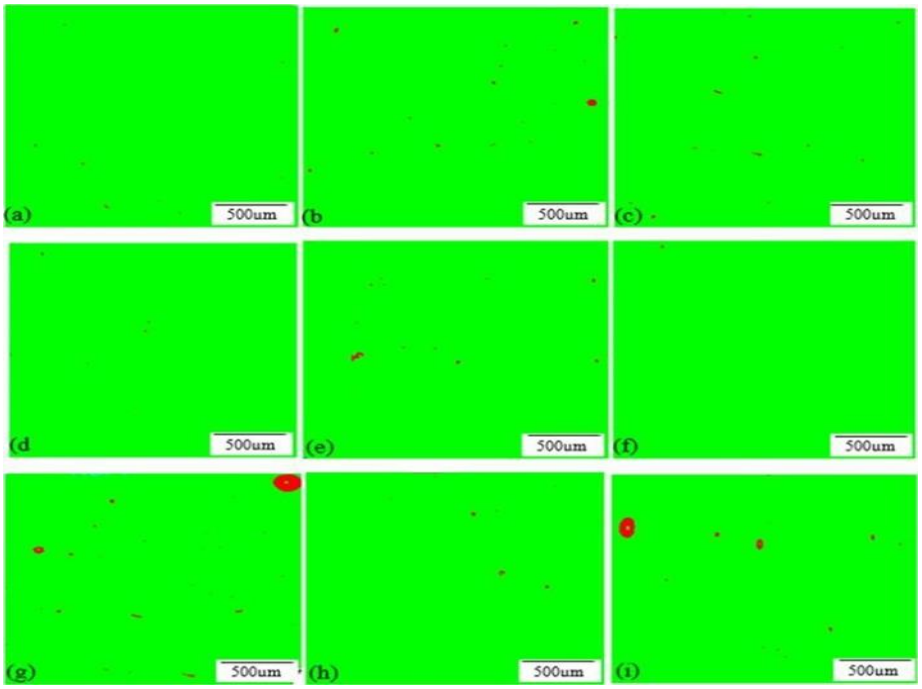

Figure 4.23: Porosity Analysis of FGM Samples As A Function Of Laser Power; (a) 700 W (e) 850 W (i) 1000 W; Scanning Speed (c) 400 mm/min (d) 500 mm/min (h) 600 mm/min, and Powder Flow Rate; (f) 2 g/min (b) 4 g/min (g) 6 g/min

A porosity level < 0.3 % is obtained when scanning speed is less than 450 mm/min and powder flow rate is more than 4 g/min. To obtain a porosity level of less than 0.15 %, the laser power must be set in the range between 750 to 850 W.

4.3.3 Effects of Process Parameters on Surface Roughness

Figure 4.25 shows the effect of process parameters on surface roughness. The surface roughness reduced as the laser power was increased up to a threshold of 850 W, then it increased with increasing laser power to 1000 W. Contrary, the surface roughness reduced with an increase in scanning speed.

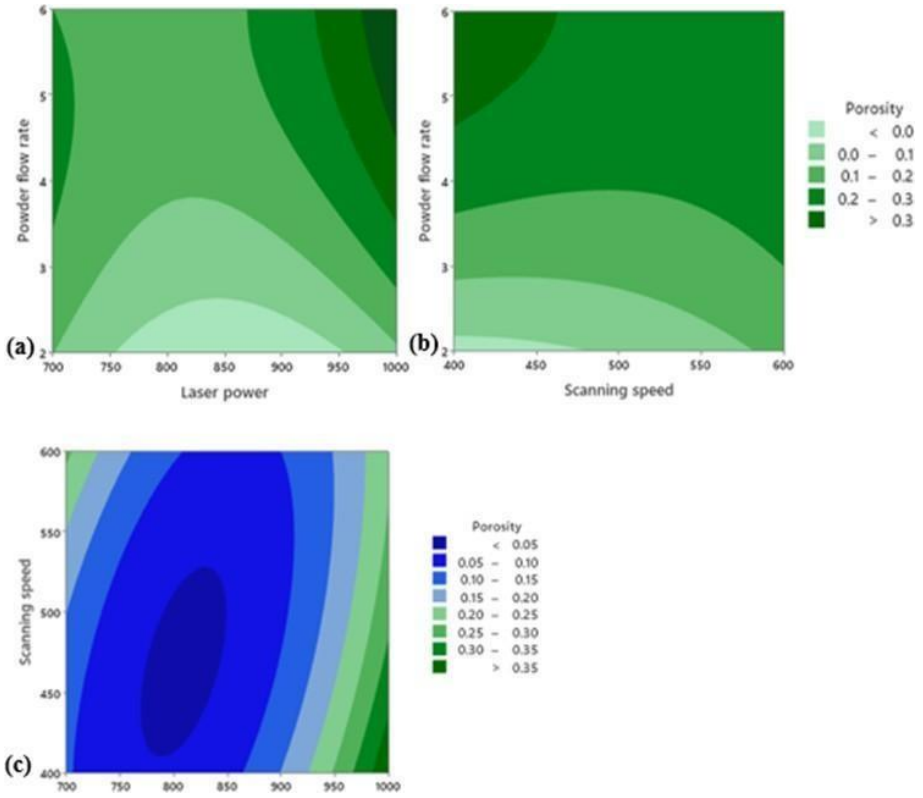

Figure 4.24: Contour Plots for the Porosity Interaction Effects of (a) Powder Flow Rate and Laser Power (b) Powder Flow Rate and Scanning Speed (c) Scanning Speed and Laser Power

Meanwhile, as the powder flow rate was increased, the surface roughness also increased. It can be seen from Table 4.13 that powder flow rate affects surface roughness the most, while laser power and scanning speed have the least influence, respectively. This is because by raising the powder flow rate, insufficient particle melting occurs. After all, the laser power was fixed, and the outcome was a rougher surface due to the unmelted particles (Ahmad, 2006). Also, a lower laser power leads to unmelted powder particles that cause a higher surface roughness (Mehrabi et al.,

2023). Fig. 18 indicates the interactive influence of two process parameters on the surface roughness whilst the other parameter is constant. The surface roughness would be <14 % when the scanning speed is >450 and laser power is between 950 and 1000 W (Figure 4.26a).

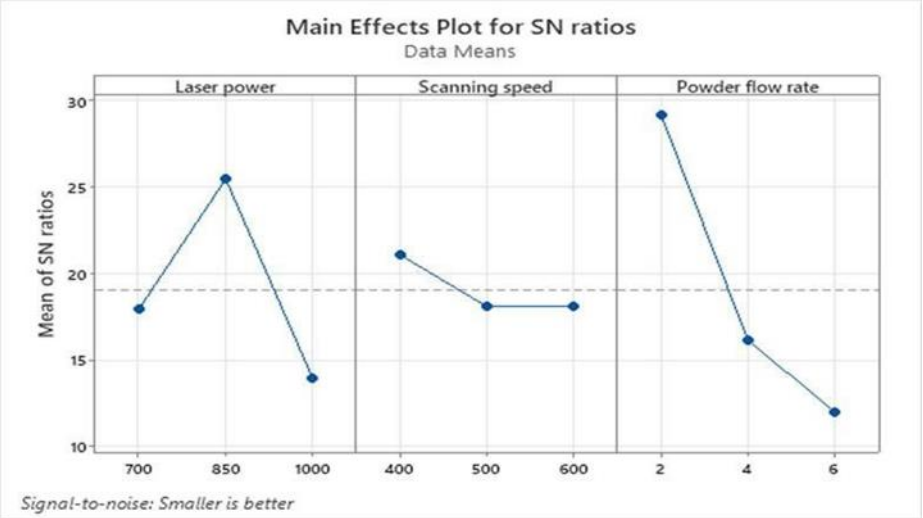

Figure 4.25: Main Effect Plot for S/N Ratios of the FGM Surface Roughness

Table 4.12: Response Table for the S/N Ratios of the FGM Surface Roughness

Level	Laser power	Scanning speed	Powder flow rate
1	17.90	21.05	29.15
2	25.43	18.07	16.09
3	13.90	18.11	11.99
Delta	11.53	2.98	17.17
Rank	2	3	1

When the powder flow rate is more than 5 g/min and the scanning speed is below 450 mm/min, the surface roughness would be >14% (Figure 4.26b). Meanwhile, a higher laser power > 950 W and a higher powder flow rate > 5 g/min, would result in a higher surface roughness > 14% (Figure 4.26c).

4.4 Confirmation and Optimization

A one-factor-at-a-time (OFAT) confirmatory experiment was carried out us- ing the well-trained network architecture as the simulating function. This was meant to the determine optimum process parameter that yields a higher GRA.

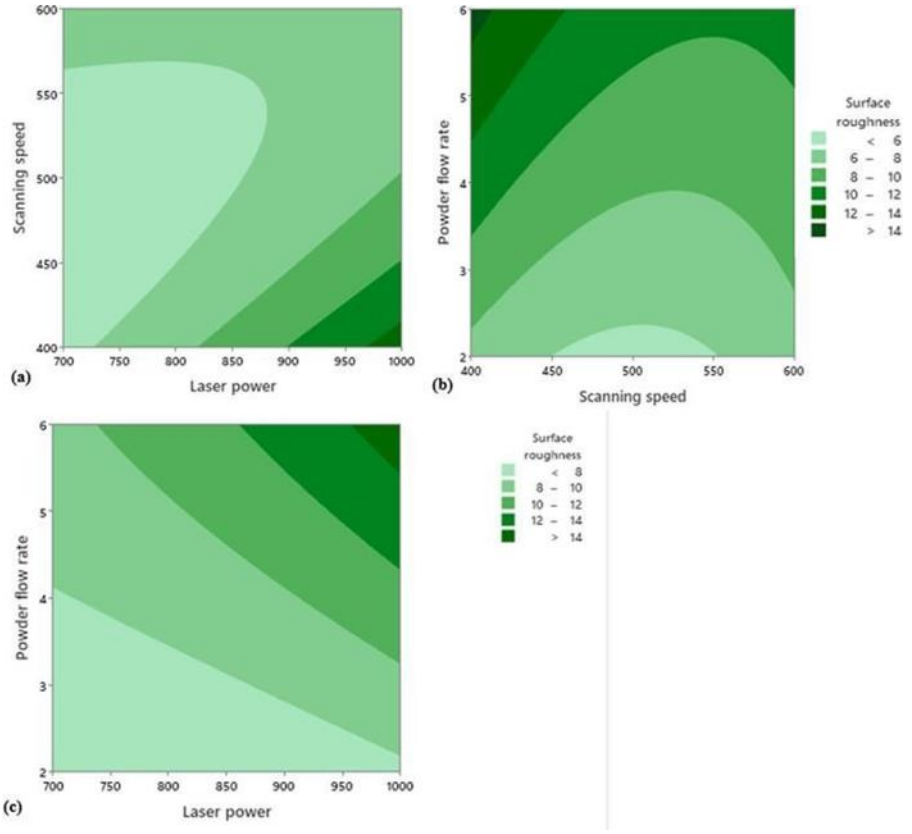

Figure 4.26: Contour Plots for the Surface Roughness Interaction Effects of (a) Scanning Speed and Laser Power (b) Powder Flow Rate and Scanning Speed (c) Powder Flow Rate and Laser Power

This is because a higher GRA indicates the clad performance characteristics exhibit a higher microhardness and aspect ratio with reduced porosity and surface roughness. The model was simulated by varying one process parameter at a time while the two others remained constant. Figure 4.27 (a) shows the optimization of laser power in the range of 300-1000 W while scanning speed and powder flow rate were kept constant at 600 mm/s and 2 g/min respectively. It can be seen that when laser power of 300-400 W is used, the GRA is at a minimum, which implies that it yields poor clad quality.

Meanwhile, a higher GRA is obtained at a laser power of 600 W, which implies it is the optimum parameter that can improve the experimental laser cladding attributes.

When the laser power is increased from 600 - 1000 W, the GRG values decrease significantly. The ANN simulated model of laser power agrees with the experimental results because the optimum experimental laser power was 850W when laser power was varied between 700-1000W, with higher laser power producing poor claddings because of higher porosity attributed to the gas entrapment. Therefore, it is evident that the ANN GRG is higher than the GRG of the Taguchi-GRA method. Similarly, the GRG was improved when the scanning speed was varied between 400-800 mm/min, as shown in Figure 4.27 (b). The highest GRG values, which indicate the optimized scanning speed parameter, were found at 700 mm/min as compared to 600 mm/min from the laser cladding experiment.

Figure 4.27 also indicates that GRG is higher at 1.5 g/min when the powder flow rate is varied between 1 – 6 g/min, while laser power and scanning speed are kept constant at 700 W and 600 mm/min, respectively (see Figure 4.27 c). This shows that the GRG can be adjusted to optimize the clad quality characteristics, as it can be seen that GRG can be improved by ANN-optimized parameters. As such, a laser cladding confirmatory experiment was carried out using the ANN-optimized parameters, and the performance attributes of the GRA optimum sample were significantly improved compared to the initial Taguchi-GRA optimum sample (see Table 4.13). Results show that the ANN-optimized parameters enhance the clad quality characteristics of the microhardness, aspect ratio, porosity, and surface roughness by 5.8%, 5.4 %, 50 %, and 4.5 %, respectively.

Table 4.13: Comparison between Taguchi Optimum Sample and ANN Optimized Sample

	Process parameter			Clad performance characteristics			
Sample	LP (W)	SP, mm/min	PF, g/min	MH, HV	AR, mm	PO, %	SR, Ra
Experimental Taguchi-GRA optimum	700	600	2.0	242.60	3.68	0.02	5.60
Predicted Taguchi-GRA	700	600	2.0	240.93	3.65	0.02	5.56
Experimental ANN optimized	600	700	1.5	257.41	3.89	0.01	5.35
Predicted ANN optimized	600	700	1.5	255.64	3.86	0.02	5.31

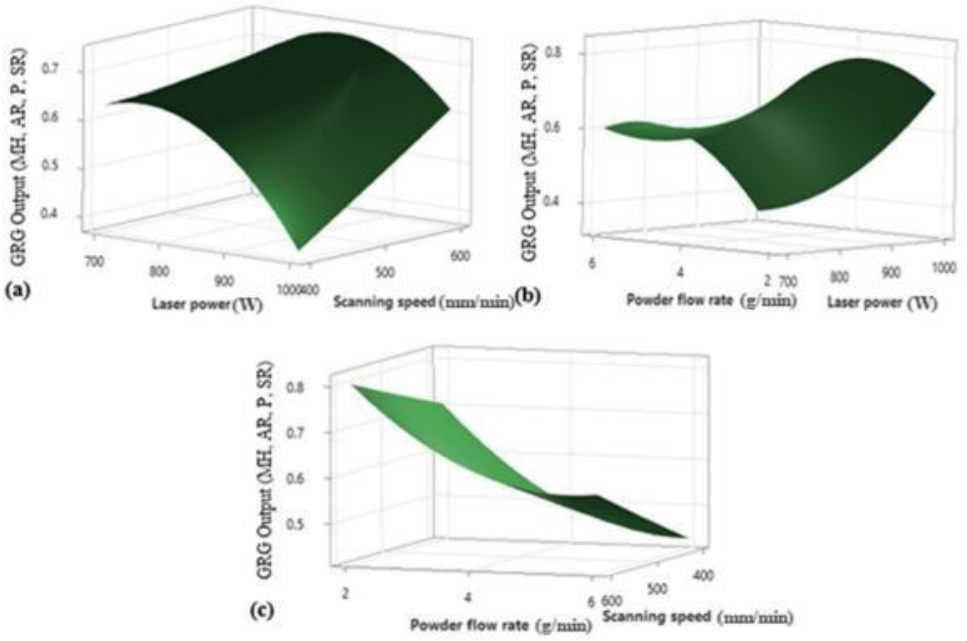

Figure 4.27: (a) Performance Improvement of GRG Values by Varying (a) Laser Power (b) Scanning Speed (c) Powder Flow Rate

The microstructural evolution of the optimum sample is shown in Figure 4.28. The five-layer clad morphologies of SS316L/IN625 FGM are shown in Figure 4.28 (a). Due to the high weight percentage of SS316L, it can be seen that the first layers primarily consist of cellular and equiaxed structures expanding along the build direction, as shown in Figure 4.28 (c) and 20 (d).

However, the grain structure changes into the columnar dendritic structure as the layer builds up with the addition of IN625 to the matrix. This structure is mostly connected to IN625 and is triggered by a low-temperature gradient with rapid solidification. Zhang et al. (2019).

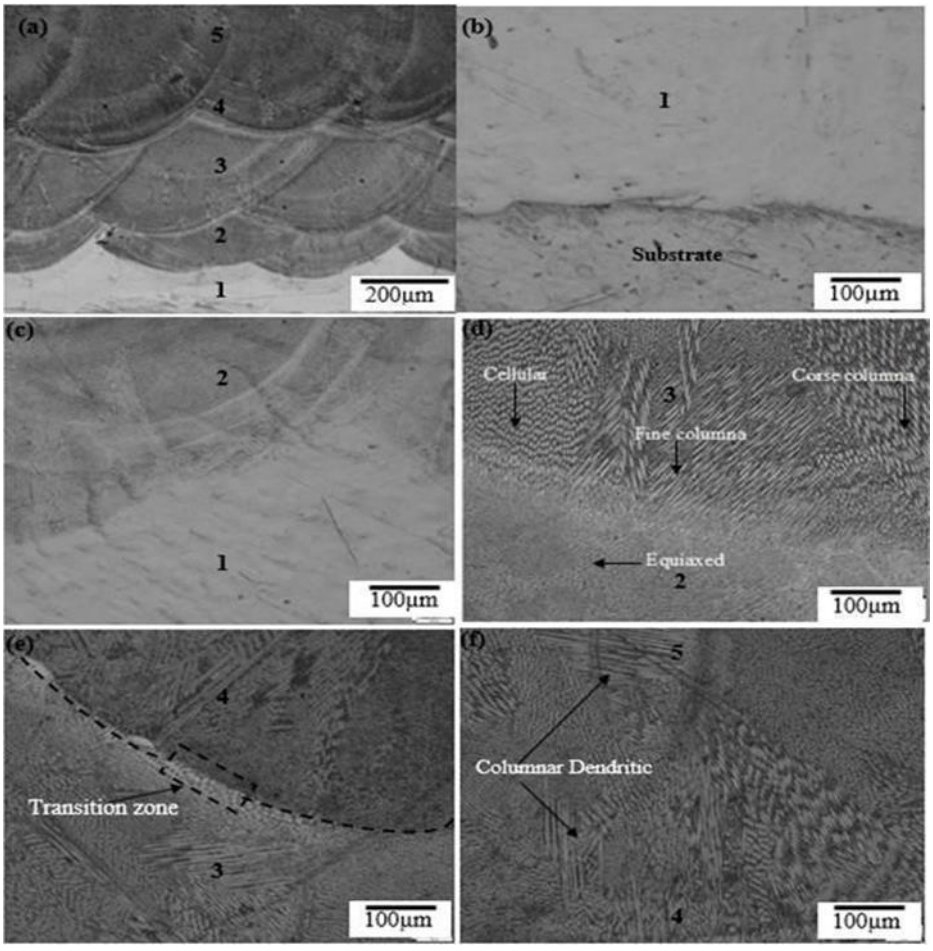

Figure 4.28: Optical Micrographs Showing Microstructural Transformation of ss316l/in625 fgm Clad (a) Microstructure of the Clad Geometry (b) Copper Substrate/100%SS316L Interface (c) Layer 1 and 2 Interfaces (d) layer 2 and 3 Interfaces (e) layer 3 and 4 Interfaces (f) Layer 4 and 5 Interface

This shows that the variation in composition of the powders influenced the grain refinement and microstructural evolution of the FGM. The Vickers hardness profile of Cu- SS316L-IN625 measured in the cross-sectional grading direction is shown in Figure 4.29. The microhardness profile reveals that the Cu substrate had the lowest microhardness (119 +/- 5 HV), which then significantly increased from SS316L (180

+/- 0) HV to the IN625 layer (245 +/- 20 HV) that had the maximum microhardness. The hardness measurements found in the manufactured FGM are comparable to those mentioned by Mehrabi et al. (2023) and Rodrigues et al. (2019).

The increased content of laves phases and γ-dendrite in the interdendritic area promoted the solid solution strengthening of IN625, resulting in higher microhardness values (see Figure 4.30). When functionally grading SS316L- IN625 using the LMD technique, Mehrabi et al. (2023) observed the same matrix and linked the laves phases and γ-matrix to the microhardness values.

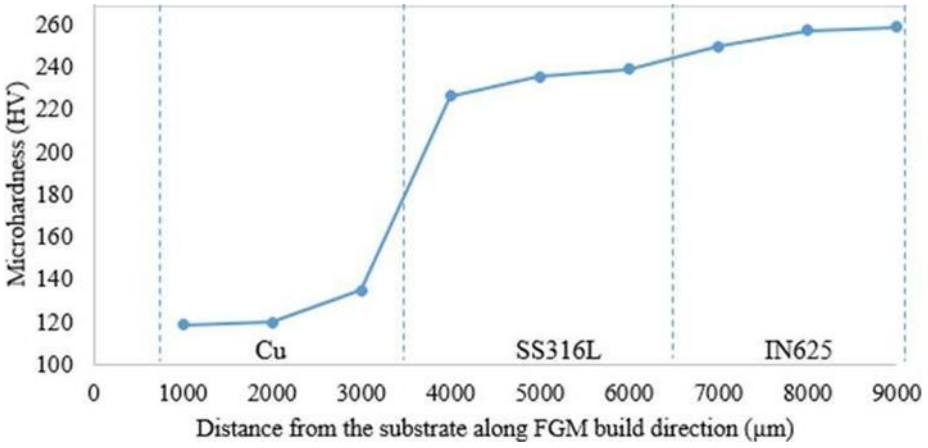

Figure 4.29: Vickers Microhardness Profile of Cu Substrate and SS316L/ IN625 FGM along the Clad Build Direction

Figure 4.31 shows the EDS analysis at the interface of the substrate and coating, which indicates the diffusion of chromium, iron, silicon, sulfur, and nickel elements to the copper substrate. This demonstrates that good metallurgical bonding with minimum dilution can be achieved when depositing at optimum processing parameters due to the adequate melting and diffusion of essential elements during laser-material interaction. The presence of Cr and Ni elements in the microstructure is preferred for better corrosion resistance of the copper substrate and FGM when operating in hostile conditions since they form a protective passive film. Minimum dilution is also preferred for coatings to enhance tribological properties and prevent customer rejection (Olakanmi et al., 2019a).

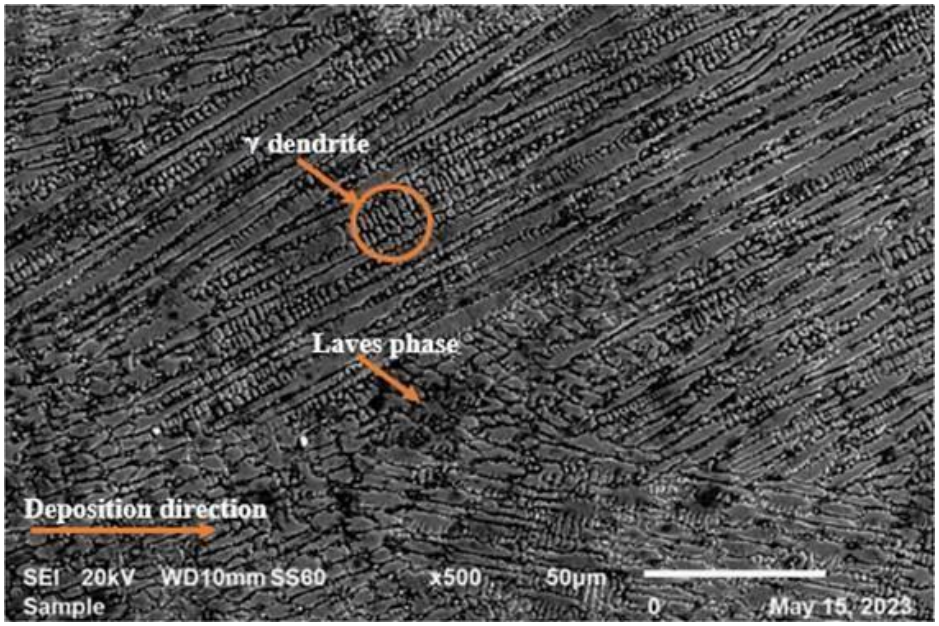

Figure 4.30: SEM Micrograph of the FGM Microstructure at 50-50 wt% of SS316L/IN625

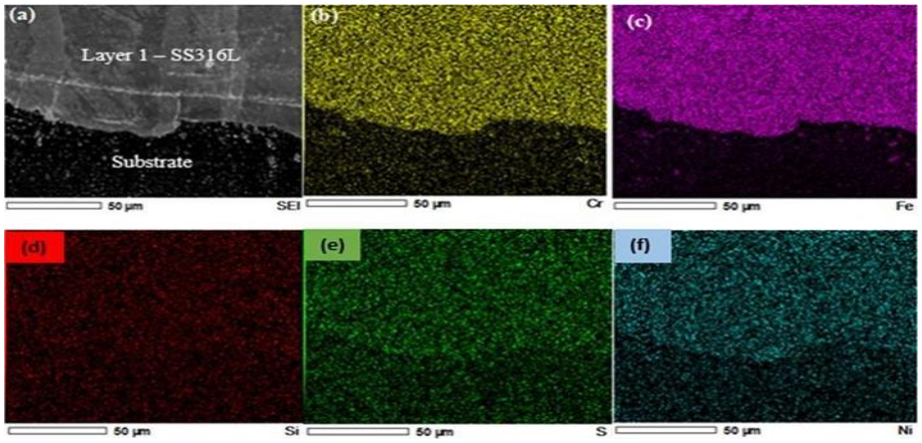

Figure 4.31: The SEM-EDS Mapping of the Cu-SS316L Dilution Zone (a) Substrate/Coating Interface, and Diffusion of (b) Cr (c) Fe Si (e) S (f) Ni

Tensile residual stresses that result in defects like pores and cracks that impair mechanical properties can be lessened with normalizing and annealing heat treatment post-processing. Figure 4.32 displays the residual stress readings for theheat-treated FGM, as-built coating, and pure copper substrate before deposition, to understand how material variation affects stress distribution. The residual stress values were auto-generated by the residual stress machine.

Figure 4.32 (a) illustrates the findings, which demonstrate the stress distribution for pure copper that had compressive residual stresses of (–ve 2692 MPa) that are acceptable for produced components. A homogeneous stress distribution can be seen by less distortion, an equilibrium debye ring, and a uniform stress profile on the substrate before deposition. The substrate and coating suffer expansion during the laser material's interaction due to cooling and contraction, which results in tensile residual stresses (+ve 8 MPa) that distort the material after laser cladding Sadeh et al. (2023). This tensile RS can cause catastrophic failure of heat exchanger components through stress corrosion cracking due to high-stress peaks highlighted in red, see Figure 4.32 (b).

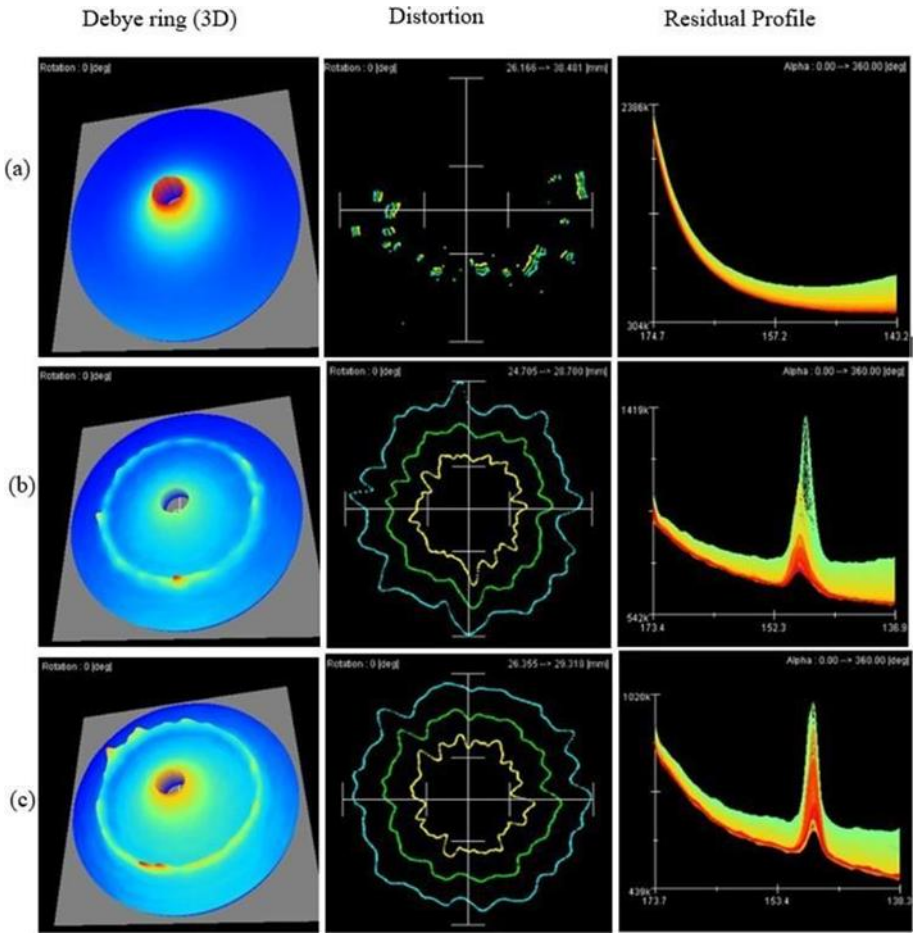

Figure 4.32: Residual Stress Measurements of SS316L/IN625 FGM (a) Pure Copper Substrate (b) As-Built SS316L/IN625 FGM and (c) Heat- Treated Cladding

4.5 Chapter Summary

In summary, it is evident that the heat exchanger tubes suffered failure aggravated by three hostile conditions (excessive operating temperatures, high fluid pressure, and wet hydrogen sulfide corrosive media). In addition, laser cladding results showed that it is possible to deposit SS316L/IN625 FGM coating on pure copper substrate and still have a good consolidated structure at the interface. The clad attributes such as hardness and surface finish were also enhanced by the optimization approach employed, which coupled the Taguchi-GRA with the ANN method. Thus, it can be inferred that the developed coating can be successfully employed during surface modification.

CHAPTER FIVE

CONCLUSIONS AND RECOMMENDATIONS

5.1 Conclusions

The objectives of this study to understand the failure mechanism, as well as to develop and optimize the laser cladded SS316L/IN625 functionally graded material were met and the following are the conclusions reached;

- The heat exchanger tubes failed due to hydrogen embrittlement.
- SS316L/IN625 functionally graded material was developed using a laser cladding process.
- Hydrid optimization combining Taguchi-grey relational analysis and artificial neural network enhanced the clad quality characteristics.
- Scanning speed has the most significant influence on the SS316L/IN625 FGM clad performance characteristics, while powder flow rate and laser power have minimal effect.
- The optimal process parameters are laser power, scanning speed, and powder flow rate of 600 W, 700 mm/min, and 1.5 g/min, respectively.
- The SS36L/IN625 FGM comprises mostly of equiaxed structure that varied sharply to columnar grains as the layer build-up increased, due to high thermal gradient.

5.2 Recommendations

- This study recommends the following for future considerations:
- heat exchanger corrosion resistance and wear properties of the developed SS316L/IN625 coating must be investigated in future for deposition made on pure copper substrate.
- The heat transfer properties of the developed coating should be investigated further to understand the performance during service.

- A suitable manufacturing technique must be identified in future research, which is capable of producing boiler tubes with the developed coating on a suitable pipe size.
- The influence of laser-clad track overlapping can be investigated in future to enhance the clad quality characteristics.

REFERENCES

Addepalli, S., Eiroa, D., Lieotrakool, S., Fran¸cois, A.-L., Guisset, J., San- jaime, D., Kazarian, M., Duda, J., Roy, R., & Phillips, P. (2015). Degra- dation study of heat exchangers. *Procedia Cirp*, 38:137–142.

Ahmad, Z. (2006*). Principles of corrosion engineering and corrosion control*. Elsevier.

Albanakis, C., Yakinthos, K., Kritikos, K., Missirlis, D., Goulas, A., & Storm, P. (2009). The effect of heat transfer on the pressure drop through a heat exchanger for aero engine applications. *Applied Thermal Engineering*, 29(4):634–644.

Balu, P., Rea, E., & Deng, J. (2015). Laser cladding of nickel-based alloy coatings on copper substrates. In *Industrial Laser Applications Symposium (ILAS 2015)*, volume 9657, pp. 8–17. SPIE.

Bartkowski, D., Bartkowska, A., Piasecki, A., & Jurˇci, P. (2020). Influence of laser cladding parameters on microstructure, microhardness, chemical composition, wear and corrosion resistance of Fe–B composite coatings re- inforced with B4C and Si particles. *Coatings*, *10*(9):809.

Belsvik, M. A., Tucho, W. M., & Hansen, V. (2020). Microstructural studies of direct- laser-deposited stainless steel 316L-Si on 316L base material. *SN Applied Sciences*, 2:1–15.

Ben-Artzy, A., Reichardt, A., Borgonia, J.-P., Dillon, R., McEnerney, B., Shapiro, A., & Hosemann, P. (2021). Compositionally graded SS316 to C300 Maraging steel using additive manufacturing. *Materials & Design*, 201, 109500.

Bichkar, P., Dandgaval, O., Dalvi, P., Godase, R., & Dey, T. (2018). Study of shell and tube heat exchanger with the effect of types of baffles. *Procedia Manufacturing*, *20*, 195–200.

Buldum, B., E¸sme, U., Kemal Ku¨lekci, M., S¸ik, A., & Kazan¸co˘glu, Y. (2012). Use of Grey-Taguchi method for the optimization of oblique turning process of AZ91D magnesium alloy. *Materials Testing*, *54*(11-12), 779–785.

Carroll, B. E., Otis, R. A., Borgonia, J. P., Suh, J.-o., Dillon, R. P., Shapiro, A. A., …& Beese, A. M. (2016). Functionally graded material of 304L stainless steel and inconel 625 fabricated by di- rected energy deposition: Characterization and thermodynamic modeling. *Acta Materialia*, *108*, 46–54.

Chae, H., Wang, H., Hong, M., Kim, W. C., Kim, J.-G., Kim, H., & Lee, S. Y. (2020). Stress corrosion cracking of a copper pipe in a heating water supply system. *Metals and Materials International*, *26*, 989–997.

Chan, Y. H., Lock, S. S. M., Wong, M. K., Yiin, C. L., Loy, A. C. M., Cheah, K. W.,… & Chin, B. L. F., (2022). A state-of-the-art review on capture and separation of hazardous hydrogen sulfide (H2S): Recent advances, challenges and outlook. *Environmental Pollution*, 120219.

Chandra, K., Kain, V., Shetty, P., & Kishan, R. (2014). Failure analysis of copper tube used in a refrigerating plant. *Engineering Failure Analysis*, *37*, 1– 11.

Chen, Q., Finney, K., Li, H., Zhang, X., Zhou, J., Sharifi, V., & Swith- enbank, J. (2012). Condensing boiler applications in the process industry. *Applied Energy*, *89*(1), 30–36.

Cheng, Y.-h., Cui, R., Wang, H.-z., & Han, Z.-t. (2018). Effect of processing parameters of laser on microstructure and properties of cladding 42crmo steel. *The International Journal of Advanced Manufacturing Technology*, *96*, 1715– 1724.

Corbin, D. J., Nassar, A. R., Reutzel, E. W., Beese, A. M., & Michaleris, P. (2018). Effect of Substrate thickness and preheating on the distortion of laser deposited Ti–6Al–4V. *Journal of Manufacturing Science and En- gineering*, *140*(6), 061009.

Corleto, C. R. & Argade, G. R. (2017). Failure analysis of dissimilar weld in heat exchanger. *Case studies in engineering failure analysis*, *9*, 27–34.

Corte, J., Rebello, J., Areiza, M., Tavares, S., & Araujo, M. (2015). Failure analysis of AISI 321 tubes of heat exchanger. *Engineering Failure Analysis*, *56*, 170–176.

CPM, S. A., Varghese, B., & Baby, A. (2014). A review on functionally graded materials. *Int. J. Eng. Sci*, *3*, 90–101.

Cuevas-Arteaga, C., Verhelst, D., & Alfantazi, A. (2010). Performance of alloy 625 under combustion gas environments: a review. *ECS Transactions*, *28*(24), 61.

Deng, Z., Chen, T., Wang, H., Li, S., & Liu, D. (2020). Process param- eter optimization when preparing Ti (C, N) ceramic coatings using laser cladding based on a neural network and quantum-behaved particle swarm optimization algorithm. *Applied Sciences*, 10(18), 6331.

Dhaiveegan, P., Elangovan, N., Nishimura, T., & Rajendran, N. (2016). Corrosion behavior of 316L and 304 stainless steels exposed to industrial- marine-urban environment: field study. *Rsc Advances*, *6*(53), 47314–47324.

El-Wazery, M. & El-Desouky, A. (2015). A review on functionally graded ceramic-metal materials. *Journal of Materials and Environmental Science*, *6*(5), 1369–1376.

Faes, W., Lecompte, S., Ahmed, Z. Y., Van Bael, J., Salenbien, R., Verbeken, K., & De Paepe, M. (2019). Corrosion and corrosion prevention in heat exchangers. *Corrosion reviews*, *37*(2), 131–155.

Fatoba, O., Naidoo, L., Akinlabi, S., Akinlabi, E., Mwema, F., & Ikuma- Payi, O. (2021). Dilution and aspect ratio properties on performance of laser deposited ti-al-si-cu/ti-6al-4v composite coatings. In *IOP Conference Series:*

Materials Science and Engineering, volume 1107, page 012123. IOP Publishing.

Ferreira, A. A., Amaral, R. L., Romio, P. C., Cruz, J. M., Reis, A. R., & Vieira, M. F. (2021). Deposition of nickel-based superalloy claddings on low alloy structural steel by direct laser deposition. *Metals*, *11*(8), 1326.

Franco, A. & Vaccaro, M. (2017). Recent trends in the development of heat exchangers for geothermal systems. In *Journal of Physics: Conference Series*, volume 923, page 012044. IOP Publishing.

Ghanavati, R. & Naffakh-Moosavy, H. (2021). Additive manufacturing of functionally graded metallic materials: A review of experimental and nu- merical studies. *Journal of Materials Research and Technology*, *13*, 1628– 1664.

Goodarzi, D. M., Pekkarinen, J., & Salminen, A. (2017). Analysis of laser cladding process parameter influence on the clad bead geometry. *Welding in the World*, *61*, 883–891.

Hamatani, H., Shimoda, N., & Kitaguchi, S. (2003). Effect of the composi- tion profile and density of lpps sprayed functionally graded coating on the thermal shock resistance. *Science and Technology of Advanced Materials*, *4*(2), 197–203.

Hotz, H., Zimmermann, M., Greco, S., Kirsch, B., & Aurich, J. C. (2021). Additive manufacturing of functionally graded ti-al structures by laser-based direct energy deposition. *Journal of Manufacturing Processes*, *68*, 1524–1534.

Hruska, J., Mlnarik, J., & Cizner, J. (2022). High-temperature corrosion of nickel-based coatings for biomass boilers in chlorine-containing atmosphere. *Coatings*, *12*(2), 116.

Hussain, T., Dudziak, T., Simms, N., & Nicholls, J. (2013). Fireside corrosion behavior of HVOF and plasma-sprayed coatings in advanced coal/biomass co- fired power plants. *Journal of thermal spray technology*, 22, 797–807.

Imran, M. (2014). Effect of corrosion on heat transfer through boiler tube and estimating overheating. *International Journal of Advanced Mechanical Engineering*, *4*(6), 629–638.

Ishii, M., Kaneko, M., & Oda, T. (2002). Titanium and its alloys as key materials for corrosion protection engineering. *Shinnittetsu Giho*, 45–50.

Islam, M. (2019). El-galy, bassiouny i. Saleh, Mahmoud H. Ahmed, Function- ally graded materials classifications and development trends from industrial point of view, *SN Applied Sciences* , 2523–3963.

Jendrzejewski, R., Navas, C., Conde, A., de Damborenea, J. J.,& S´liwin´ski, G. (2008). Properties of laser-cladded stellite coatings prepared on pre- heated chromium steel. *Materials & Design*, *29*(1), 187–192.

Jiang, Q., Zhang, P., Yu, Z., Shi, H., Wu, D., Yan, H., Ye, X., ..& Tian, Y. (2021). A review on additive manufacturing of pure copper. *Coatings*, *11*(6), 740.

Jim´enez, A., Bidare, P., Hassanin, H., Tarlochan, F., Dimov, S., & Essa, K. (2021). Powder-based laser hybrid additive manufacturing of metals: A review. *The International Journal of Advanced Manufacturing Technology*, *114*, 63–96.

Jin, H.-Z., Gu, Y., & Ou, G.-F. (2021). Corrosion risk analysis of tube- and-shell heat exchangers and design of outlet temperature control system. *Petroleum Science*, 18(4), 1219–1229.

Jing, Z., Cao, Q., & Jun, H. (2021). Corrosion, wear and biocompatibility of hydroxyapatite bio-functionally graded coating on titanium alloy surface prepared by laser cladding. *Ceramics International*, *47*(17), 24641–24651.

Johnson, N., Vulimiri, P., To, A., Zhang, X., Brice, C., Kappes, B., & Steb- ner, A. (2020). Invited review: Machine learning for materials developments in metals additive manufacturing. *Additive Manufacturing*, *36*, 101641.

Kant, S. (2017). Application of taguchi oa array and artificial neural network for optimizing and modeling of drilling cutting parameters. *International Journal of Theoretical and Applied Mechanics*, *12*(1), 1–2.

Kapranos, P. & Priestner, R. (1987). Overview of metallic materials for heat exchangers for ocean thermal energy conversion systems. *Journal of materials science*, *22*, 1141–1149.

Klein, U., Zunkel, A., & Eberle, A. (2014). Breakdown of heat exchangers due to erosion corrosion and fretting caused by inappropriate operating conditions. *Engineering Failure Analysis*, *43*, 271–280.

Kracke, A. & Allvac, A. (2010). Superalloys, the most successful alloy system of modern times-past, present and future. In *Proceedings of the 7th International Symposium on Superalloy*, volume 718, pp. 13–50.

Kumar, D., Gupta, A. K., Chandna, P., & Pal, M. (2015). Optimiza- tion of neural network parameters using Grey–Taguchi methodology for manufacturing process applications. *Proceedings of the Institution of Me- chanical Engineers, Part C: Journal of Mechanical Engineering Science*, 229(14), 2651–2664.

Kumar, S., Choudhary, A. K. S., Anwar, J., & Sharma, V. (2016). Opti- mization of process parameters in Direct Metal Deposition Technique us- ing Taguchi method. *International Journal of Mechanical Engineering and Technology*, *7*(3).

Ku´znicka, B. (2009). Erosion–corrosion of heat exchanger tubes. *Engineering Failure Analysis*, 16(7), 2382–2387.

Lazi´c, V., Arsi´c, D., Nikoli´c, R. R., Raki´c, D., Aleksandrovi´c, S., Djordjevi´c, M., & Hadzima, B. (2016). Selection and analysis of material for boiler pipes in a steam plant. *Procedia Engineering*, *149*, 216–223.

Le, T.-N. & Lo, Y.-L. (2019). Effects of sulfur concentration and marangoni convection on melt-pool formation in transition mode of selective laser melt- ing process. *Materials & Design*, *179*, 107866.

Li, K., Wang, X., & Xiong, W. (2022). Functionally graded material fabri- cated by powder-based laser directed energy deposition: From conventional to complex concentrated alloys.

Lian, G., Zhang, H., Zhang, Y., Tanaka, M. L., Chen, C.,& Jiang, J. (2019). Optimizing processing parameters for multi-track laser cladding utilizing multi- response grey relational analysis. *Coatings*, 9(6), 356.

Lima, A. S., Nascimento, A. M. d., Abreu, H. F. G. d., & de Lima-Neto, P. (2005). Sensitization evaluation of the austenitic stainless steel AISI 304L, 316L, 321 and 347. *Journal of Materials Science*, *40*, 139–144.

Lin, H.-L. (2012). The use of the taguchi method with grey relational analysis and a neural network to optimize a novel gma welding process. *Journal of intelligent manufacturing*, *23*(5), 1671–1680.

Liu, Y., Ding, Y., Yang, L., Sun, R., Zhang, T., & Yang, X. (2021). Research and progress of laser cladding on engineering alloys: A review. *Journal of Manufacturing Processes*, *66*, 341–363.

Liu, Y., Xu, T., & Li, G. (2022). Research on Wear and Corrosion Resistance of Ni60-WC Coating Fabricated by Laser on the Preheated Copper Alloy. *Coatings*, *12*(10), 1537.

Luo, K., Li, S., Xu, G., Hosseini, S. R. E., & Lu, J. (2022). Hot corrosion behaviors of directed energy deposited Inconel 718/Haynes 25 functionally graded material at 700 C and 900 C. *Corrosion Science*, *197*, 110040.

Lv, J., Zhang, C., Chen, Z., Bai, D., Zhang, Y., Li, G., & Lu, X. (2021). Fabrication and characterization of Ni60A alloy coating on copper pipe by plasma cladding with induction heating. *Coatings*, *11*(9), 1080.

Mahamood, R. & Akinlabi, E. T. (2015). Laser metal deposition of func- tionally graded Ti6Al4V/TiC. *Materials & Design*, 84, 402–410.

Mahamood, R. M., Akinlabi, E. T., Shukla, M., & Pityana, S. L. (2012). Functionally graded material: an overview.

Mahamood, R. M., Akinlabi, E. T., Shukla, M., & Pityana, S. L. (2013). Laser metal deposition of ti6al4v: a study on the effect of laser power on microstructure and microhardness.

Mahmood, M., Suryanto, S., Al Hazza, M., & Haidera, F. (2018). De- veloping of corrosion resistance nano copper oxide coating on copper us- ing anodization in oxalate solution. *International Journal of Engineering*, *31*(3), 450–455.

Maodzeka, D. K., Olakanmi, E. O., Mosalagae, M., Hagedorn-Hansen, D., & Pityana, S. L. (2023). Hybrid optimisation studies on the microstructural properties and wear resistance of maraging steel 1.2709 parts produced by laser powder bed fusion. *Optics & Laser Technology*, *159*, 108914.

Marrey, M., Malekipour, E., El-Mounayri, H., & Faierson, E. J. (2019). A framework for optimizing process parameters in powder bed fusion (PBF) process using artificial neural network (ANN). *Procedia Manufacturing*, *34*, 505–515.

Master, B. I., Chunangad, K. S., Boxma, A., Kral, D., & Stehlik, P. (2006). Most frequently used heat exchangers from pioneering research to worldwide applications. *Heat Transfer Engineering*, *27*(6), 4–11.

McDonald, A. G. & Magande, H. (2012). *Introduction to thermo-fluids systems design*. John Wiley & Sons.

Mehrabi, O., Seyedkashi, S. M. H., & Moradi, M. (2023). Function- ally Graded Additive Manufacturing of Thin-Walled 316L Stainless Steel- Inconel 625 by Direct Laser Metal Deposition Process: Characterization and Evaluation. *Metals*, *13*(6), 1108.

Meng, W., Zhang, W., Zhang, W., Yin, X., & Cui, B. (2020). Fabrication of steel-inconel functionally graded materials by laser melting deposition integrating with laser synchronous preheating. *Optics & Laser Technology*, 131, 106451.

Meng, W., Zhang, W., Zhang, W., Yin, X., Guo, L., & Cui, B. (2019). Addi- tive fabrication of 316L/Inconel625/Ti6Al4V functionally graded materials by laser synchronous preheating. *The International Journal of Advanced Manufacturing Technology*, *104*. 2525–2538.

Miteva, A. (2014). An overview of the functionally graded materials. *Ma-chines.*Technologies. Materials., *8*(3), 13–16.

Miyamoto, H., Saburi, D., & Fujiwara, H. (2012). A microstructural as- pect of intergranular stress corrosion cracking of semi-hard u-bend tubes of commercially pure copper in cooling systems. *Engineering Failure Analysis*, 26, 108–119.

Mondal, S., Tudu, B., Bandyopadhhyay, A., & Pal, P. K. (2012). Process optimization for laser cladding operation of alloy steel using genetic algo- rithm and artificial neural network. *International Journal of Computational Engineering Research*, 2(1), 18–24.

Mousavian, R. T., Hajjari, E., Ghasemi, D., Manesh, M. K., & Ranjbar, K. (2011). Failure analysis of a shell and tube oil cooler. *Engineering Failure Analysis*, 18(1), 202–211.

Nguejio, J., Szmytka, F., Hallais, S., Tanguy, A., Nardone, S., & Martinez, M. G. (2019). Comparison of microstructure features and mechanical prop- erties for additive manufactured and wrought nickel alloys 625. *Materials Science and Engineering: A*, *764*, 138214.

Nukman, Y., Hassan, M., and Harizam, M. (2013). Optimization of prediction error in co2 laser cutting process by taguchi artificial neural network hy- brid with

genetic algorithm. *Applied Mathematics & Information Sciences*, *7*(1), 363–370.

Nyadongo, S. T., Pityana, S. L., & Olakanmi, E. O. (2021). Isothermal oxi- dation performance of laser cladding assisted with preheat (LCAP) Tribaloy T-800 composite coatings deposited on EN8. *Coatings*, *11*(7), 843.

Ocylok, S., Weisheit, A., & Kelbassa, I. (2010). Functionally graded multi- layers by laser cladding for increased wear and corrosion protection. *Physics Procedia*, *5*, 359–367.

Oksa, M., Auerkari, P., Salonen, J., & Varis, T. (2014). Nickel-based hvof coatings promoting high temperature corrosion resistance of biomass-fired power plant boilers. *Fuel processing technology*, *125*, 236–245.

Olakanmi, E., Nyadongo, S., Malikongwa, K., Lawal, S. A., Botes, A., & Pityana, S. L. (2019a). Multi-variable optimisation of the quality charac- teristics of fiber-laser cladded inconel-625 composite coatings. *Surface and Coatings Technology*, *357*, 289–303.

Olakanmi, E., Sepako, M., Morake, J., Hoosain, S. E., & Pityana, S. L. (2019b). Microstructural characteristics, crack frequency and diffusion ki- netics of functionally graded ti-al composite coatings: Effects of laser energy density (led). *Jom*, *71*(3), 900–911.

Ostolaza, M., Arrizubieta, J. I., Lamikiz, A., & Cortina, M. (2021). Func- tionally graded aisi 316l and aisi h13 manufactured by l-ded for die and mould applications. *Applied Sciences*, *11*(2), 771.

Pan, L. K., Wang, C. C., Wei, S. L., & Sher, H. F. (2007). Optimizing multiple quality characteristics via Taguchi method-based Grey analysis. *Journal of Materials Processing Technology*, *182*(1-3), 107–116.

Pan, T., Zhang, X., Yamazaki, T., Sutton, A., Cui, W., Li, L., & Liou, F. (2020).Characteristics of inconel 625—copper bimetallic structure

fabricated by directed energy deposition. *The International Journal of Advanced Manufacturing Technology*, *109*, 1261–1274.

Parisher, R. A. (2001). *Pipe drafting and design*. Elsevier.

Patel, S. K. & Mavani, A. M. (2012). Shell and tube heat exchanger thermal design with optimization of mass flow rate and baffle spacing. *International Journal of advanced engineering research and studies*, *2*(1), 130–135.

Permatasari, R. & Yusuf, A. M. (2018). Material selection for shell and tube heat exchanger using computational fluid dynamics method. In *AIP Conference Proceedings*, volume 1977. AIP Publishing.

Pokhmurskii, V., Student, M., Gvozdeckii, V., Stypnutskyy, T., Student, O., Wielage, B., & Pokhmurska, H. (2013). Arc-sprayed iron-based coatings for erosion-corrosion protection of boiler tubes at elevated temperatures. *Journal of thermal spray technology*, *22*, 808–819.

Polat, A., Sarikaya, O., & Celik, E. (2002). Effects of porosity on thermal loadings of functionally graded Y2O3–ZrO2/NiCoCrAlY coatings. *Materi- als & design*, *23*(7), 641–644.

Qi, H., Azer, M., & Ritter, A. (2009). Studies of standard heat treatment ef- fects on microstructure and mechanical properties of laser net shape manu- factured inconel 718. *Metallurgical and Materials Transactions A*, *40*, 2410– 2422.

Ralls, A. M., Kumar, P., & Menezes, P. L. (2020). Tribological proper- ties of additive manufactured materials for energy applications: a review. *Processes*, 9(1, 31.

Rebak, R. (2011). Stress corrosion cracking (scc) of nickel-based alloys. In *Stress corrosion cracking*, pages 273–306. Elsevier.

Reeks, W., Davies, H., & Marchisio, S. (2020). A review: Interlayer joining of nickel base alloys. *Journal of Advanced Joining Processes*, 2, 100030.

Reichardt, A., Shapiro, A. A., Otis, R., Dillon, R. P., Borgonia, J. P., McEner- ney, B. W., …& Beese, A. M. (2021). Advances in additive manufacturing of metal-based functionally graded materials. *International Materials Reviews*, *66*(1), 1–29.

Rezakhani, D. (2007). Corrosion behaviours of several thermal spray coatings used on boiler tubes at elevated temperatures. *Anti-Corrosion Methods and Materials*, *54*(4), 237–243.

Rodriguez, J., Hoefer, K., Haelsig, A., & Mayr, P. (2019). Functionally graded ss 316l to ni-based structures produced by 3d plasma metal deposi- tion. *Metals*, 9(6), 620.

Roy, T., Paradowska, A., Abrahams, R., Lai, Q., Law, M., Mutton, P., …& Yan, W. (2018). Effect of cladding direction on residual stress distribution in laser cladded rails.

Saboori, A., Aversa, A., Marchese, G., Biamino, S., Lombardi, M., & Fino, P. (2020). Microstructure and mechanical properties of AISI 316L produced by directed energy deposition-based additive manufacturing: A review. *Applied sciences*, *10*(9), 3310.

Sadeghi, E., Markocsan, N., & Joshi, S. (2019). Advances in corrosion- resistant thermal spray coatings for renewable energy power plants: Part II—Effect of environment and outlook. *Journal of Thermal Spray Technol- ogy*, *28*, 1789– 1850.

Sadeh, S., Mathews, R., Zhang, R., Sunny, S., Marais, D., Venter, A. M., Li, W., and Malik, A. (2023). Interlayer machining effects on microstructure and residual stress in directed energy deposition of stainless steel 316L. *Journal of Manufacturing Processes*, *94*, 69–78.

Saito, N., Komai, N., Sumiyoshi, Y., Takei, Y., Kitamura, M., & Tokairin, T. (2015). Development of materials for use in a-usc boilers. *Mitsubishi Heavy Industries Technical Review*, *52*(4), 27.

Salavati, S. (2016). *Thermally Sprayed High Temperature Sandwich Struc- tures: Physical Properties and Mechanical Performance*. University of Toronto (Canada).

Saltzman, D., Bichnevicius, M., Lynch, S., Simpson, T. W., Reutzel, E. W., Dickman, C., & Martukanitz, R. (2018). Design and evaluation of an additively manufactured aircraft heat exchanger. *Applied Thermal Engi- neering*, 138, 254– 263.

Saqib, S., Urbanic, R., & Aggarwal, K. (2014). Analysis of laser cladding bead morphology for developing additive manufacturing travel paths. *Procedia Cirp*, 17, 824–829.

Sathish, M., Radhika, N., & Saleh, B. (2021). A critical review on func- tionally graded coatings: Methods, properties, and challenges. *Composites Part B: Engineering*, 225, 109278.

Scala, K. D., Meschino, G., Vega-Galvez, A., Lemus-Mondaca, R., Roura, S., & Mascheroni, R. (2013). An artificial neural network model for prediction of quality characteristics of apples during convective dehydration. *Food Science and Technology*, *33*, 411–416.

Schleich, W. (2004). Typical failures of cuni 90/10 seawater tubing systems and how to avoid them.

Schwartz, M. P. (1982). *Four types of heat exchanger failures*. ITT Bell & Gosset.

Shang, C., Wang, C., Li, C., Yang, G., Xu, G., & You, J. (2020). Eliminating the crack of laser 3D printed functionally graded material from TA15 to Inconel718 by base preheating. *Optics & Laser Technology*, *126*, 106100.

Siddiqui, A. A. & Dubey, A. K. (2021). Recent trends in laser cladding and surface alloying. *Optics & Laser Technology, 134*, 106619.

Sidebotham, G. & Sidebotham, G. (2015). Heat exchanger fundamentals. Heat Transfer Modeling: An Inductive Approach, pages 445–474.

Singh, J., Thakur, L., & Angra, S. (2019). Effect of argon flow rate and standoff distance on the microstructure and wear behaviour of wc-cocr tig cladding. In *Journal of Physics: Conference Series*, volume 1240, page 012162. IOP Publishing.

Song, B., Hussain, T., & Voisey, K. (2016). Laser cladding of Ni50Cr: A parametric and dilution study. *Physics Procedia*, *83*, 706–715.

Stojanovi´c, B., Veli˘ckovi´c, S., Vencl, A., Babi´c, M., Petrovi´c, N., Miladinovi´c, S., & Cherkezova-Zheleva, Z. (2016). Optimization and prediction of aluminium composite wear using taguchi design and artificial neural network. *Tribological Journal BULTRIB*, *6*, 38–45.

Tiwari, G. K., Dubey, A. K., & Siddiqui, A. A. (2020). A hybrid approach for modelling and optimization of laser cladding process. *Int J Adv Prod Indus Eng*, *5*(1), 17–24.

Tomaz, I. d. V., Cola¸co, F. H. G., Sarfraz, S., Pimenov, D. Y., Gupta, M. K., and Pintaude, G. (2021). Investigations on quality characteristics in gas tungsten arc welding process using artificial neural network integrated with genetic algorithm. The International Journal of Advanced Manufacturing Technology, *113*(11-12), 3569–3583.

Tuck, C., Powell, C., & Nuttall, J. (2016). Corrosion of copper and its alloys.

Uenishi, K., Ogata, Y., Iwatani, S., Adachi, A., Sato, T., & Kobayashi, K. F. (2007). Laser cladding of fe-cu based alloys on aluminum. *Solid State Phenomena*, *127*, 331–336.

Updike, D., Kalnins, A., & Caldwell, S. (1992). Residual stresses in transi- tion zones of heat exchanger tubes.

Uusitalo, M., Vuoristo, P., & M¨antyl¨a, T. (2004). High temperature cor- rosion of coatings and boiler steels below chlorine-containing salt deposits. *Corrosion science*, *46*(6), 1311–1331.

Vasileiou, A. N., Smith, M. C., Francis, J. A., Balakrishnan, J., Wang, Y. L., Obasi, G., …& Irvine, N. M. (2021). Development of microstructure and residual stress in electron beam welds in low alloy pressure vessel steels. *Materials & Design*, 209, 109924.

Vasiliev, L. L. (2005). Heat pipes in modern heat exchangers. *Applied thermal engineering*, 25(1), 1–19.

Voisin, T., Shi, R., Zhu, Y., Qi, Z., Wu, M., Sen-Britain, S., Zhang, Y., Qiu, S., Wang, Y., …& Thomas, S., (2022). Pitting corrosion in 316L stainless steel fabricated by laser powder bed fusion additive manufacturing: A review and perspective. *JOM*, *74*(4), 1668–1689.

Wakchaure, K., Thakur, A., Gadakh, V., & Kumar, A. (2018). Multi- objective optimization of friction stir welding of aluminium alloy 6082-T6 Using hybrid Taguchi-Grey relation analysis-ANN method. *Materials To- day: Proceedings*, *5*(2), 7150–7159.

Wang, X., Yang, Z., Wang, Z., Shi, Q., Xu, B., Zhou, C., & Zhang, L. (2019). The influence of copper on the stress corrosion cracking of 304 stainless steel. *Applied Surface Science*, 478, 492–498.

Wang, Y., Liang, Z., Zhang, J., Ning, Z., & Jin, H. (2016). Microstructure and antiwear property of laser cladding Ni–Co duplex coating on copper. *Materials*, *9*(8), 634.

Wang, Z., Lu, H., Cai, J., Wu, L., Luo, K., & Lu, J. (2022). Improvement mechanism in stress corrosion resistance of the X70 pipeline steel in hydro- gen sulfide solution by massive laser shock peening treatment. *Corrosion Science*, 201, 110293.

Watring, D. S., Benzing, J. T., Hrabe, N., & Spear, A. D. (2020). Effects of laser- energy density and build orientation on the structure–property rela- tionships in as-built inconel 718 manufactured by laser powder bed fusion. *Additive manufacturing*, *36*, 101425.

Wei, C., Zhang, Z., Cheng, D., Sun, Z., Zhu, M., & Li, L. (2020). An overview of laser-based multiple metallic material additive manufacturing: from macro-to micro-scales. *International Journal of Extreme Manufactur- ing*, *3*(1), 012003.

Weng, F., Chen, C., & Yu, H. (2014). Research status of laser cladding on titanium and its alloys: A review. *Materials & Design*, *58*, 412–425.

Wu, D., Liang, X., Li, Q., Jiang, L., et al. (2010). Laser rapid manufacturing of stainless steel 316L/Inconel718 functionally graded materials: microstruc- ture evolution and mechanical properties. *International Journal of Optics*, *2010*.

Wu, D., Yuan, Z., Liu, S., Zheng, J., Wei, X., & Zhang, C. (2020). Recent development of corrosion factors and coating applications in biomass firing plants. *Coatings*, *10*(10), 1001.

Xu, S., Wang, C., & Wang, W. (2015). Failure analysis of stress corrosion cracking in heat exchanger tubes during start-up operation. *Engineering Failure Analysis*, *51*, 1–8.

Yan, H., Zhang, P., Yu, Z., Lu, Q., Yang, S., & Li, C. (2012). Microstructure and tribological properties of laser-clad Ni–Cr/TiB2 composite coatings on copper with the addition of CaF2. *Surface and Coatings Technology*, *206*(19-20), 4046– 4053.

Yan, L., Chen, Y., & Liou, F. (2020). Additive manufacturing of func- tionally graded metallic materials using laser metal deposition. *Additive Manufacturing*, *31*, 100901.

Yang, X., Liu, M., Liu, Z., Du, C., & Li, X. (2020). Failure analysis of a 304 stainless steel heat exchanger in liquid sulfur recovery units. *Engineering Failure Analysis*, *116*, 104729.

Yoo, H. J., Baek, S., Kim, J. H., Choi, J., Kim, Y.-J., & Park, C. (2022). Effect of laser surface cleaning of corroded 304l stainless steel on microstruc- ture and mechanical properties. *Journal of Materials Research and Tech- nology*, *16*, 373–385.

Zhang, X., Chen, Y., & Liou, F. (2019). Fabrication of ss316l-in625 func- tionally graded materials by powder-fed directed energy deposition. *Science and Technology of Welding and Joining*, *24*(5), 504–516.

Zhang, X., Li, L., & Liou, F. (2021). Additive manufacturing of stain- less steel–copper functionally graded materials via inconel 718 interlayer. *Journal of Materials Research and Technology*, *15*, 2045–2058.

Zhang, Y.-z., Tu, Y., Xi, M.-z., & Shi, L.-k. (2008). Characterization on laser clad nickel based alloy coating on pure copper. *Surface and Coatings Technology*, *202*(24), 5924–5928.

Zhu, L., Xue, P., Lan, Q., Meng, G., Ren, Y., Yang, Z., Xu, P., and Liu, Z. (2021). Recent research and development status of laser cladding: A review. *Optics & Laser Technology*, *138*, 106915.

Ziaei, S., Kokabi, A., & Mostowfi, J. (2014). Failure analysis: sulfide stress corrosion cracking and hydrogen-induced cracking of A216-WCC wellhead flow control valve body. *Journal of Failure Analysis and Prevention*, *14*, 376–383.

Zohuri, B. (2017). *Compact heat exchangers*. Springer Cham, Switzerland.

APPENDICES

Appendix I: ANN Program/Code

```
% Optimizing the GRG using neural network
% Script generated by Levenberg-Marquardt Back Propagation (LMBP) method
% for training, testing, and validation.
clc  close all
X = Inputs; y
= Output;
X1 = X(:,1:27);
y1 = y(:,1:27); n = 4;

net2 = feedforwardnet(n) ;
% define a neural network (a variable called ”net”’), which 1g a 3-layer
% perceptron (3LP) with n nodes in the hidden layer net2.trainFcn = ’trainlm’
% net.trainFcn = ’trainc’ net2.divideFcn = ’divideblock’;
% net2.divideFcn = ’dividerand’; net2.layers2.transferFcn = ’tansig’;
% net.layers1.transferFcn = ’poslin’;
% net.divideFcn = ’dividerand’;
% net2.divideParam.trainRatio = 0.8;
% net2.divideParam.valRatio = 0.2;
% net1.divideParam.testRatio = 0.075;
% net.performParam.regularization = 0.0001; net2 = configure(net2,X, y);
% view(net2)
[net2, TR] = train(net2,X, y);
x1 = X(1,:);
x2 = X(2,:);
x3 = X(3,:);
y_model = zeros(length(X), 1);
for i= 1:length(y)
y_model(i) = net2([x1(i); x2(i); x3(i)]);
```

```
% simulate neural network with varying xl, but all other variables constant end
Predicted_y =  y_model;
figure(2) plot(y','rd–') hold on
plot(Predicted_y,'bd–')
% plot(x1',y','r+:',x1',y_model,' gd–') xlabel('Experiments')
ylabel('GRG') legend('Actual','ANN model') grid on
mse_perf = mse(net2,y_model,y')

% save ('BestNET.mat', 'net2')
%%
x1_test =600:100:1000;
%
for i= 1:length(x1_test)
y_test1(i) = net2([x1_test(i); 600; 2]);
% simulate neural network with varying xl, but all other variables constant end x2_test
=floor(200:100:1000); for
i= 1:length(x2_test)
y_test2(i) = net2([850; x2_test(i); 2]);
% simulate neural network with varying xl, but all other variables constant end x3_test
=1:1:6;

for i= 1:length(x3_test)
y_test3(i) = net2([850; 600; x3_test(i)]);
% simulate neural network with varying xl, but all other variables constant end

%%
figure(3) plot(x1_test,y_test1,'rd–') xlabel('x1 input') ylabel('GRG') legend('x1
input')

grid on

%%

figure(4) plot(x2_test,y_test2,'bd–') xlabel('x2 input')
```

```
ylabel('GRG') legend('x2 input') grid on

%%

figure(5) plot(x3_test,y_test3,'gd–') xlabel('x3 input') ylabel('GRG') legend('x3 input')
grid on

%%

% Optimized_GRG
Optimized_GRG = net2([600; 700; 1.5])
clc  close all clear
load TR2
x1_test =300:100:1000;

%

for i= 1:length(x1_test)
y_TR1(i) = net([x1_test(i); 600; 2]);
y_TR2(i) = net1([x1_test(i); 600; 2]);
% simulate neural network with varying xl, but all other variables constant y_TR3(i) =
net2([x1_test(i); 600; 2]);
end plot(x1_test,y_TR1,x1_test,y_TR2,x1_test,y_TR3)
```